Pre-Clinical Development of Best-in-Class $Zn_{0.4}Fe_{2.6}O_4$ Magnetic Nanoparticles for Thermal Treatment of Brain Glioblastoma

Georgios Kasparis

PhD Thesis

Faculty of Mathematical and Physical Sciences

Department of Physics & Astronomy

University College London

Declaration of Originality

I, Georgios Kasparis, declare in lieu of an oath that I have written this document myself. Where the work of others is used is clearly indicated and all sources are properly referenced. Opinions expressed herein do not represent the university and are solely the opinions of the author. I confirm that this document has not been submitted before or elsewhere for another degree.

Abstract

Nanomaterials are intensely researched and developed for a wide range of applications. The focus of this work is on developing novel nanomaterials with augmented physicochemical properties for biomedical applications. Specifically, developing magnetic nanoparticles for thermal treatment of neoplasms as this method offers a potentially drug-free approach to cancer treatment currently approved for clinical use for a limited number of malignancies and undergoing further trials for assessing its effect on others. To date, several procedures have been established to produce nanoparticles with variable shapes, sizes and compositions and their effect on various technologies are intensely investigated. Among both anisotropic and isotropic magnetic nanoparticles synthesised as part of this work, superparamagnetic zinc doped ferrite nanoparticles were the most suitable for further development owing to their high magnetisation, superparamagnetic nature, low anisotropy and biocompatibility as characterised by their chemical and physical attributes and compared with iron oxide nanoparticles of same size and morphology. These nanoparticles have been developed using liquid chemistry routes under high temperature and pressure. Their extensive characterisation renders them as the best-in-class nanoparticles in terms of their magnetic properties and size exceeding the magnetic properties of the next most magnetic zinc ferrite synthesised to date whilst having ten times smaller magnetic volume. Their ability to convert magnetic energy to heat (magnetothermal) and light to heat (photothermal) has been assessed with photothermia being far more efficient than magnetothermia both in suspension and in cellular confinement. Magnetothermal conversion was similar to other superparamagnetic materials and of limited clinical use while photothermal conversion showed enhanced performance achieving complete cell death in 10 minutes using clinically relevant settings. The nanoparticles showed extensive cellular uptake *in vitro* on brain glioblastoma cells as indicated by imaging and magnetometry. The biocompatibility of the nanoparticles has been assessed with several techniques to assess mitochondrial function, cell membrane integrity and clonogenicity indicating a well-tolerated material of similar toxicity to iron oxide which itself is cleared for medical use by the Food and Drug Administration

and the European medicines Agency. A practical treatment time has been determined to induce preferentially irreversible apoptosis than necrosis in *in vitro* experiments as a result of apoptosis-related proteins expression or inhibition and reactive oxygen species formation before, during and after thermal treatment. Biodistribution studies made use of nuclear medicine tomographic imaging techniques to monitor the biodistribution profile of the nanomaterial in real-time including positron emission tomography and single photon emission computed tomography integrated with computed tomography on physiological and immunocompromised mice via intravenous and intranasal administration. The nanomaterial mainly accumulates in organs involved in the clearance pathway; the liver and the kidneys with a small amount of material reaching the brain.

Acknowledgments

This work would have not been possible without the many people who have contributed in the execution, discussion, provision of facilities and funds. As such I need to wholeheartedly extend my gratitude by individually acknowledging their participation.

It is essential to acknowledge the funding bodies and organizations who had believed in my proposals and funded this work. The Engineering and Physical Sciences Research Council (EPSRC) and University College London (UCL) for my PhD studentship which without I would have not been able to do so. The Royal Society of Chemistry (RSC) and Society of Chemical Industry (SCI) for awarding me funds to attend and orally present my work at UK Colloids 2017 in Manchester, UK, through the Rideal Grant. The RSC for providing funds to attend and orally present at the 12th International Conference on the Scientific and Clinical Applications of Magnetic Carriers 2018 in Copenhagen, Denmark. The UCL Postgraduate Teaching Committee for providing funds to attend UK Colloids 2017 in Manchester, UK, and the 12th International Conference on the Scientific and Clinical Applications of Magnetic Carriers 2018 in Copenhagen, Denmark. The RSC for awarding me the Researcher Mobility Grant to visit the National Centre for Scientific Research (NCSR) Demokritos in Athens, Greece to perform radiolabelling and *in vivo* work. The European Commission which through their Cooperation in Science and Technology (COST) scheme awarded me multiple financial awards to visit overseas laboratories to perform experimental work including the Barr Ilan University in Tel Aviv, Israel, for bioconjugation and *in vitro* work, visit twice University Paris Diderot in Paris, France, for photothermal assessment and *in vitro* work, funds to attend the Annual Progress Conference in Timisoara, Romania, funds to attend and orally present my work at the Final Meeting of the programme in Florence, Italy, and funds to attend and orally present at COST workshop in Bialystok, Poland. The School of Analytical Sciences Adlershof in Berlin, Germany, for providing funds to attend their summer school and debate leaders in nanotechnology. UCL for their Grand Challenges competition for awarding me the award in Global Health Section for collaborating with UCL Medical School at the Royal Free Hospital in London

for extending biological assessment of photothermal therapy. The British Society of Nanomedicine for allowing me to orally present my work to their Annual Early Career Researchers conference. From all the above programmes and schemes, I have formed an extended network of colleagues with whom I have written proposals and maintain professional and personal relationships. To all, without the impeccable systems for science funding, dissemination and execution, vast parts of this work would have been impossible and as such I am most thankful.

Firstly, I need to acknowledge Thanh Nguyen who gave me the freedom to explore my ideas and encouraged me to join the RSC and Ivan Parkin for support and feedback towards the completion of this thesis. My colleagues, who have been incredibly helpful in scientific as well as personal discussions and supported one another through this journey. I want to thank Andreas Sergides who through his Doctoral Training School had access to facilities at Imperial College London who he kindly performed as needed. Alec LaGrow helped with the interpretation of such data. Simone Famiani and Stefanos Mourdikoudis who were participating in scientific discussions; Lilin Wang for teaching me the basics in biological experiments and Shiv Patel for assistance in executing the work of the proposal submitted to UCL Grand Challenges; Quentin Pankhurst and Paul Southern for providing an infrared camera; Lara Bogart for useful discussions on magnetism; Eleni Efthymiadou for providing the U87-MG cell line; Eva Salvanou and Maria Karayeoryou who taught me and assisted me in radiological studies; Maria Theodosiou who have been a very good colleague and a friend; Stauros Xanthopoulos and Maritina Rouchota for assisting in *in vivo* work; Penelope Bouziotis for her expertise and guidance in radiolabelling; Spyridon Spyrou for useful discussions towards combining radiochemistry with photothermal therapy; Claire Wilhelm who with her endless knowledge in photothermia hugely assisted in the design of those experiments; Anouchka Plan Sagnier for assisting me with the use of instruments and execution of *in vitro* work for hyperthermia. Lastly and most importantly, I want to cordially extend my thanks to Aritz Sterne Erdocio, Horatio Cox, Joshua Mark Tuffnell, Christoforos Efstathiou, Sayeed Ahmed and Afia Shakir who as part of their placement or university degree assisted in

the execution of parts of this work including in synthesising anisotropic ferrites, reducing the polydispersity of ferrites and biological assessment of nanomaterials. To all, thank you. You have taught me plenty at both personal and professional levels. I wish you the very best of luck in your future endeavours.

Impact Statement

Cancer in general, is a disease that scares most of us. Its occurrence is increasing year after year with only a few cancers having a good prognosis. Many, such as brain cancer, is viewed as a death sentence hence there is an urgent need to advance the development and number of treatments for this disease.

Hyperthermia, as a treatment for malignancies, undergone clinical trials with conflicting results and is now undergoing more. Nanotechnology has advanced so much since the initiation of the latest clinical trials that the nanomaterials currently used seem outdated with limited performance. To this end, the preparation of novel nanomaterials to augment the performance of nanoparticles in localized hyperthermia was proposed.

Through extended literature review and experimental attempts to prepare state-of-the-art nanoparticles, best-in-class materials were prepared. By making use of pressure close to perfect nanocrystals were obtained which is reflected in their magnetic properties. As such, many collaborators around the globe are utilising the developed nanomaterial to further their own work in several different applications. Further, the semiconducting properties of the magnetic nanoparticles instead of their magnetic were exploited, an unorthodox approach, with a massive enhancement in performance *in situ* and *in vitro* in hyperthermia tests. Additionally, the exploitation of uncommon routes of administration such as the intranasal cavity was used for direct delivery of nanoparticles to the brain by-passing this way the blood-brain-barrier, a significant obstacle for drug delivery to the brain.

It is believed that many can benefit from this work especially scientists investigating the current issues in hyperthermia. By using non-standard methods and techniques great outcomes can come and only this way an unexpected great treatment can be achieved. Ultimately, it is hoped that people suffering from brain cancer will, one day, benefit from localised hyperthermia and the approach paved.

Table of Contents

1 Introduction

1.1 Hyperthermia as a Medical Tool

Hyperthermia is derived from the Greek words "υπέρ" meaning "above" or "over", and "θερμός" meaning "hot" and is used to describe a situation where the temperature has been increased to levels above a set normal[1]. In biomedicine, this is used to describe situations where the body temperature has been elevated by external factors while the body's temperature set point remains at physiological values and this is how hyperthermia differs from fever (disease).

Exploiting hyperthermia for cancer treatment dates back many years. The physiology of neoplasms, being hypoxic and acidic, renders them susceptible to heat and prone to deteriorate at temperatures between 41-46 °C, temperatures that healthy cells can withstand and this is what gives hyperthermia specificity[1,2]. The concept of hyperthermia in oncology is that a controlled level of heat can be applied at the site of interest which would kill nearby malignant cells which are damaged by the temperature increase. The temperature increase must be in a range where healthy cells remain unaffected, ideally achieving selective elimination of cancerous populations. Usually trialled as an adjunctive modality to radiotherapy or chemotherapy, thermotherapy has gone a long way since the first hot water applicators. Bags with water were heated up with radiofrequency radiation to warm up a region on the body, so called regional hyperthermia[1]. Due to various factors, thermotherapy never took off, either because of limited number of companies making the applicators, the inability of the small companies making those to advertise in mass media or conflicting clinical trial results[3,4]. Today, research has progressed beyond whole body or regional hyperthermia to a highly specific alternative, local hyperthermia. Nanotechnology allowed the precise manipulation of matter at the nanoscale, which in turn allowed the maximisation of heat released by nanoparticles (NPs). Consequently, the number of scientific articles published through the years has been increasing exponentially as shown in Figure 1 (Scopus, term 'hyperthermia', extracted on the 02/12/2018).

There are two major materials that are intensively researched for this purpose, magnetic NPs in which case magnetic energy is converted into heat[5,6] or noble metal NPs to transform light into heat[7,8]. Magnetic NPs can induce hyperthermia, as do gold NPs albeit with different mechanism, but magnetic NPs can also be externally manipulated due to their magnetic properties hence, magnetic nanomaterials offer multifunctionality over other nanomaterials.

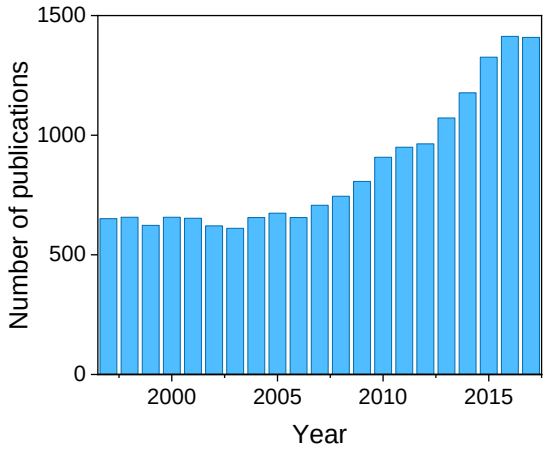

Figure 1: Number of publications with the term 'hyperthermia' between 1997-2017.

The recent advances in matter manipulation and development of nanomaterials with augmented properties sparked again the interest of the clinical community which is reflected in the latest clinical trials reassessing the clinical potential of hyperthermia as a medical tool in oncology with a German company leading the way[4]. MagForce AG, has developed the first clinical alternating magnetic field (AMF) applicator (necessary to heat magnetic NPs – discussed in 2.1.1). The NPs are injected inside the tumour where they remain for a long time allowing for multiple consequent treatments. An official approval has been obtained, valid for all states in the European Union, for the treatment of brain tumours. Currently, a pilot study with 80 patients is underway to extend this modality to pancreatic, breast and oesophageal cancers[9].

1.2 Specificity of Nanomedicines to Tumours

Nanomedicine is the medical application of nanotechnology used to prevent or treat disease. Although this branch of medicine involves nanoscale materials[10,11], nano-electronic biosensors[12,13], biological machines[14] and others, herein the focus is on the development of magnetic nanomaterials for cancer hyperthermia.

Materials scaled down to the nanoscale exhibit different physical and chemical properties compared to their bulk counterparts. For example, a gold nugget has a shiny golden colour while nano-scaled gold can vary between deep red to green as shown in Figure 2[15]. Magnetic materials scaled down to the nanoscale change their magnetic properties from ferro- and ferrimagnetic to superparamagnetic behaviour[16].

Figure 2: Gold NPs of different sizes.

Another property of nano-pharmaceutics for cancer treatment is their ability to specifically target vascularised tumours over healthy tissue[17]. Tumours grow substantially and quickly and to sustain their intense growth, they release factors to initiate angiogenesis, a vasculature growth process. This facilitates the delivery of nutrients throughout the tumour to support further growth[18]. This rapidly formed vasculature has fenestrae due to its rapid formation[19]. These pores can be exploited for preferential accumulation at such sites giving this delivery method specificity. Once NPs exit the circulation, they are retained on the side due to constant positive pressure from flowing blood[17]. This phenomenon is called enhanced permeation and retention (EPR) effect also known as passive targeting and is the most common targeting technique for cancer nano-pharmaceutics. An illustration of this effect is shown in Figure 3. In addition to passive targeting, one can engineer the surface of the NPs in

such manner to target at the cellular level through special recognition[17]. This method is called active targeting and does not exclude passive targeting. In this case, molecules such as peptides[20], antibodies[21], sugars[22], aptamers[23] and other biomolecules have been used to recognise structures on the surface of cells that express or overexpress the appropriate binding site in contrast with other cell populations that might be present nearby. This way, preferential uptake at the cellular level can occur and many studies have shown the efficiency of both methods[17].

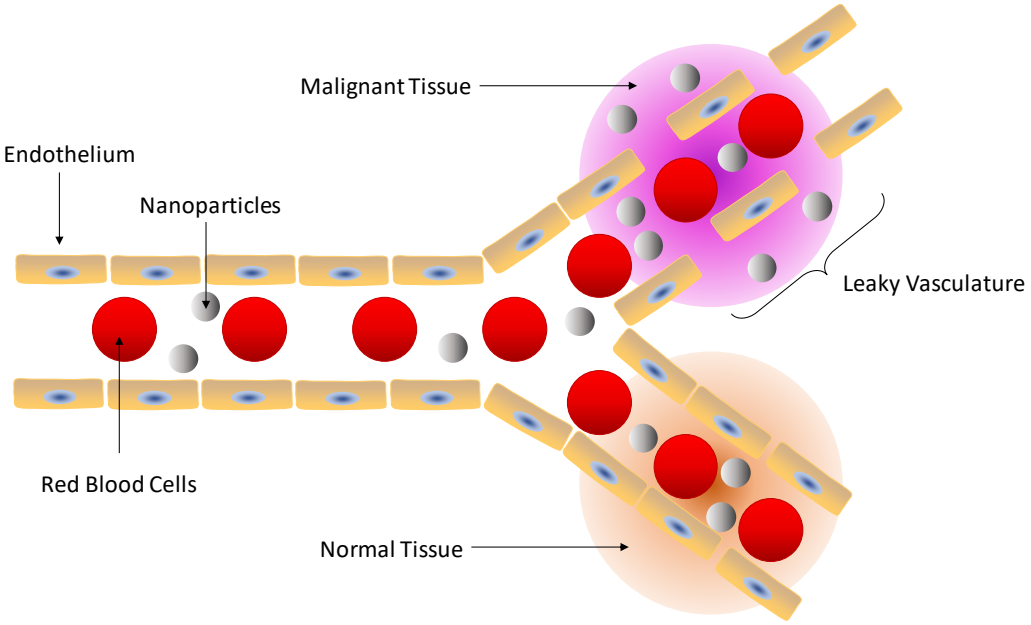

Figure 3: NPs exiting the systemic circulation due to fenestrae on cancer neovasculature.

1.3 Magnetism and Magnetic Nanoparticles

Magnetic NPs consist of a large family of magnetic materials that have been scaled-down to nano-sized crystals. Typical examples and the only Food and Drug Administration (FDA) approved materials today are based on magnetite (Fe_3O_4) and maghemite (γ-Fe_2O_3). These two materials have long been studied and today one can produce variable sizes[24,25] and shapes[26,27]. Research in the field is on-going with substituted ferrites; cobalt[28], zinc[29], manganese[30], magnesium[31] and others that adapt the formula $M_xFe_{3-x}O_4$. Other materials include metallic nickel[32], iron[33,34] and their alloys, iron cobalt[35], iron platinum[36], iron nickel[37] and others. Beyond being a biocompatible

material with small size for passive targeting, magnetic nanomaterials have further attributes that need to be met to be suitable for clinical use. These are closely linked to their magnetic properties and are discussed in detail in section 1.4.

1.4 Types and Properties of Magnetic Materials

There are six types of magnetism; paramagnetism, diamagnetism, ferromagnetism, ferrimagnetism, antiferromagnetism and spin-glass[38]. Paramagnetic substances display a weak attraction to an applied magnetic field and is observed in atoms and molecules with an odd number of electrons since the net magnetic moment cannot be zero. Diamagnetism is the opposite to paramagnetism, it is a weak repulsion from an applied magnetic field because of a current induced in the electron orbits of the atoms by the applied magnetic field; all materials exhibit this behaviour more often masked by other phenomena. For extended networks of atoms such as in crystals, the other four types of magnetism are rather more common due to long range ordering of the atoms with the exception of spin-glass which refers to lack of spatial orientation similar to paramagnetism although frozen in time. The magnetic moment of each atom can align parallel or antiparallel with a neighbouring atom while the third case arises when the antiparallel alignment is composed of two unequal in magnitude magnetic moments as shown in Figure 4. These three ways of ordering make up ferromagnetic, antiferromagnetic and ferrimagnetic materials, respectively.

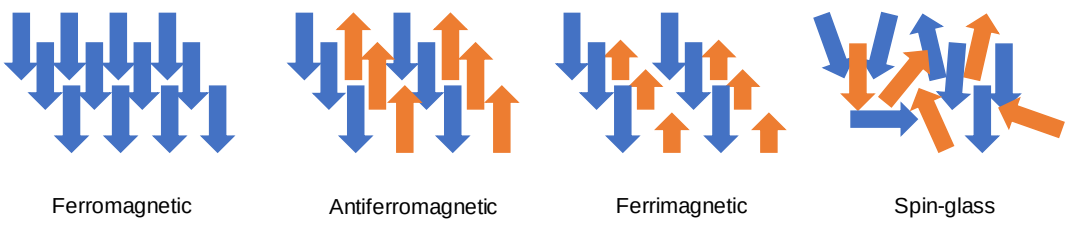

Figure 4: Types of magnetic ordering.

In ferromagnetic materials, all magnetic moments are aligned in-parallel and such materials exhibit a big permanent magnetic moment. In the case of antiferromagnetic materials, the spins are aligned antiparallel and they cancel each other out while in ferrimagnetic materials the spins of opposing directions

are not of equal magnitude hence these materials also exhibit a permanent magnetic moment. Fe_3O_4 and γ-Fe_2O_3 fall in this last category of magnetic materials, they are ferrimagnetic.

The interest in ferrimagnetic materials stems from the ability to manipulate the crystal lattice and introduce new properties or manipulate pre-existing. The scientific principle termed superexchange is a phenomenon where the electrons of a cation are coupled with another through an adjacent anion[38]. A simplification of this effect is shown in Figure 5.

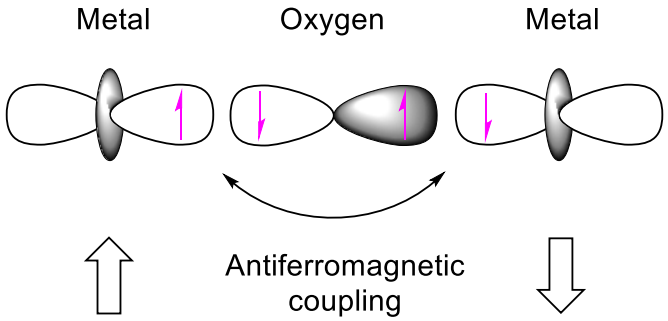

Figure 5: Illustration of superexchange of two metal cations via a non-metallic anion.

In the case of iron oxides, the Fe^{3+} cations are surrounded by O^{2-} anions. The valence electrons of Fe^{3+} interact with the electrons of the oxygen ion and this effect percolates though the crystal. The eventual effect, whether ferromagnetic or antiferromagnetic is geometry dependent but often is an antiferromagnetic interaction. Taken Fe_3O_4 as an example, the crystal consists of two interpenetrating magnetic sublattices. The iron ions between the two sublattices have an angle of 127° which renders the interaction antiferromagnetic. In order to increase the magnetic properties of this material non-magnetic cations were to be incorporated in the crystal and break the antiferromagnetic coupling[39]. Further discussion on this effect follows in section 3.3.2.

Magnetic behaviour is also hugely influenced by the size of the crystallites[38,40]. Bulk magnetic materials spontaneously split into magnetic domains, regions where the magnetic vector faces at a direction different from the neighbouring domains. These domains arise from structural defects. Such materials are referred to as multi-domain and the magnetic vectors of the domains will align

when a magnetic field is applied. Reducing the size down smaller to that of domains in bulk materials, the particles are single-domain and their magnetic moment is uniform throughout, oriented to a specific direction called the easy axis which is intrinsic to each material based on its crystal lattice. The energy required to flip the spin in single-domain particles from its easy axis is known as the magnetocrystalline anisotropy and is illustrated in Figure 6[41].

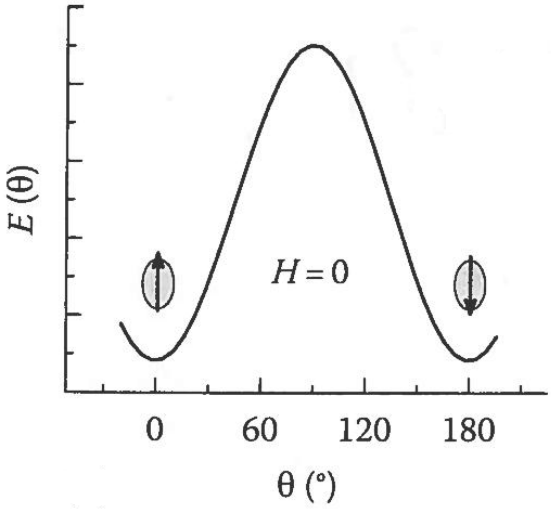

Figure 6: Magnetocrystalline anisotropy energy barrier.

Reducing the size even further, one enters the superparamagnetic regime. At a small enough size, ambient thermal energy is enough to overcome the magnetocrystalline anisotropy barrier flipping the magnetic vector at random. Even though each individual particle will have a magnetic moment, the collective random flipping manifest itself as a zero-magnetic moment in the absence of a magnetic field. This phenomenon is known as superparamagnetism and is the type of magnetism required for biomedical applications. Multi-domain, single-domain and superparamagnetic crystals are illustrated in Figure 7A, while some indicative size limits for when crystals of different materials become superparamagnetic[40] are shown in Figure 7B.

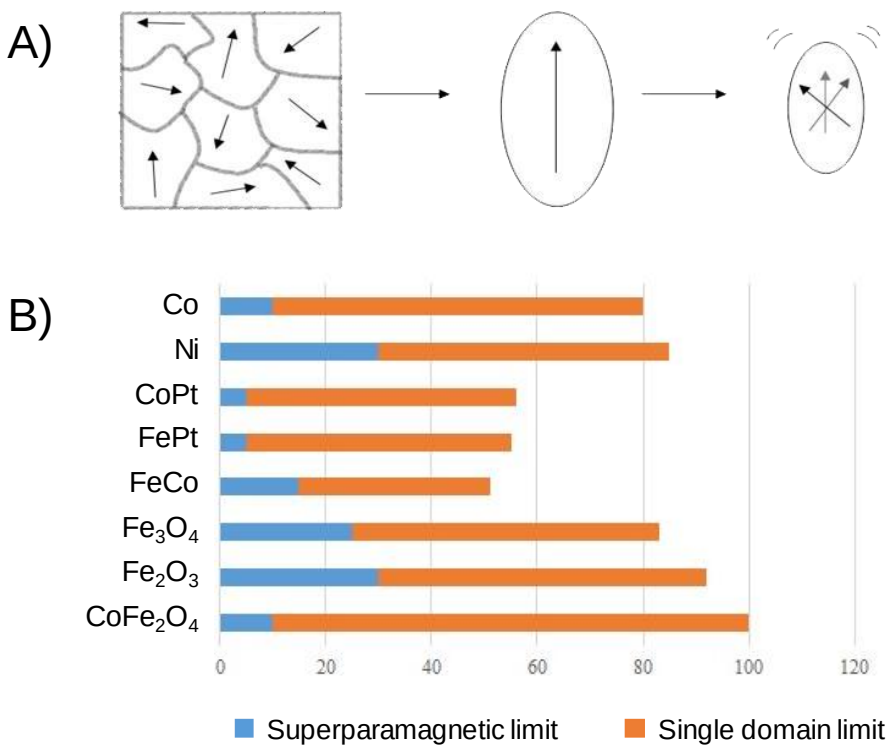

Figure 7: A) The transition of a multi-domain crystal (left) to a single domain crystal (centre) and a superparamagnetic crystal (right) and B) Superparamagnetic and single-domain size limits for magnetic NPs.

Single- and multi-domain crystallites will retain some magnetisation when the applied magnetic field is removed, known as remnant magnetisation. The importance of using superparamagnetic particles for clinical applications is the lack of remnant magnetisation in the absence of a magnetic field which would otherwise cause nearby crystals to attract each other, aggregate and possibly lead to vascular occlusion. The field required to be applied in the opposite direction to bring the magnetisation to zero is known as the coercive field. In a field versus magnetisation plot [M(H)], a loop is formed known as hysteresis and is indicative of non-superparamagnetic particles. Coercivity, or resistance to demagnetisation, is also size dependent and is illustrated in Figure 8[42].

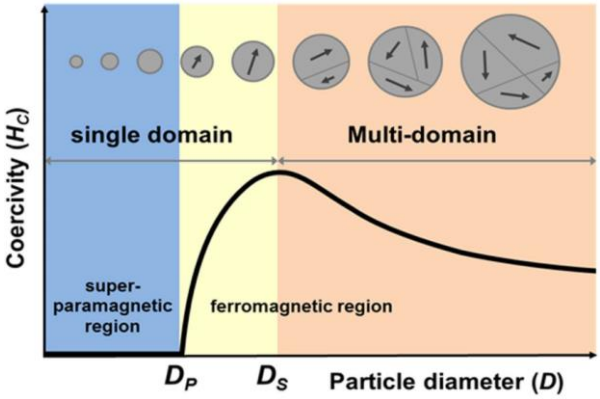

Figure 8: Coercivity as a function of size.

1.5 Commercial Use of Magnetic Nanoparticles

Magnetic NPs had previously been commercialised as negative contrast agents in magnetic resonance imaging (MRI). Two well-known examples include Feridex®, a polymer coated 4-6 nm spherical magnetic crystallite and Resovist®, also a polymer coated 5-10 nm spherical magnetic crystallite. The preferential use of positive, gadolinium-based contrast agents led to lack of use and the discontinuation of negative contrast agents. With on-going research, impressive positive contrast using iron oxide NPs has been achieved[43,44] as shown in Figure 9[44] and can potentially replace nephrotoxic gadolinium contrast agents[45] in the future.

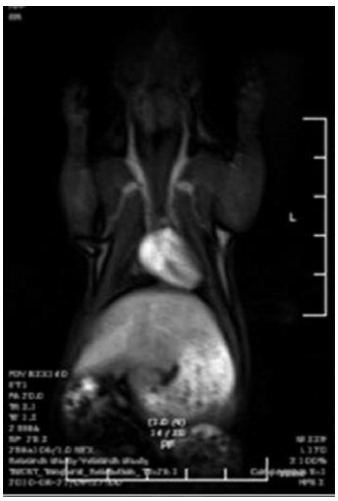

Figure 9: T1 MRI contrast with iron oxide NPs.

Magnetic NPs are also exploited for drug delivery as delivery platforms themselves by attaching the medicinal molecule on their surface or as a part

of a larger entity[46,47]. Such use of magnetic NPs offers selective spatial accumulation by the application of an external magnet while their heating ability offers triggerability or controlled release of molecules on-demand[46]. The delivery system can be thermo-responsive and as such heat released by magnetic NPs can initiate the release of cargo. This approach often appears in academic literature[46,48].

Blood detoxification and pathogen removal has also been achieved using magnetic NPs[49,50] and this technology is reaching the market[51]. MediSieve Ltd, UK, has used surface engineered iron oxide NPs to clear blood-borne diseases such as malaria, leukaemia, and sepsis. The principle is illustrated in Figure 10.

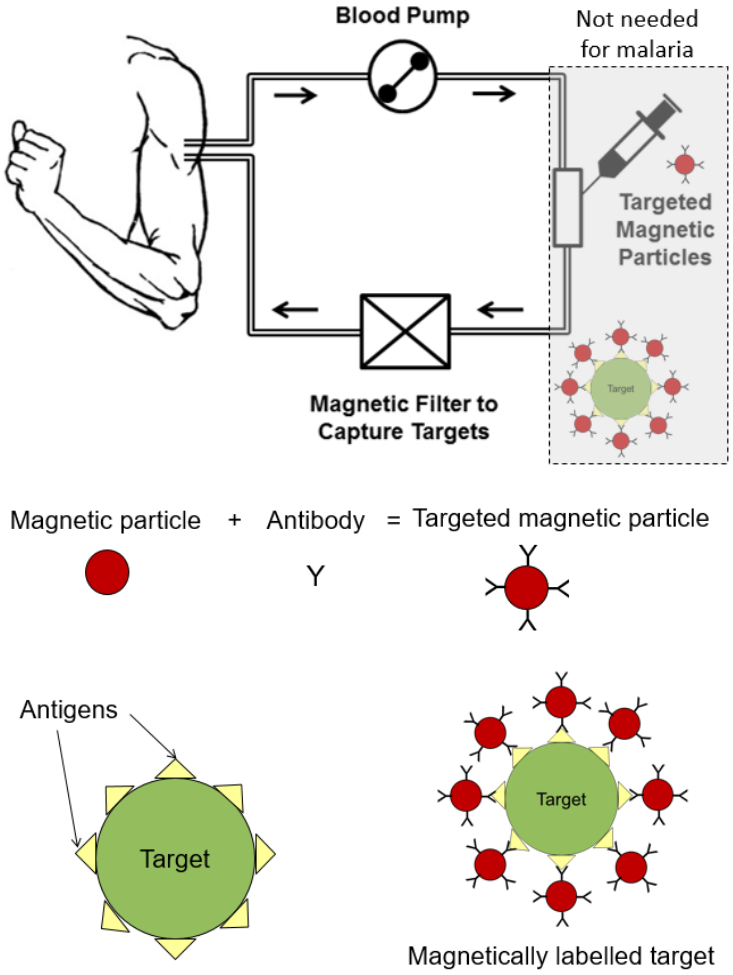

Figure 10: Blood detoxification system based on iron oxide NPs from MediSieve Ltd, UK.

Magnetofection is another use of magnetic NPs where DNA-bound magnetic NPs deliver nucleic acids to specific targets *in vivo*, or more efficiently in cell cultures after forced contact with the cells by a magnet[47]. Additionally, magnetic NPs are encapsulated in viral vectors to deliver nucleic acids *in vivo* in laboratory settings from OZBiosciences SAS, France.

Last but not least, iron oxide NPs are also commercially available for laboratory use from different companies such as Resonant Circuit Ltd, UK, NanoStructured & Amorphous Materials Inc., USA, Skyspring Nanomaterials Inc., USA, Creative Diagnostics, USA, Merck Ltd, UK and many others while those that made it into clinical trials are much less in numbers and are focused on treating brain glioblastoma and prostate adenocarcinoma by thermotherapy, assessed by MagForce AG, Germany[9]. Such products and their uses are tabulated in Table 1.

Table 1: Companies selling magnetic NPs, their trade name and intended use.

Company	Product	Laboratory Use	Clinical Use
Nanoscale Biomagnetics	Magno	✓	
Resonant Circuits	RCL-01	✓	
Endomagnetics	Sienna+	✓	
Chemicell	FluidMag	✓	
AMAG	Feraheme		✓
AMAG	Ferridex		✓
Pharmacosmos	Ferrisat		✓
Sanofi	Ferrlecit		✓
Vifor	Ferinject		✓
MagForce	NanoTherm		✓

1.6 Current Needs for Clinical Translation of Hyperthermia

There are many commercially available magnetic NPs formulations, all of them are based on iron oxide NPs. Even though superparamagnetic iron oxide NPs appear in literature in magnetic fluid hyperthermia (MFH) studies, their

performance is usually poor. To this end, introducing anisotropy in nanomaterials such as altering the shape of the NPs was shown to enhance the performance of MFH at least in *in situ* scenarios[52,53]. The preparation of shaped NPs is not trivial and many of these reports produce inadequate quantities of materials, require specialised techniques and equipment, or suffer from irreproducibility.

In addition to the physical properties of the NPs themselves, intravenously (IV) administering iron oxide NPs leads to a protein corona formation, which is the attachment of blood-borne proteins on the coating of the NPs[54,55]. Consequently, this leads to recognition from the mononuclear phagocyte system (MPS) which is responsible for removing foreign bodies from the body leading to liver accumulation as the main metabolic organ of the human body[54]. This translates to subtherapeutic levels of material reaching the tumours. Subsequently, this leaves scientists with the only option to intratumourally deliver the NPs to reach the high concentration required to achieve a therapeutic level of heat. This is a highly risky procedure itself and is not expected to reach clinical practice. Therefore, there is a need to develop nanomaterials with higher performance in MFH to achieve adequate levels of heat. There are three main prospects to achieve this:

- Increasing the amount of material able to reach the tumour and/or
- Investigate other routes of administration and/or
- Devise other ways of inducing hyperthermia.

The focus of this study was concentrated on two types of malignancies. Breast adenocarcinoma which is a superficial tumour best suited for non-or minimally-invasive treatment and brain glioblastoma which due to its low survival rates and severity there is an urgent need for novel treatments.

Our approach to tackle the aforementioned obstacles as far as material design is concerned, included the preparation of the highest performing NPs for MFH as they appear in literature with the aim of increasing their magnetic properties by quenching superexchange enhancing their magnetothermal properties further, discussed in sections 2.1.1 and 4.3.4. Our efforts also focused on modifying current synthetic procedures to synthesise biocompatible magnetic

nanomaterials with augmented electronic and magnetic properties and investigate unconventional methods to induce heat based on the semi-conducting properties of such materials enhancing the heating effect while reducing the necessary dose.

1.7 Aims of the Thesis

The purpose of this work was to prepare novel nanomaterials with potential use in clinical practice for the treatment of cancer. As such, it had to be a biologically compatible material with minimal toxicity, facile and scalable preparation methods, and high performance in thermotherapy.

Current state-of-the-art iron oxide NPs were to be replicated and doped with Zn^{2+} to increase their magnetic properties and reassess their magnetothermal conversion. Three syntheses were of interest to prepare:

- Cubic iron oxide NPs
- Spindle iron oxide NPs
- Multi-core iron oxide NPs

If the above methods were to be proven reproducible, materials would be doped and characterised. The most suitable material would be biologically evaluated for biocompatibility and performance in cellular experiments.

In the unfortunate case, where the above protocols could not be replicated in our labs, the most magnetic spherical iron oxide NPs would be prepared, doped and assessed.

The preparation of spherical iron oxide NPs prepared under high pressure with a scalable and facile method was to be replicated and have their performance assessed after Zn^{2+} doping. If this method was to be proven reproducible, a specific level of doping should be determined to produce the most magnetic NPs and assess their magnetothermal conversion. If magnetothermia was highly effective, biocompatibility experiments of these NPs would follow and assess magnetothermia performance in the cellular environment.

If magnetothermia was poorly performing, the electronic effects altered by Zn^{2+} doping would be evaluated for photothermal conversion. If photothermal conversion was efficient, biological evaluation of the material would take place and a comparison between the effectiveness of both thermotherapies would take place.

Once a material has been reproducibly prepared, extensively characterised, proven biocompatible and highly converting either magnetic work or light to heat efficiently, a suitable timeframe would be determined that can be easily adopted in real-life scenarios. Towards this end, cell death against treatment time experiments would be performed and molecularly characterise the biochemical processes occurring to preferentially achieve apoptosis.

Lastly, the biodistribution of the material would be determined to assess the percentage of material reaching the tumour and assess whether this amount is sufficient for elevating the temperature at levels where malignant cells would die. These experiments should also prove if there is any need to re-evaluate the coating of the NPs in case first-pass metabolism limits their distribution.

2 Syntheses of Anisotropic Ferrite Nanoparticles

2.1 Introduction

Anisotropy is derived from Greek meaning ‘uneven behaviour’ referring to the directionally dependent physical or mechanical properties of a material. Relating to this work, shape and magnetic anisotropy will be considered; whether materials have a non-spherical shape such as cubes, rods, triangles etc. or having a preferential orientation to align their magnetic moment for each anisotropy type respectively. Both anisotropies can affect the performance of NPs in certain applications. For example, iron oxide nanorods were shown to induce a stronger magnetic field around themselves and therefore exhibit better T2 contrast in MRI compared to spherical NPs[56]. Iron oxide nanocubes[57] and clustered iron oxide (nanoflowers)[58] showed enhanced performance in MFH compared to their isotropic counterparts. For the above reasons, there is a great amount of work being done on developing such materials. To optimise such materials specifically for MFH, one needs to understand the relaxation mechanisms which allow magnetic NPs to produce heat which are explained in section 2.1.1.

2.1.1 Mechanisms of Magnetic Relaxation

To illustrate the enhanced performance of anisotropic against isotropic NPs one needs to explore the mechanisms of conversion of magnetic work to heat upon the application of an AMF[59]. Most anisotropic NPs are not superparamagnetic and hence their mechanisms differ based on their magnetic relaxation[10,16].

The heat release occurs by hysteretic or susceptibility losses; the latter shown by superparamagnetic particles and the former by all others. A ferri- or ferro-magnetic crystal responds to an external variation of a magnetic field in a retarded way known as hysteresis. Applying reversal cycles through an AMF, the internal energy of the system increases, some of which is released as heat as all energy forms do eventually[60]. Graphically, hysteresis manifests itself as a loop on an M(H) curve as shown in Figure 11[48].

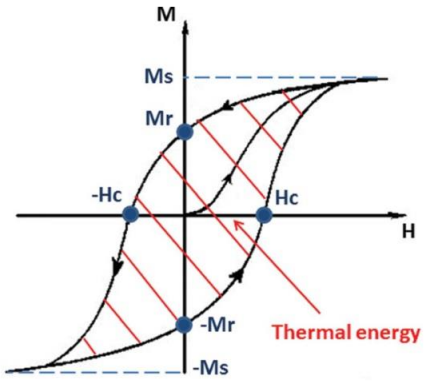

Figure 11: Hysteresis loop on a magnetisation cycle.

The power loss due to hysteresis is mathematically expressed in equation 1.

$$P_{FM} = \mu_0 f \oint H \, dM \qquad (1)$$

Where μ_0 is the permeability of free space, f is the frequency and H the magnitude of the field and M is the magnetisation.

Therefore, from the schematic above and equation 1, it seems that the larger the loop the greater the power released by the material. The anisotropic nature of the crystals poses a high-energy barrier for magnetisation reversal resulting in large coercivity (resistance to alignment with externally applied field), hence great heat release.

In the case of superparamagnetic particles and at high enough frequencies, the particles do not follow the reversal and show an out-of-phase susceptibility[59]. This also increases the internal energy of the particles subsequently translating to heat. When the magnetic field oscillates, the crystal can physically rotate to align or it can rotate the individual magnetic moments of the atoms to align with the reversed field; the processes are also known as Brownian and Néel relaxations respectively illustrated in Figure 12. They have different dependencies on the size and frequencies at which they manifest themselves but generally a combination of the two is assumed to take place. These relaxations are the cause of the out-of-phase susceptibility increasing the internal energy of the crystals.

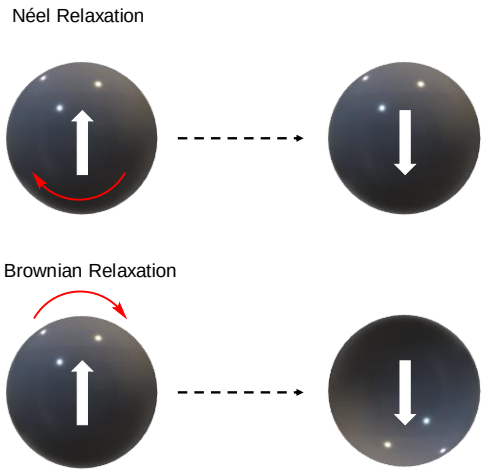

Figure 12: Néel and Brownian relaxations.

Losses from superparamagnetic materials are expressed as in equation 2.

$$P_{SPM} = \frac{\mu_0^2 \pi M_S^2 V \nu^2 H^2 \tau_{N/B}}{kt\left[1 + \left(\nu\tau_{N/B}\right)^2\right]} \quad (2)$$

Where V is the volume, v is the frequency, k is Boltzmann constant and $\tau_{N/B}$ is the Néel and Brownian relaxation times, respectively.

Ferro- and ferri-magnetic NPs release more heat compared to superparamagnetic NPs and hence there are intense efforts in producing anisotropic magnetic NPs. Due to this multi-angle enhanced performance of anisotropic magnetic NPs, γ-Fe_2O_3 nanoflowers were initially pursued followed by Fe_3O_4 nanocubes. Lastly, a two-step hydrolysis-reduction method was investigated to produce iron oxide nanorods from iron oxyhydroxide NPs.

2.2 Materials and Methods

2.2.1 Reagents

$FeCl_3.6H_2O$ (99%), branched PEI solution 50 wt% (M_w 750 kDa) and branched PEI (M_w 25 kDa), NaOH, diethylene glycol (DEG), N-methyldiethanolamine (NMDEA), $Fe(NO_3)_3.9H_2O$, diethyl ether, decanoic acid, tetradecanoic acid, octadecanoic acid, $Fe(acac)_3$ (99.9%), squalene, 65% $N_2H_4.H_2O$ (98%), 70% HNO_3 (99.999%) dibenzyl ether, $CHCl_3$ and n-hexane were purchased from Merck, UK. $FeCl_2.4H_2O$ (99%) was purchased from Honeywell, UK. Oleylamine (80-90%) and 37% HCl (trace metals) were purchased from Acros Organics, UK. Acetone (technical grade) was purchased from VWR, UK.

Ethanol (100%) was purchased from HaymanKimia Ltd. Trisodium citrate (99%) was purchased from BDH, UK. Water was purified by Purelab Ultra, Elga, UK. All chemicals have been used without further treatment.

2.2.2 Experimental Methods

2.2.2.1 Synthesis of γ-Fe_2O_3 Nanoflowers

For the synthesis of γ-Fe_2O_3 nanoflowers a previously described protocol was followed[26]. In detail, $FeCl_3.6H_2O$ (1.09 g, 4 mmol) and $FeCl_2.4H_2O$ (0.4 g, 2 mmol) were dissolved in a mixture of DEG (37 ml) and NMDEA (37 ml) in a three-neck round bottom flask (RBF). The solution was stirred for 1 h at room temperature (RT) to solubilise both precursors. Separately, NaOH (0.64 g, 16 mmol) was dissolved in a mixture of DEG (17.5 ml) and NMDEA (17.5 ml) under stirring at 80 °C to form a pale-yellow solution. Once the hour has passed, the NaOH solution was added to the solution of iron chlorides and stirred for 3 h. Subsequently, the reaction mixture was heated to 220 °C at a rate of 2 °C/min using an Oakton Temp 9500 advanced multiparameter controller and kept at 220 °C for 12 h. After the reaction mixture cooled to RT the NPs were magnetically separated and washed three times with a 1 : 1 v/v ethanol : ethyl acetate mixture (100 ml). The NPs were washed with 10% HNO_3 and a solution of $Fe(NO_3)_3.9H_2O$ (0.2 M, 20 ml) was added to the NPs and heated at 80 °C under stirring for 45 min to oxidise the NPs to γ-Fe_2O_3. After another wash with 10% HNO_3, the NPs were washed three times with acetone and once with diethyl ether. The solid product was redispersed in a trisodium citrate solution (0.002 M, 30 ml) to form a stable suspension.

2.2.2.2 Synthesis of Fe_3O_4 Nanocubes

To synthesise Fe_3O_4 nanocubes a recently developed protocol was followed[57]. $Fe(acac)_3$ (0.35 g, 1 mmol) was dissolved in dibenzyl ether (25 ml) in the presence of decanoic acid (0.7 g, 4 mmol) under a nitrogen atmosphere in a three necked RBF. After degassing under vacuum and replacing the atmosphere with nitrogen three times on a Schlenk line, the reaction mixture was heated in two steps. Initially, the mixture was heated to 200 °C at a rate of 5 °C/min and kept there for 2.5 h using a Julabo LC6 PID controller equipped with 2 platinum probes. Consequently, the mixture was heated to 290 °C with a rate of 10 °C/min and kept at reflux for 1 h. The reaction mixture was let cool

to RT and the NPs were precipitated by acetone and magnetically collected. The NPs were washed three times with acetone and stored in $CHCl_3$.

2.2.2.3 Synthesis of Elongated Iron Oxide Nanoparticles

Synthesis of β-FeOOH Nanoellipsoids. A general synthesis of β-FeOOH nanoellipsoids was previously described[56]. Briefly, $FeCl_3.6H_2O$ (5.4 g, 20 mmol) was added in water (100 ml) containing PEI. The mixture was heated at 80 °C in an oil bath for 2 h under magnetic stirring (500 rpm). The NPs were isolated by centrifugation (8000 g, 10 min), rinsed with acetone and ethanol sequentially and dried at 80 °C. The amount of PEI, its molecular weight and the reaction time have been varied to investigate the role of each parameter in the formation of β-FeOOH nanoellipsoids.

Reduction with Oleylamine. Oleylamine was used as a mild reducing agent. 200 mg of β-FeOOH nanoellipsoids were mixed with oleylamine (3.14 g, 11.7 mmol) in a three-neck RBF. Under a nitrogen atmosphere, the mixture was heated to 200 °C under magnetic stirring (500 rpm) for 4 h. The product was let cool down and washed three times with ethanol and centrifuged (8000 g, 5 min). The solid product was recovered from acetone and dried at 80 °C.

Reduction with Hydrazine. Hydrazine was employed as a strong reducing agent. 90 mg of β-FeOOH nanoellipsoids were dispersed in water (20 ml) in a three-neck RBF. The NPs were fully resuspended after 20 min of magnetic stirring. Approximately 1 ml of 65% $N_2H_4.H_2O$ was added to reach a pH value of 10.5 which was determined by Thermo Scientific Orion 3-Star pH meter. The mixture was refluxed at 100 °C under magnetic stirring (500 rpm) for 4 h. The reaction mixture was let to cool down and the product was washed with ethanol and acetone and centrifuged (8000 g, 5 min) three times. The NPs were dried at 80 °C.

2.2.2.4 Characterisation Methods

The NPs were visualised by transmission electron microscopy (TEM) using a JEOL JEM 1200-EX operating at an accelerating voltage of 120 kV using the software Gatan DigitalMicrograph. Samples were casted on carbon coated copper grids and air dried. Size analysis was performed by image analysis software Image J (National Institute of Health). X-ray diffraction (XRD) patterns

of powder samples were recorded at RT between 20-110° on a PANalytical X'Pert^3 equipped with a cobalt source (λ=1.789 Å) on transmission-reflection spinning mode. Thermogravimetric analysis (TGA) was performed using a DiscoveryTGA (TA Instruments) under a nitrogen atmosphere between RT up to 700 °C with a heating rate of 10 °C/min. Infrared spectra were recorded on a PerkinElmer Spectrum 100 attenuated total reflectance Fourier transformed infrared spectrometer (ATR-FTIR) on dry powder samples at RT accumulating 20 scans between 600-4000 cm^{-1} for each sample and analysed with the software Spectrum. Magnetic measurements were recorded on a Quantum Design MPMS 3 superconducting quantum interference - vibrating sample magnetometer (SQUID-VSM) between ±70 kOe at 300 K.

2.3 Results and Discussion

2.3.1 γ-Fe_2O_3 Nanoflowers

Nanoflower-shaped NPs have shown enhanced performance in MFH compared to isotropic NPs which makes them an attractive material for biomedical applications. Although their synthesis is a multi-step procedure spanning over two days, it is simpler compared to other high temperature thermal decomposition reactions as it is carried out at ambient atmosphere. Repeating the synthesis more than once revealed reproducibility issues which can be seen from the TEM images shown in Figure 13.

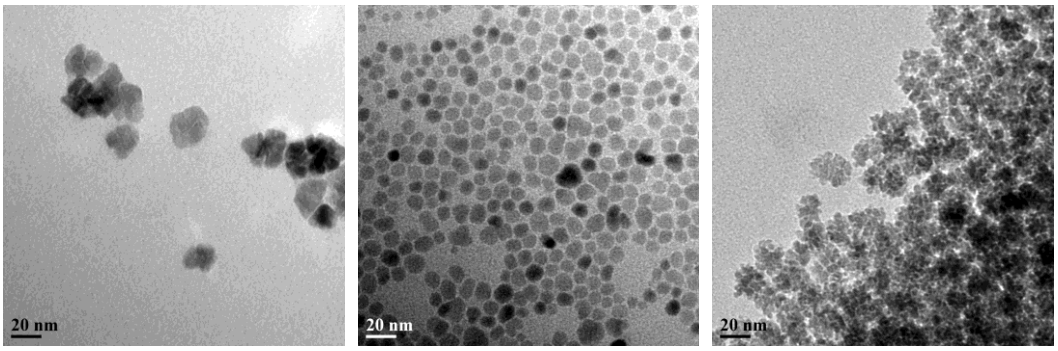

Figure 13: TEM images of NPs prepared from three independent experiments following the nanoflower synthesis protocol.

The morphology of the NPs obtained from repeating the nanoflower synthesis varies greatly. On occasions, the NPs would come out as clustered small crystallites to form one bigger nanoparticle whilst on other, bigger crystallites

would aggregate to form a nanoflower with bigger petal-like structures. Often the resulting NPs had a spheroidal shape instead. This would result in irreproducible performance. The formation of the NPs was followed by aliquoting to determine the point at which the synthesis would result in nanoflower-shaped NPs or not. To do this, aliquots were extracted from the reaction mixture at different time-points and observed under a TEM. NPs were counted using ImageJ by measuring at least 300 NPs.

Addition of NMDEA. In the first step of the reaction, a Lewis base, NMDEA, is added in the iron chloride precursors. This would initiate the nucleation part of the synthesis and hence it was investigated whether aging in that reaction mixture could produce nuclei of different sizes which could affect the final morphology and size of the NPs. Aliquots from the reaction mixture were taken between 0-120 min and imaged under a TEM. As it can be seen in Figure 14, the size of the nuclei remained constant throughout and hence this step was not considered to be influential in the final morphology.

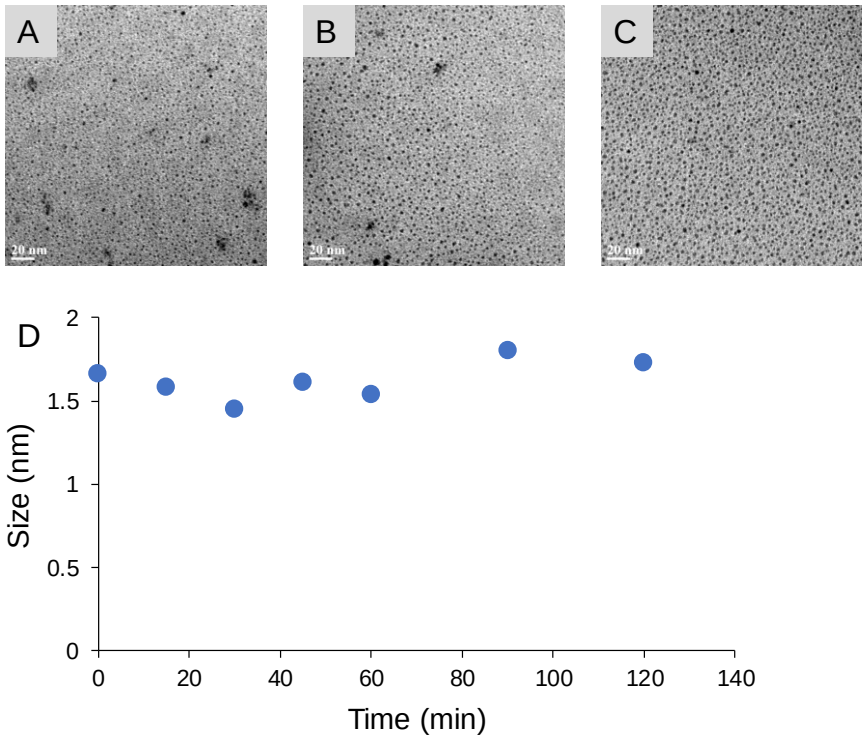

Figure 14: A), B) and C) TEM images of NPs produced after NMDEA addition at 30, 60 and 120 min respectively. D) Time-resolved size change after NMDEA addition as obtained from counting at least 300 NPs per aliquot from TEM images.

Addition of NaOH. The addition of NaOH in the polyol mixture of iron chlorides was studied during stirring at RT as well as during the heating-up to 220 °C. These experiments were carried out with an NMDEA stirring time of 1 h according to the published procedure. The TEM images of these aliquots are shown in Figure 15. The number of NPs was extremely low for any quantitative analysis because of the dilute reaction mixture and the little amount withdrawn from the reaction to prevent possible thermodynamic or kinetic factors interfering. Qualitatively, it can be observed that there is a time-dependent growth of the nuclei post NaOH addition to produce poorly defined 8-10 nm NPs.

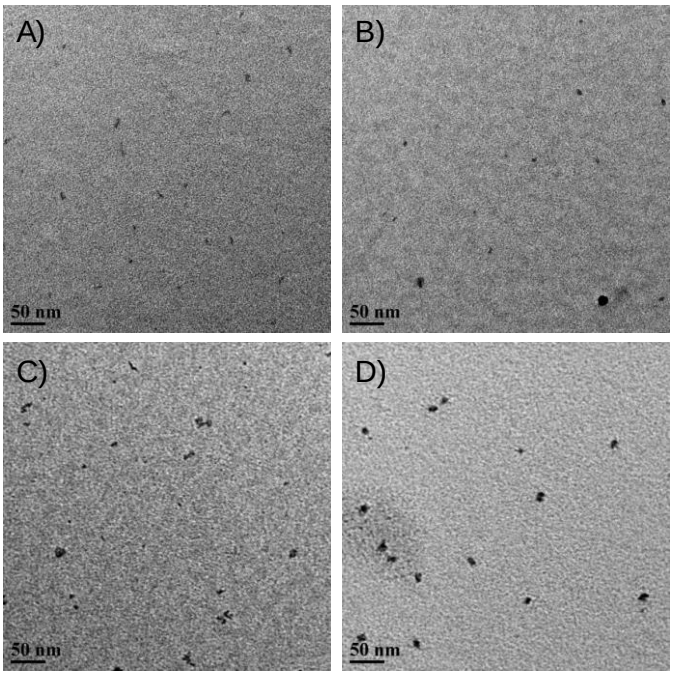

Figure 15: A), B), C) and D) TEM images of post-NaOH mixture addition after 1 h of NMDEA stirring at RT, aliquots taken at 0.5, 1, 2 and 3 h respectively.

According to the published procedure, after 3 h of stirring the two reaction mixtures together at RT, the flask was heated to 220 °C at a rate of 2 °C/min. This is the main growth phase of the reaction when the reaction mixture turns black and magnetic NPs can be separated thereafter.

The biggest morphological changes occur during the heating stage of the reaction as it can be seen from Figure 16 and as such it seems the most probable stage at which the final morphology of the NPs will be determined.

Due to the irreproducibility of the system, further investigation in this synthetic procedure was stopped at this stage as no firm conclusions could be obtained from repeating it.

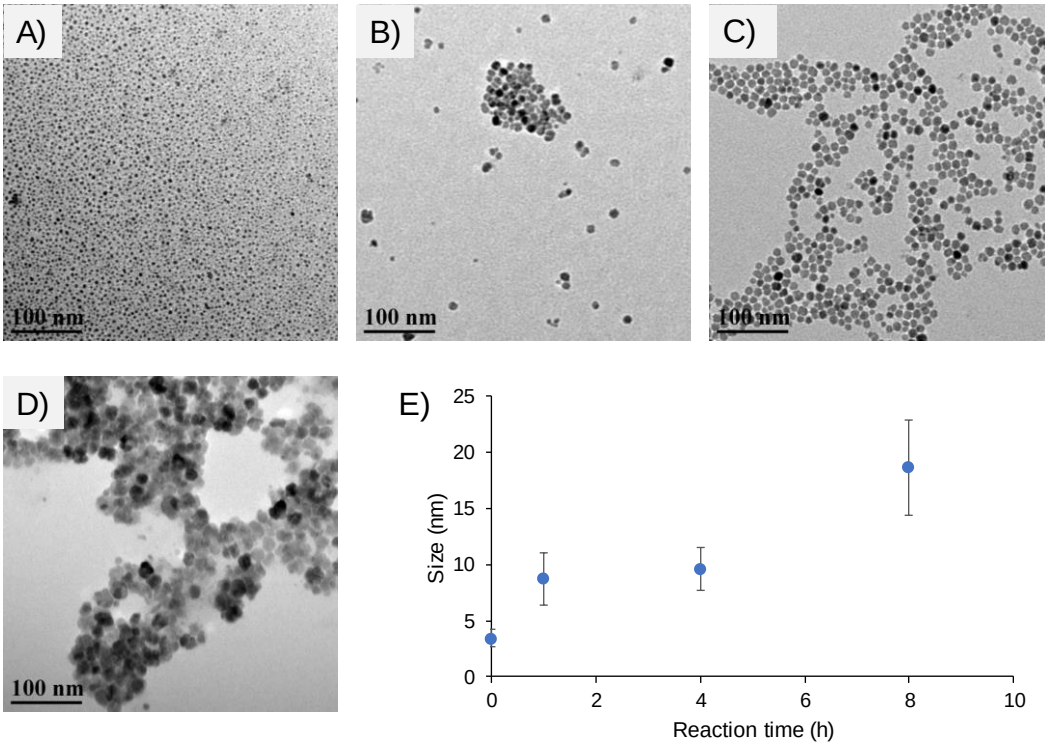

Figure 16: A), B), C) and D) TEM images of NPs formed after NaOH addition at 220 °C at 0, 1, 4 and 8 h respectively. E) Size analysis of the corresponding samples.

Factors Influencing the Reproducibility of γ-Fe_2O_3 Nanoflower Formation. It was not until recently, a publication addressed possible parameters which can affect the formation of the nanoflower morphology[61]. The authors concluded that the amount and timing of water present in the reaction seems to be a key factor in determining the morphological fate of the NPs. Additionally, they comment on the effects of various stirring methods and different heating-up protocols and how these, influence the final morphology. Ambient humidity does not seem like a possible source of water as these reactions are carried in open air and a well-ventilated space and in addition, the iron chloride precursors used are in their hydrated state. Ethylene glycols as well as NaOH are known to be hygroscopic materials, and these could introduce variability in the synthesis of these materials depending on how and for how long these materials have been stored. Even though they exhibit good

results in MFH, these difficulties in producing them might be a hindering factor towards their clinical translation.

2.3.2 Fe_3O_4 Nanocubes

The next highly performing system in MFH is Fe_3O_4 nanocubes. This synthetic procedure is more complex than the synthesis of γ-Fe_2O_3 nanoflowers in the sense that it requires airless and waterless conditions as well as specialised equipment. The synthesis involves the thermolysis of a commercially available precursor, $Fe(acac)_3$, in the presence of decanoic acid in dibenzyl ether. This synthesis also requires a controlled heating rate. As observed with the previous anisotropic formation of iron oxide NPs, this synthetic procedure was also difficult to reproduce as shown in Figure 17.

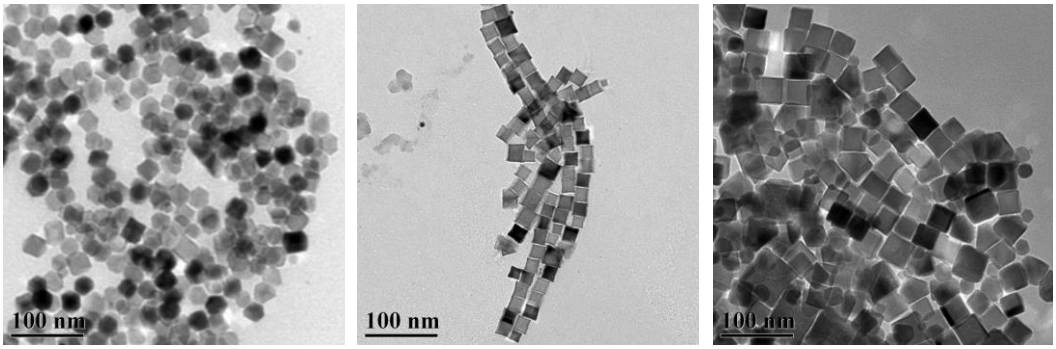

Figure 17: TEM images of three independent syntheses of Fe_3O_4 NPs made according to the published procedure for Fe_3O_4 nanocubes.

Heating-up. The heating up of the reaction was followed by aliquoting at both heating steps of the reaction, Figure 18A.

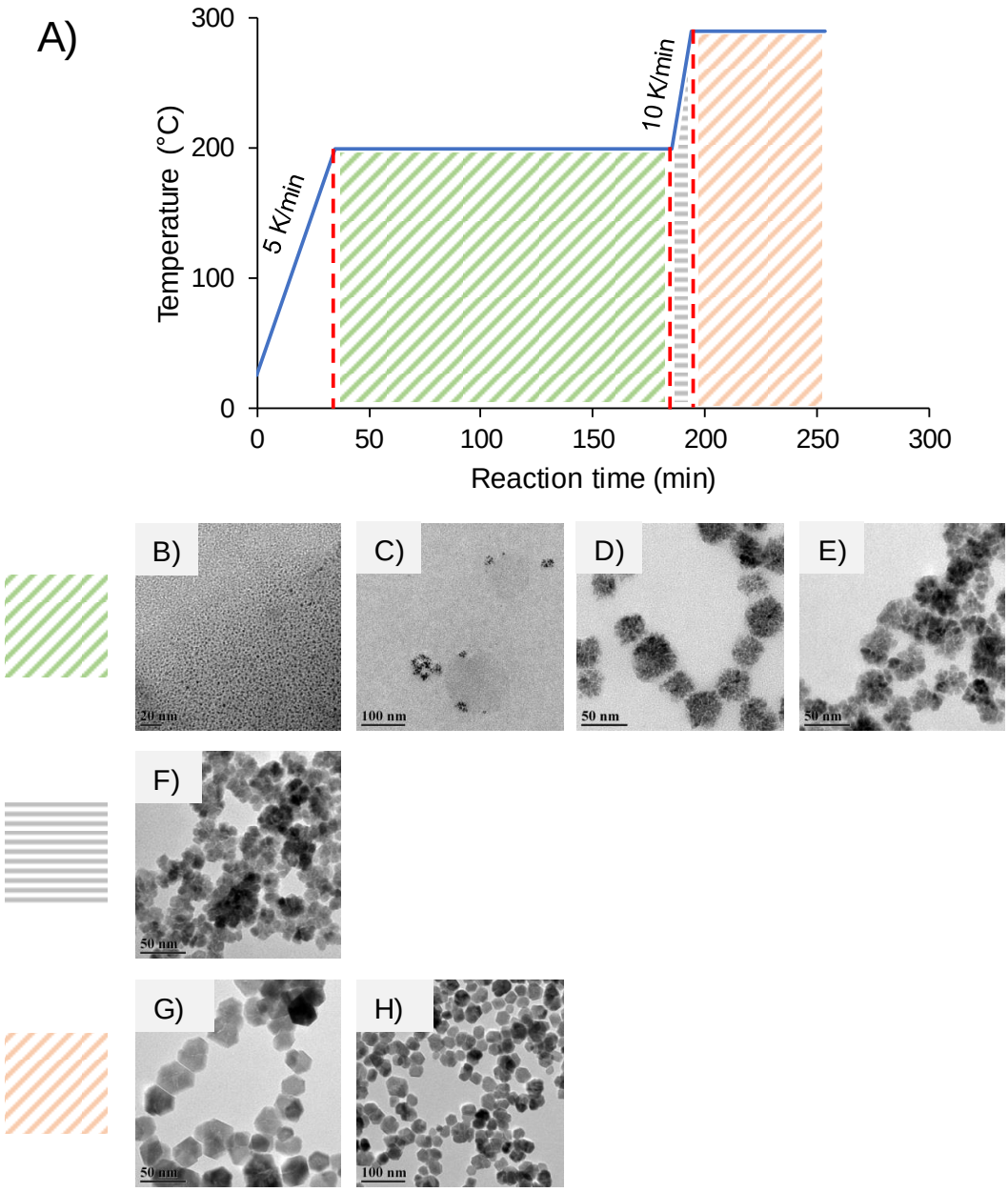

Figure 18: A) Heating-up profile of Fe_3O_4 nanocubes procedure colour-coded for the three main stages of the reaction. B), C), D) and E) TEM images obtained by aliquoting the reaction mixture at 0, 30, 60 and 150 min covering the whole span of the first heating plateau at 200 °C. F) TEM image of aliquot taken at 270 °C during the second stage of heating-up and G) and H) TEM images of aliquots taken at 15 and 45 min after refluxing at 290 °C.

During both heating stages there are significant morphological changes. Not only the size of the nuclei grows, they then aggregate in a regular fashion to form clusters as shown in Figure 18B-E. These clusters have poor crystallinity which increases as the temperature is further increased evidenced by the

higher definition of the NPs under the TEM. As the temperature is increased to 290 °C the clusters seem to fill up (Figure 18F-H) from additional iron as more precursor is deposited due to quick decomposition (decomposition temperature of $Fe(acac)_3$ is 200 °C, Figure 19). The final product even though faceted, is not the defined cubic shape shown in literature.

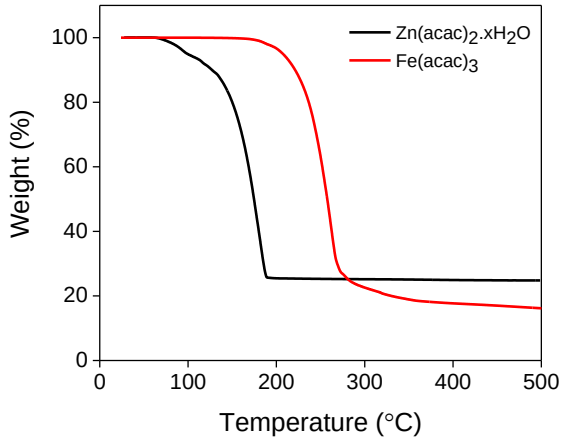

Figure 19: TGA of $Fe(acac)_3$ and $Zn(acac)_2.xH_2O$ under nitrogen.

Effect of Surfactant. It has been previously shown in high temperature reactions used to produce iron oxide NPs, that in the presence of fatty acids, an intermediate complex is formed between the iron and the surfactant[62]. This has implications at the consequent decomposition temperature of the precursor and hence affecting the nucleation and growth of a given crystallisation procedure. To this end, the surfactant was varied from decanoic to tetradecanoic and octadecanoic acid to investigate the effect on the resulting NPs in attempts to separate nucleation from growth to produce cubic NPs reproducibly.

It can be seen in Figure 20 that the longer the carbon-chain length of the fatty acid, the bigger the cubic edge of the resulting NPs. This might be a direct precipitate of different decomposition temperatures such as less early decomposing material being present, and more material being available for deposition during growth at higher temperature. These reactions also suffered irreproducibility.

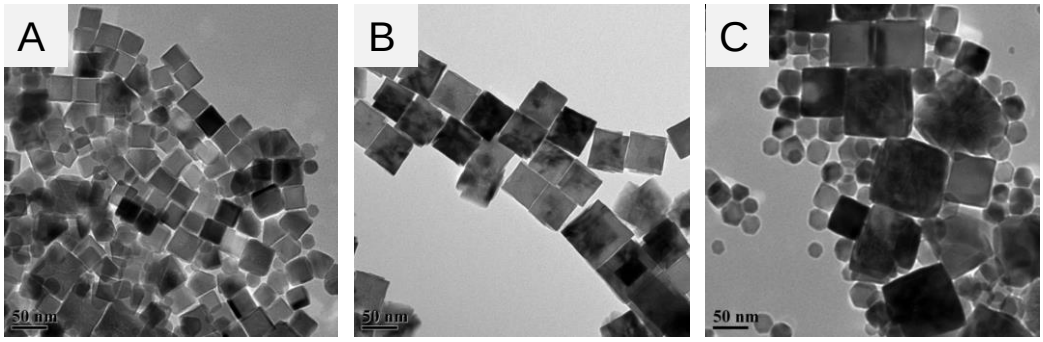

Figure 20: TEM images of Fe_3O_4 nanocubes prepared in the presence of A) decanoic, B) tetradecanoic and C) octadecanoic acids.

The reaction temperature was dropping after reflux with violent eruptions which the original authors recently addressed by changing the solvent from dibenzyl ether to squalene[63]. Our results with the new proposed solvent also did not result in the cubic morphology reported and hence this system was abandoned.

2.3.3 β-FeOOH Nanoellipsoids

Reaction Scale-up. The amount of β-FeOOH nanoellipsoids obtained with the published procedure was inadequate and was limiting the characterisation and future use of the product. To obtain sufficient characterisation data and expedite the development of β-FeOOH as potential precursors for the synthesis of magnetic NPs, the scalability of the reaction was initially assessed. For the scaled-up syntheses, two PEI with different molecular weights (25 and 750 kDa) were separately used and the amount of all reagents was increased by a factor of two. Both reactions were successfully scaled-up as it was confirmed from TEM images shown in Figure 21 producing morphologically identical nanoellipsoids. Using TGA, the yield of the initial and scaled-up reactions was determined; it was found that the weight of the products had increased from 0.25 g to 0.76 g (10.5 and 16.3% yield respectively), corresponding to a yield increase of 55%. All further experiments were performed with the scaled-up reactions.

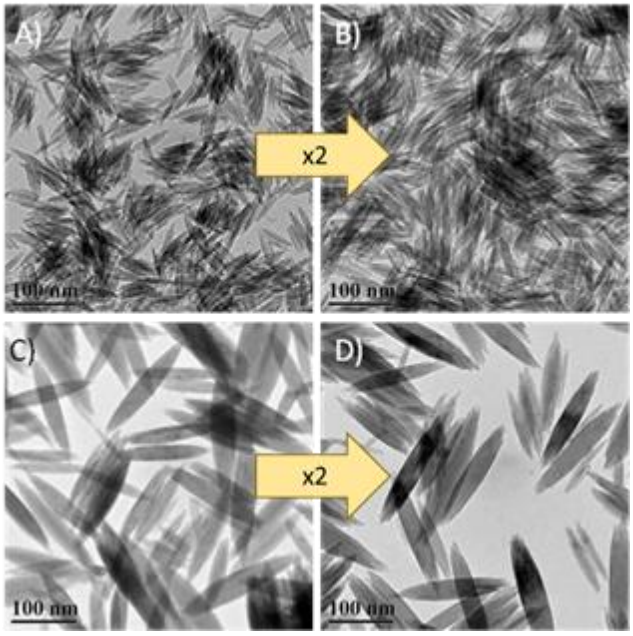

Figure 21: TEM images of β-FeOOH nanoellipsoids. A) and C) Nanoellipsoids prepared with 750 kDa and 25 kDa PEI respectively. B) and D) Their corresponding 2x scaled-up syntheses.

Time-dependent Growth of Nanoellipsoids. The growth of β-FeOOH has not been previously investigated with respect to reaction time. Aliquots have been taken from the reaction mixture at different times and TEM images were collected. The size and aspect ratio of the NPs were assessed using ImageJ for at least 100 NPs per condition. The reaction was performed in the presence of 0.2 g of 750 kDa PEI and aliquots were taken between 30 and 180 min. As it can be seen from Figure 22A, the length of the nanoellipsoids increases with time (p value=0.0005, 0.04, 3.4×10^{-24}) for student t-test between 60 and 90; 90 and 120; 120 and 180 min respectively). The different spatial growth rate of the anisotropic structure is observed here with a two times faster growth in the long axis in comparison with the short axis resulting in the same aspect ratio at all times as shown in Figure 22B.

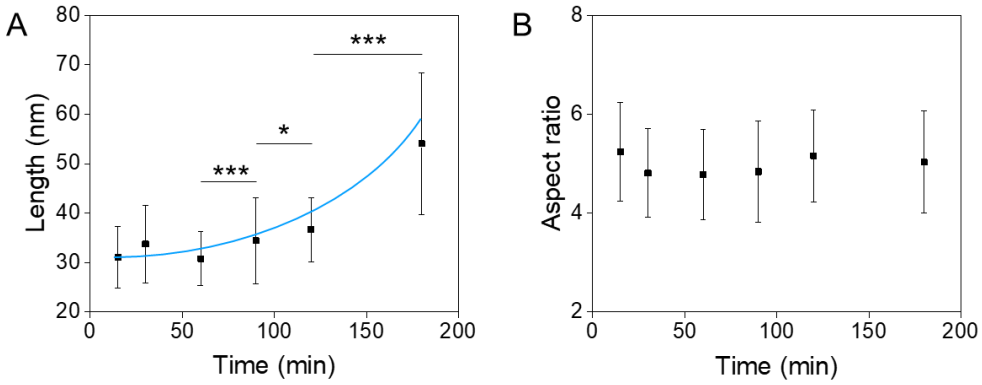

Figure 22: A) Long axis and B) Aspect ratio of β-FeOOH nanoellipsoids with increasing reaction time prepared with 0.2 g of 750 kDa PEI. The solid line is a guide to the eye. Values reported as mean ± SD. p-Values were calculated based on a two-tailed t-test: * indicates $p<0.001$ and * indicates $p<0.05$.**

Surfactants play a very important and complex role in NP synthesis in controlling facet kinetics[64], forming by-products crucial for some reactions[65], *in-situ* generation of precursors[28,65,66], acting as reducing agents[67] and even act as solvents in some cases[67]. Even more complex is the case of polymers, when it is possible to crosslink particles or engulf multiple nuclei at the same time[68], something not possible with singly functionalised molecules. To this end, the effect of PEI on the forming NPs was investigated.

Role of PEI on the Composition and Morphology of NPs. To increase understanding of the role of PEI in the synthesis of the material, the synthesis was performed in the presence or absence of different molecular weights of PEI. Interestingly, β-FeOOH phase was obtained in all cases as shown in Figure 23A.

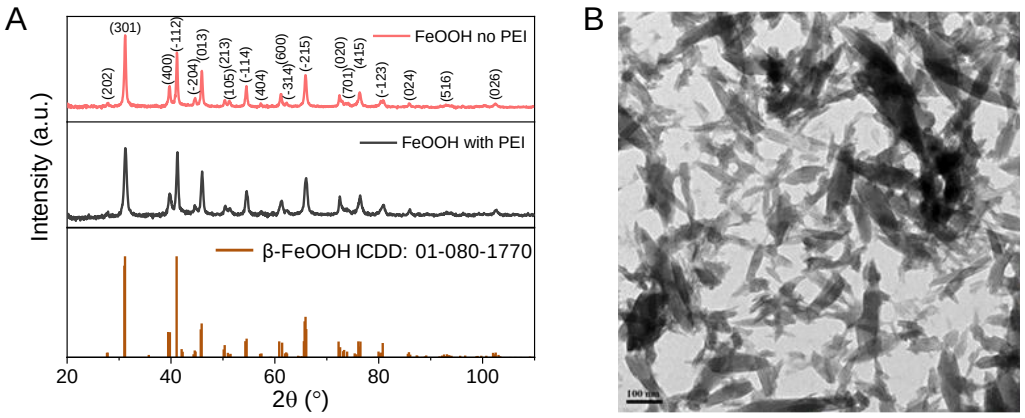

Figure 23: A) XRD patterns of NPs formed in the presence and absence of PEI. B) Synthesis of β-FeOOH in the absence of PEI at 80 °C for 2 h.

Similar to the NPs prepared in the presence of PEI, NPs obtained in the absence of PEI also exhibit an elongated structure although of much less definition and homogeneity, shown in Figure 23B. The elongated morphology observed in the absence or presence of PEI is a result of the monoclinic crystal structure of β-FeOOH favouring anisotropic growth[69]. In combination, the data suggest that PEI plays a role in determining morphology predominantly while the composition is independent of whether PEI is present. The length of the nanoellipsoids was shown to depend on the amount of PEI used. The more PEI (25 kDa) used led to a decrease in the length of the long axis of the NPs from 225 nm to 25 nm as shown in Figure 24. The aspect ratio of the ellipsoids remains the same at a value of 6 and therefore the amount of PEI can be used to tune the size of the resulting β-FeOOH nanoellipsoids while retaining the same aspect ratio. The homogeneity of the nanoellipsoids remains high over the PEI amounts tested (6-300 mg).

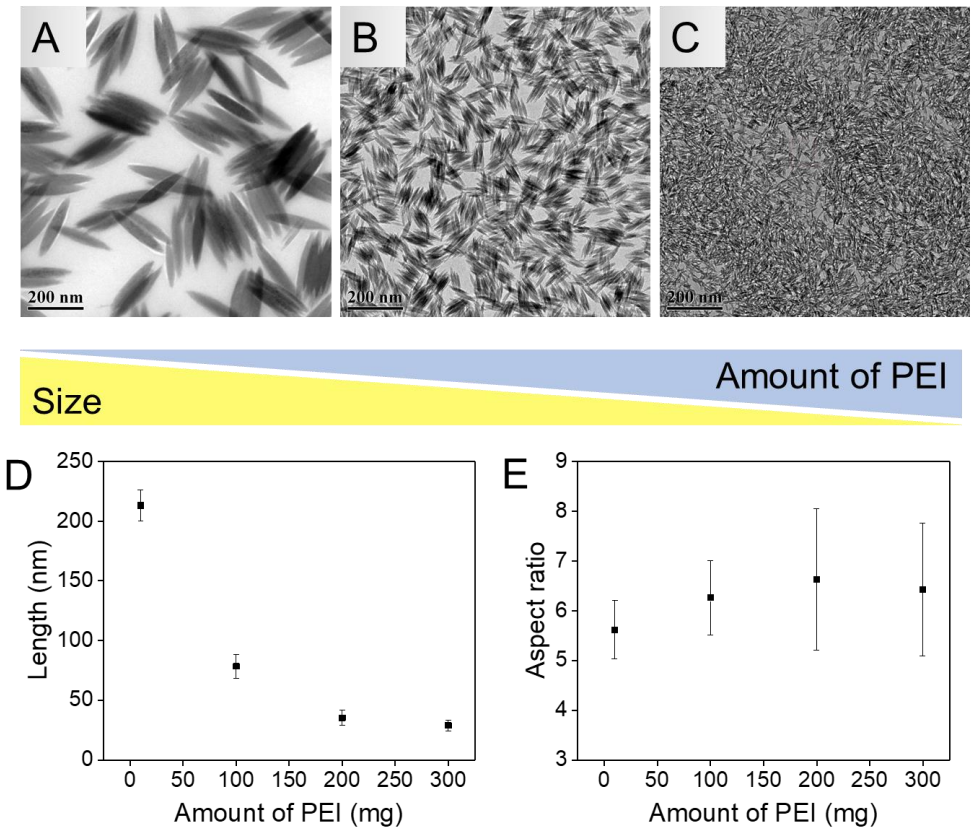

Figure 24: A), B) and C) TEM images of β-FeOOH nanoellipsoids synthesised with 10, 100 and 300 mg of 25 kDa PEI respectively. D) Size and E) Aspect ratio change with different amount of PEI.

A similar trend is observed with PEI with a molecular weight of 750 kDa for both the size and the aspect ratio of the NPs with the length of the nanoellipsoids varying between 50-25 nm and a constant aspect ratio of 5 as shown in Figure 25.

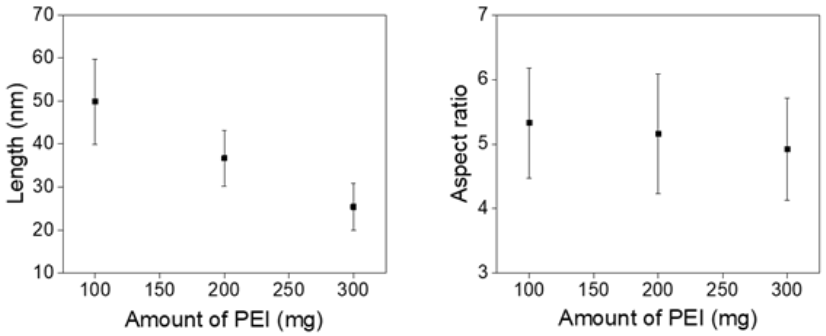

Figure 25: Length (left) and aspect ratio (right) changes of β-FeOOH nanoellipsoids with different amount of 750 kDa PEI.

As β-FeOOH is paramagnetic, the reduction of these nanoellipsoids with both mild and strong reducing agents with variable experimental conditions, to form anisotropic Fe_3O_4 NPs were studied.

Effects of Oleylamine High Temperature Reaction With β-FeOOH on the Composition, Morphology and Magnetic Properties of NPs. It was previously reported that oleylamine could reduce β-FeOOH to Fe_3O_4 as solid nanorods[56]. This method was employed to convert the nanoellipsoids to Fe_3O_4 but instead porous nanoellipsoids of an FeOOH phase with orthorhombic crystal habit were obtained as shown in Figure 26A and B

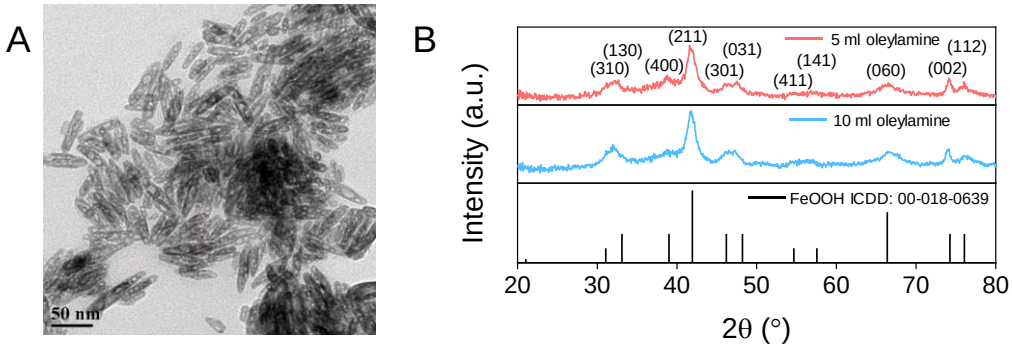

Figure 26: A) TEM image of oleylamine reduced β-FeOOH nanoellipsoids with voids visible. B) XRD patterns of oleylamine reduced β-FeOOH nanoellipsoids.

The pores could be exploited for potential application in drug delivery. The porous and hollow ellipsoids are believed to be the result of the dehydration of the oxide-hydroxide to form an oxide[70]. Chandy *et al.* indicated that the removal of chloride and water molecules from the tunnels in the β-FeOOH crystal structure are partially removed due to the thermal treatment[71]. Consequently, there is a contraction in the crystal lattice changing from the monoclinic structure of β-FeOOH to an orthorhombic FeOOH before converting to α-Fe_2O_3. This is true in this case of reacting with oleylamine at high temperature. It is also stated that further heating treatment at 320 °C of this FeOOH would result in α-Fe_2O_3 as with all iron oxide-hydroxides[38]. The intensity of the peaks on diffraction patterns obtained from XRD is low suggesting poor crystallinity, which might be due to a transitioning phase in-between the oxide-hydroxides and the oxide phases. Previously, a single condition has been used to reduce β-FeOOH to iron oxide. Herein, different

experimental parameters were investigated such as the amount of oleylamine, reaction time and temperature in attempts to preserve the shape and control the extent of phase transformation to increase the crystallinity.

The amount of oleylamine used during the reaction did not make a difference with regards to the material formed as it can be concluded from XRD data shown in Figure 26B. Similarly, the size of the resulting NPs also remained constant with changing the amount of oleylamine used (Figure 27A-C). Oleylamine was found to coordinate on the surface of the NPs by infrared spectroscopy (Figure 27D).

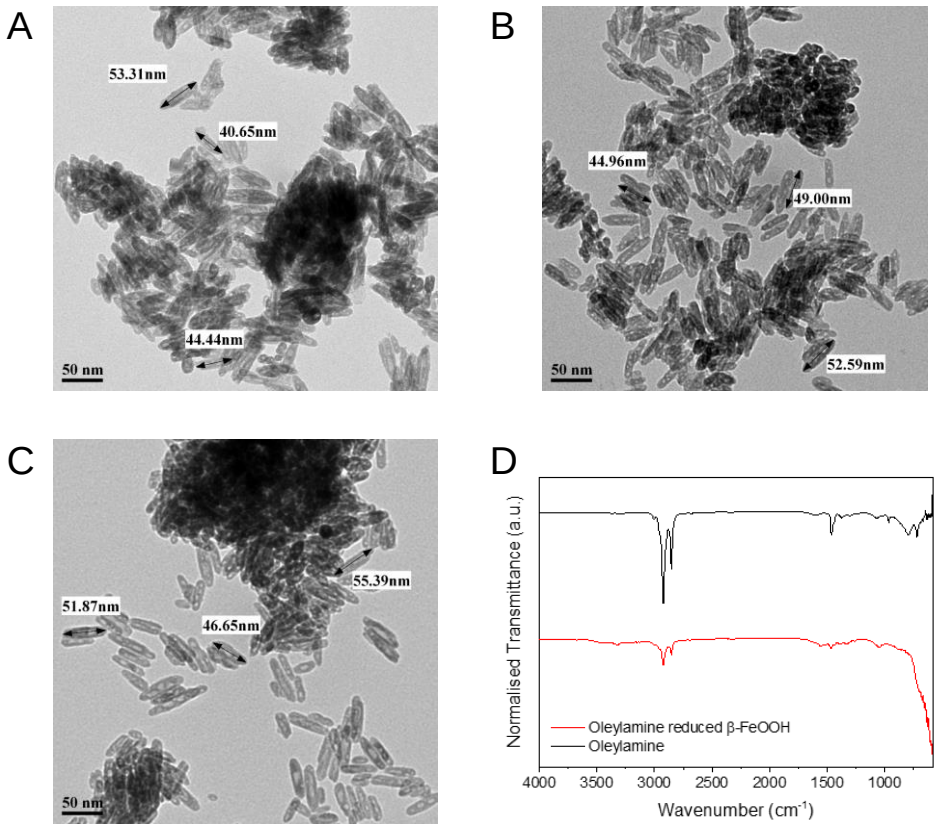

Figure 27: TEM images of β-FeOOH nanoellipsoids reduced by A) 5 ml, B) 10 ml and C) 15 ml oleylamine. Numbers are indicative of the length of the nanorods in each region in the TEM image at each condition. D) ATR-FTIR spectra of oleylamine and oleylamine reduced NPs.

Even though the colour of the NPs changes from light brown before reaction with oleylamine to black after reaction, which is indicative of Fe_3O_4 formation,

the magnetic behaviour of the resulting particles was almost purely paramagnetic as it can be seen from magnetometry measurements shown in Figure 28A. The nanoellipsoids, after reaction with oleylamine, have a shorter long axis by approximately 10 nm while their width remained the same, essentially decreasing their aspect ratio. The reaction time seems to have a small effect on the magnetic properties of the material as shown in Figure 28B**.** From the shape of the magnetisation curve, it can be seen that a paramagnetic component of FeOOH remains in the material because a plateau is not reached even at high applied magnetic fields although an iron oxide ferrimagnetic phase is formed in higher extent as indicated from the steep increase of magnetisation at low applied magnetic fields which is absent at shorter reaction times.

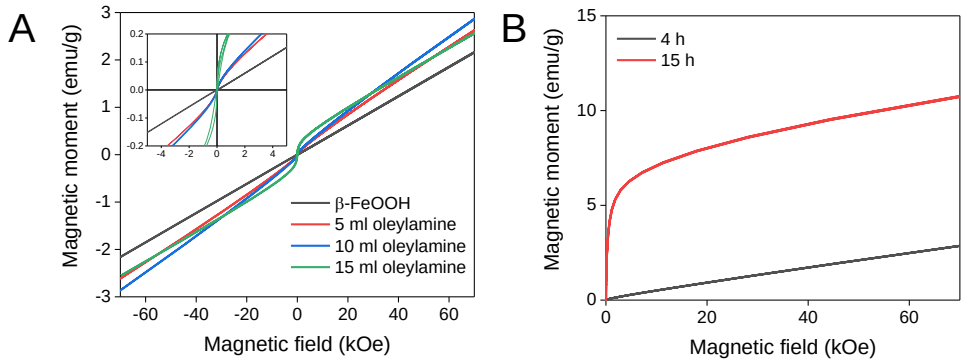

Figure 28: A) M(H) plots of β-FeOOH nanoellipsoids reduced with different amounts of oleylamine. B) M(H) plots of oleylamine reduced β-FeOOH nanoellipsoids at different reaction times

Lastly, the reaction temperature was further increased to 250 °C to overcome any thermodynamic or kinetic barriers for atom rearrangement and promote the formation of highly crystalline materials. The temperature increase resulted in phase transformation to Fe_3O_4 to a great extent with only a small contribution of FeOOH as shown from the XRD measurement (Figure 29B). The magnetic properties increased manifold to values typical of high-quality magnetic NPs as indicated in Figure 29C. Unfortunately, the morphology of the resulting NPs is lost, and a variety of shapes are formed including cuboid and parallelepiped shapes (Figure 29A).

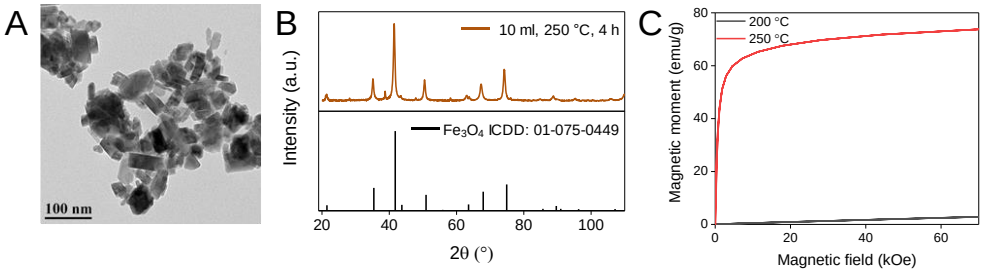

Figure 29: A) TEM image and B) XRD of NPs reduced with oleylamine at 250 °C for 4 h. C) M(H) plots of oleylamine reduced β-FeOOH at different temperatures.

Other high temperature reductions observed in literature often result in sintering, merging many NPs together losing the nano-size and morphological characteristics. To promote reduction and allow the reaction to proceed at lower temperature, hydrazine has been used as a stronger, water-miscible reducing agent.

Physicochemical Changes of β-FeOOH Induced by Hydrazine Reduction. Hydrazine has not been previously used to reduce β-FeOOH nanoellipsoids. As a stronger reducing agent than oleylamine, was employed to induce the reduction at lower temperature to prevent thermal dehydroxylation and possibly avoid porous/hollow structure formation. The transformation was shown to follow a dissolution-recrystallization mechanism through the formation of $Fe(OH)_4^-$ species in a basic medium[72]. A pH value of 10.5 was shown to induce the slowest rate of transformation within the window of 9-11.5 where this process takes place[38]. By adopting the pH value of 10.5 it was hypothesised that the transformation could be better controlled due to its slow kinetics possibly retaining the overall shape of the NPs. The reduction reaction of β-FeOOH with hydrazine is described in equation (3.

$$12\ \beta - \mathrm{FeOOH} + \mathrm{N_2H_4} \rightarrow 4\ \mathrm{Fe_3O_4} + 8\ \mathrm{H_2O} + \mathrm{N_2} \qquad (3)$$

The reduction with hydrazine is fast and occurs at 100 °C as opposed to 250 °C with oleylamine. The reaction mixture turns from brown to black after approximately 10 min of stirring and aliquots from 30-240 min show the same morphology at every time-point indicating that the reaction is complete after 30 min (Figure 30A-D). The XRD patterns reveal primarily an iron oxide phase with a few low intensity peaks indexed to α-FeOOH as shown in Figure 30E.

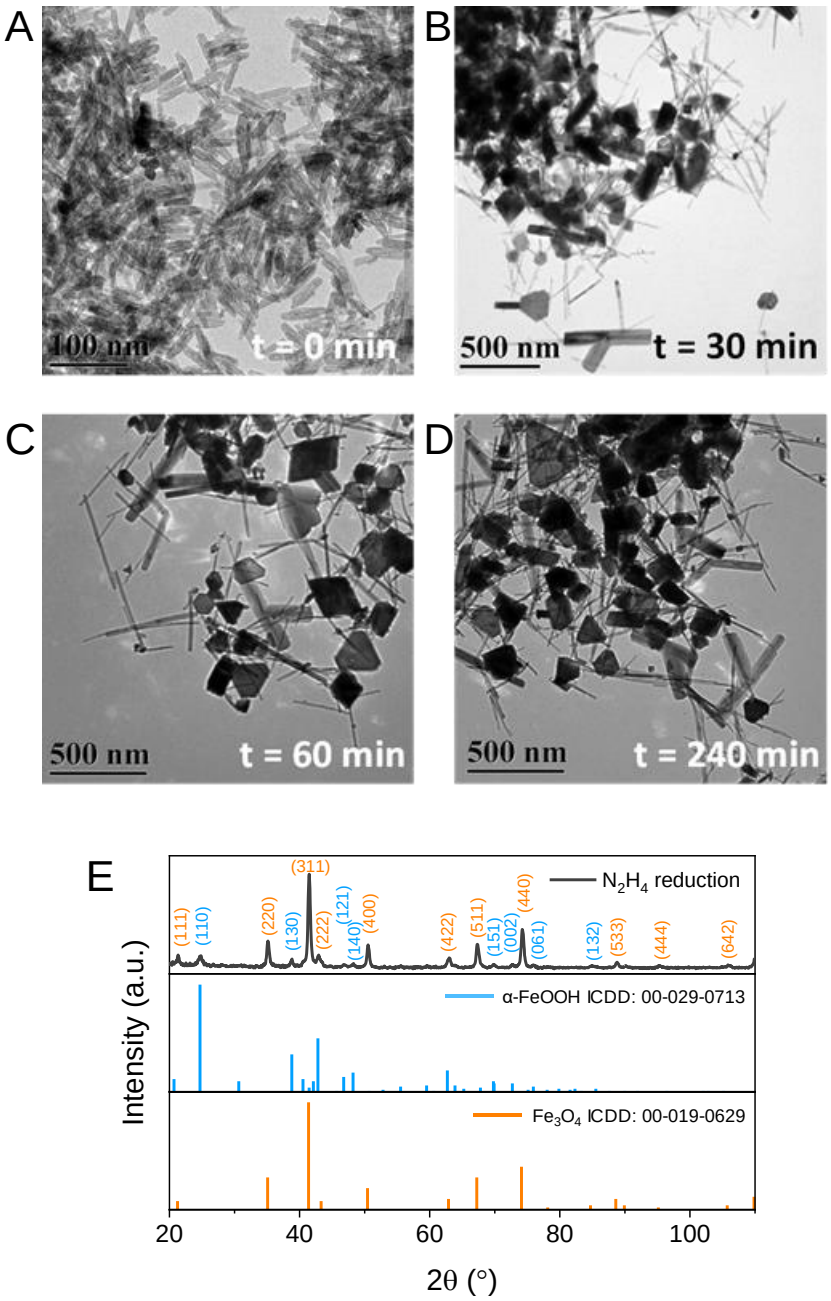

Figure 30: A) – D) are TEM images of hydrazine reduction at different reaction times. E) XRD pattern of N_2H_4 reduced β-FeOOH nanoellipsoids at 100 °C after 4 h reaction. Indexed reflections are colour-coded with respect to the reference patterns.

The resulting NPs from hydrazine reduction lose their ellipsoidal morphology producing faceted NPs including cuboids, wires and truncated triangles (Figure 30A-D). Due to loss of morphology, PEI was introduced into the reaction mixture to reduce the rate of reaction by coordinating on the surface of β-FeOOH and iron oxide as it forms, limiting further growth. Initially, 0.2 g of

PEI was introduced, and the reaction time was varied from 30 min to 4 h. At 30 min, hollow nanoellipsoids prevail on the TEM image with a few wires also being visible shown in Figure 31A. The TEM image of the prolonged reaction time shows mostly nanowires with some rod-shaped particles as well shown in Figure 31B. The XRD data show a mixture of Fe_3O_4 and α-FeOOH as shown in Figure 31C. When the reaction time was increased to 4 h, the product was an almost pure α-FeOOH phase with some low intensity Fe_3O_4 peaks (for clarity of Figure 31C, not all reflections have been indexed). The formation of α-FeOOH with increasing reaction time and disappearing of Fe_3O_4 can be monitored by the 220, 311 and 400 reflections of Fe_3O_4 at 35.1°, 41.3° and 50.4°, respectively. From the population of wires on the TEM images and in accordance with the XRD data it can be concluded that nanowires are composed of α-FeOOH and a longer reaction time favours the formation of α-FeOOH making this a polymorphic transformation rather than a reduction. The effect arises from the presence of PEI only since at the same experimental conditions but in its absence only Fe_3O_4 is obtained. This might be the result of strong coordination of the amine groups of the PEI with the iron atoms which might prohibit or considerably slow their desorption from the nanoellipsoids to perform the dissolution-recrystallization reduction mechanism and favour a polymorphic transformation instead.

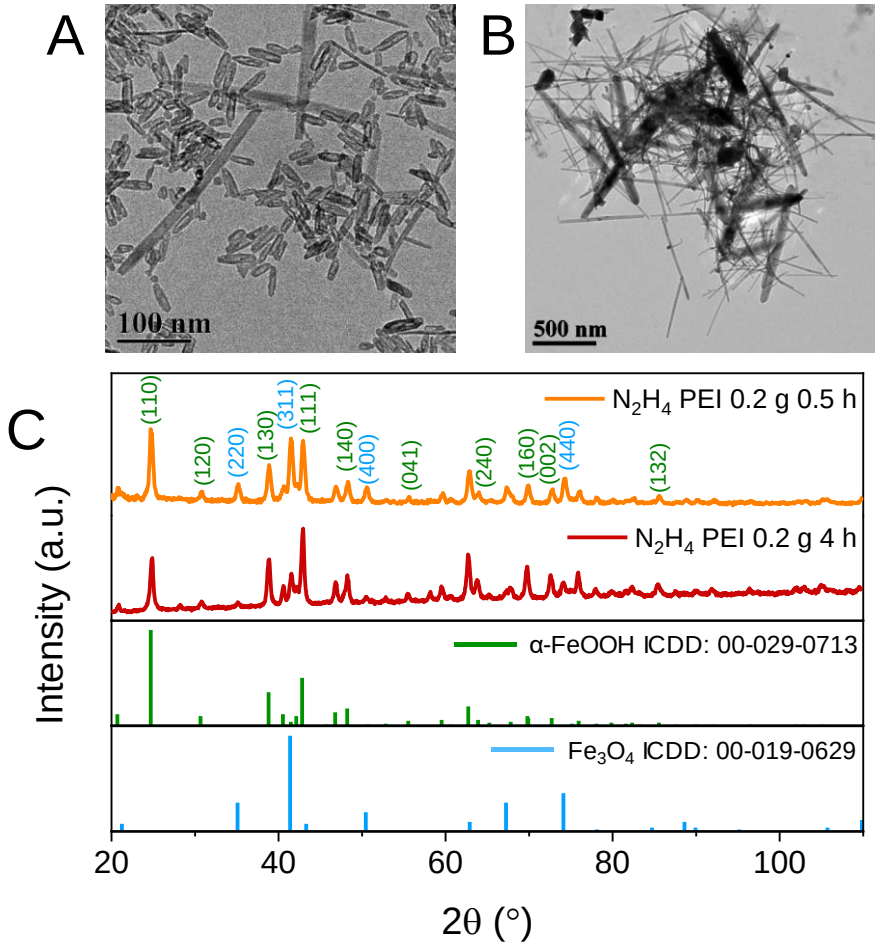

Figure 31: A) and B) TEM images of β-FeOOH reduced in the presence of N_2H_4 and 0.2 g PEI at 100 °C for 0.5 h and 4 h respectively. C) XRD patterns of the NPs in A) and B). Indexed reflections are colour-coded with respect to the reference patterns.

To further understand what the role of PEI is in these reactions its amount was doubled to 0.4 g and the reaction was carried out for 4 h. The composition of the resulting materials is similar with the 0.2 g PEI reaction, a predominant α-FeOOH with some Fe_3O_4 peaks although the TEM image shows smaller nanowires as shown Figure 32A and B. The products of reduction by hydrazine in the presence and absence of PEI were analysed by SQUID-VSM. The results shown in Figure 32C show a high saturation magnetisation (M_S) for NPs reduced in the presence of hydrazine only while when PEI was used the M_S was significantly lower which agrees with the XRD data of a dominant α-FeOOH phase. These data suggest that the formation of α-FeOOH is favoured

in the presence of PEI while the more magnetic phase Fe_3O_4 is formed in its absence.

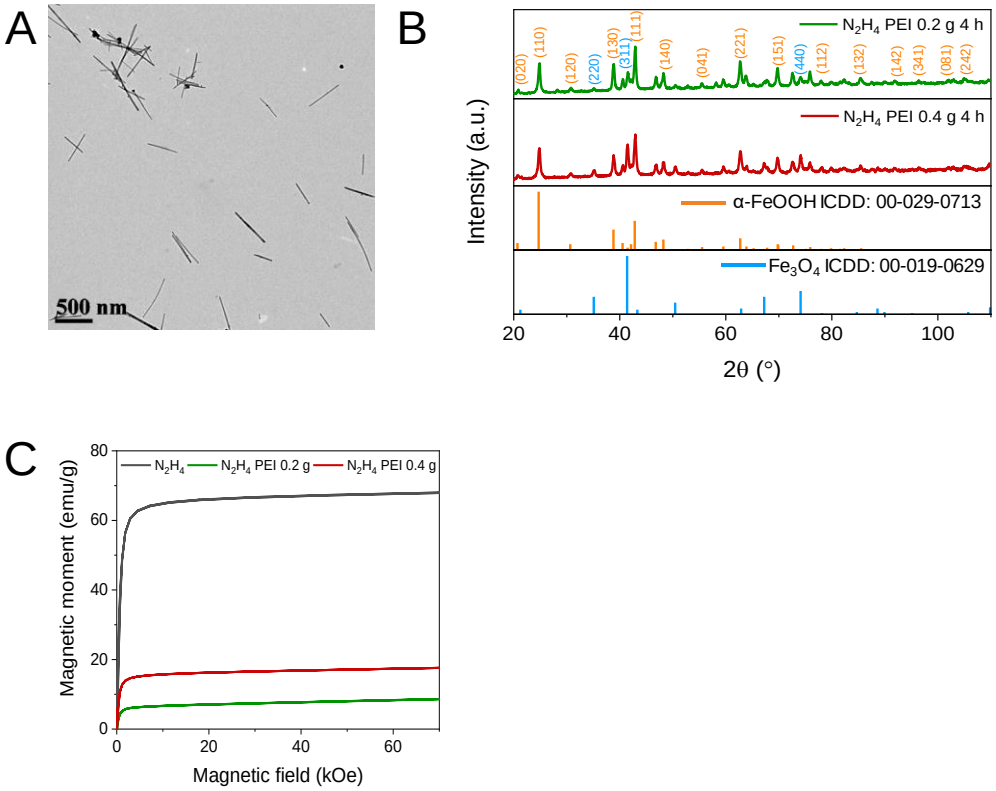

Figure 32: A) TEM image of β-FeOOH nanoellipsoids reduced by N_2H_4 at 100 °C in the presence of 0.4 g PEI. B) XRD patterns of β-FeOOH nanoellipsoids reduced by N_2H_4 at 100 °C in the presence of 0.2 and 0.4 g PEI. C) M(H) plots of β-FeOOH nanoellipsoids reduced by N_2H_4 in the absence or presence and different amounts of PEI.

2.4 Conclusion

The direct synthesis of anisotropic Fe_3O_4 NPs is challenging. Their advantages have been presented in literature although their preparation remains problematic and was hindering progress of further work. The synthesis of nanoflower NPs was studied in a time-resolved manner at all steps noting significant changes during the heat-up stage. Their formation seems complex and sensitive to environmental settings but the inability to reproducibly prepare them deemed it an unviable procedure. The preparation of cubic NPs was also monitored during the reaction revealing an impressive regular aggregation to form bigger entities. An effect of the surfactant used on the final cubic edge size was observed although their irreproducibility also

deemed this method impractical for further studies. The advances in controlling the size of β-FeOOH NPs will find use in oxide-hydroxide based catalysis, environmental remediation and possibly in anisotropic magnetic NPs synthesis all of which have been previously attempted using β-FeOOH based materials. A high degree of control over the synthesis of β-FeOOH nanoellipsoids has been achieved by changing the molecular weight and amount of PEI used in the reaction providing a wider range of sizes to scientists interested in iron oxide-hydroxide based nanomaterials. Experimental variables in the synthesis of β-FeOOH nanoellipsoids were studied and the PEI used during the preparation of the material was shown to play a morphological role only. The long-axis growth of the nanoellipsoids is time-dependent and affected by the molecular weight of the PEI used. The aspect ratio of the nanoellipsoids is independent of the reaction time but it can also be changed by changing the molecular weight of PEI. Oleylamine used as a mild reducing agent to convert β-FeOOH nanoellipsoids to iron oxide produced porous nanoellipsoids at all reaction times and amounts tested at 200 °C but magnetic measurements and XRD did not show a ferrite material. Increasing the temperature to 250 °C pushes the transformation to completion according to XRD and magnetometry studies which is accompanied by a loss of morphology. Hydrazine employed as a strong reducing agent also caused a loss of morphology when used alone but successfully forms Fe_3O_4 confirmed by XRD and magnetometry fast and at lower temperature. When PEI is present during reduction with hydrazine, the morphology is retained, hollow NPs are observed along with a mixture of Fe_3O_4 and α-FeOOH whose ratio is dependent on the amount of PEI present in the reaction. From the experiments performed herein, it is shown that when phase transformation occurs a loss of morphology is also observed while when the morphology is preserved a polymorphic transformation takes place instead of reduction indicating the need for further studies to achieve the formation of anisotropic iron oxide NPs by using FeOOH materials as precursors.

3 Novel Bio-Magnetic Nanomaterial Development and Physicochemical Characterisation

3.1 Introduction

Magnetic NPs are of interest in various fields and their M_S is of paramount importance in many such as drug delivery[73,74], bio-separation[75,76] and MFH[77]. More complex systems are pursued to enhance the magnetic properties of magnetic materials including metallic NPs[78], their alloys[79] or core-shell architectures[80]. Such materials are difficult to prepare, they suffer from extensive and immediate oxidation once exposed to air, consequently losing their magnetic properties and they may cause cellular damage when used *in vivo*[81]. To date, only iron oxide NPs have been approved by the FDA and European Medicines Agency (EMA) despite them having limited magnetic properties. Alternative materials to either iron oxide or metallic NPs are doped ferrites; spinel-based lattices into which different metal cations are introduced to alter the properties of the material. Such materials take the general form $M_xFe_{3-x}O_4$ where M is the dopant cation and examples of dopants include Ni^{2+}, Mn^{2+}, Zn^{2+}, Ho^{3+}, Co^{2+}, Mg^{2+}, Eu^{3+} and Cu^{2+} [16]. Doping can change the structural[82], electronic[83] and magnetic properties of materials[84,85]. Although many of them might find use in solar cells[83] or batteries[82] dopants for biomedical applications are limited due to the inherent toxicity of some elements.

NPs at the larger-size end of the superparamagnetic limit are pursued to achieve a smaller spin-canted layer-to-volume ratio which minimizes the reduction in the observed M_S value due to this effect[44]. The larger size might be beneficial in certain applications such as bio-separation or other *ex-vivo* applications but might limit others such as MFH and drug delivery due to hysteretic behaviour causing colloidal instability and the possibility of vascular occlusion[86]. Also, smaller sized NPs were shown to have prolonged systemic circulation[87], the ability to cross the blood-brain barrier[88], enhanced cellular uptake and sub-cellular size-dependent localization compared to their larger analogues[20]. Traditionally, smaller NPs suffer from lower values of M_S compared to larger NPs of the same composition due to a smaller magnetic

volume and the spin canting effect. A challenging need exists for a scalable, reproducible and facile synthesis to produce highly magnetic and biomedically relevant NPs.

Zn^{2+} has the second highest abundance among d-block metals in the human body after iron and its deficiency poses several risks to health such as oxidative stress and DNA damage[89,90]. Its importance in many enzymatic processes and food fortification with Zn^{2+} indicate the high tolerance to and need of Zn^{2+} for the human body to function properly[91]. Therefore, Zn^{2+} would be a biocompatible dopant for the preparation of magnetic ferrite NPs. Herein, it is demonstrated how a high temperature reaction with autogenous pressure can be used to prepare small, biocompatible, and highly crystalline zinc ferrite NPs as best-in-class. The preparation of zinc ferrite NPs with ten times less magnetic volume but similar M_S as the current highest reported value[29] is presented. The high reproducibility of the reaction and the ability to prepare iron oxide and zinc ferrite NPs with the same size and morphology allowed for an in-depth statistical study of various structural and magnetic properties such as unit cell parameter, lattice strain, M_S, Curie temperature (T_C), coercivity, blocking temperature (T_B) and effective, surface and magnetocrystalline anisotropies arising from Zn^{2+} doping. The surface of these high-quality NPs was functionalized with citrate in a one-pot functionalization step producing NPs dispersions whose magnetic and colloidal stability were assessed.

3.2 Materials and Methods

3.2.1 Reagents

$Fe(acac)_3$ (99.0%), $Zn(acac)_2.xH_2O$ (99.995% trace metal basis), 70% HNO_3 for ICP (99.999% trace metal basis) and 1,10-phenanthroline monohydrate (99%), triethylene glycol (TREG) (ReagentPlus® 99%), Zn standard for atomic absorption spectroscopy (TraceCERT®), Fe standard for ICP (TraceCERT®) and hydroxylamine hydrochloride (ReagentPlus® 99%) were purchased from Merck, UK. 37% HCl (trace metals) was purchased from Acros Organics, UK. Acetone (technical grade) was purchased from VWR, UK. Trisodium citrate (99%) was purchased from BDH, UK. $FeCl_2.4H_2O$ (99.0%) was purchased from Honeywell, UK. Sodium acetate anhydrous (ReagentPlus® 99.0%) was

purchased from Sigma Life Science, UK. Water was purified by Purelab Ultra, Elga. All chemicals have been used without further treatment.

3.2.2 Experimental Methods

3.2.2.1 Synthesis of Zinc Ferrites

High Temperature Autogenous Pressure. For the synthesis of $Zn_{0.4}Fe_{2.6}O_4$ NPs, $Fe(acac)_3$ (1.23 g, 3.5 mmol) and $Zn(acac)_2.xH_2O$ (0.14 g, 0.5 mmol) were dispersed in TREG (20 ml) by inversion and short bath sonication. The mixture was transferred into a 45 ml Teflon liner and assembled with an autoclave jacket. The mixture was heated to 250 °C at a rate of 5 °C/min using a Memmert UFP400 oven and kept at that temperature for 8 h after which it was let cool to RT. The NPs were precipitated with acetone using a 1 : 8 reaction mixture : acetone ratio at 9000 g for 10 min three times.

High Temperature Ambient Pressure. The synthesis of NPs under ambient pressure used the same reaction mixture in a three-necked RBF equipped with a Liebig condenser. Under no stirring, the flask was heated to the same temperature, rate and duration controlled by a Julabo LC6 PID controller equipped with two platinum probes.

Yield Quantification. Powder samples underwent elemental analysis with inductively coupled plasma-optical emission spectrometry (ICP-OES) to determine the metal fraction in the samples. The theoretical metal content assumed 100% conversion of the metallic content of the precursors to nanoparticulate form. The percent yield was calculated according to equation (5).

$$\text{Yield } \% = \frac{\text{actual } [\text{Fe} + \text{Zn}]}{\text{theoretical } [\text{Fe} + \text{Zn}]} \times 100 \qquad (5)$$

3.2.2.2 Surface Functionalisation

The crude NPs suspension could be functionalized by thermally equilibrating 8 ml of the suspension at 70 °C with intense magnetic stirring (1300 rpm). An equal volume of trisodium citrate solution (0.2 M) was added and the mixture was stirred for further 2 h. The product was collected by magnetic decantation

and washed with acetone (2 × 10 ml) after which the NPs were dispersed in the minimum volume of water to form stable suspensions (Figure 33A andB).

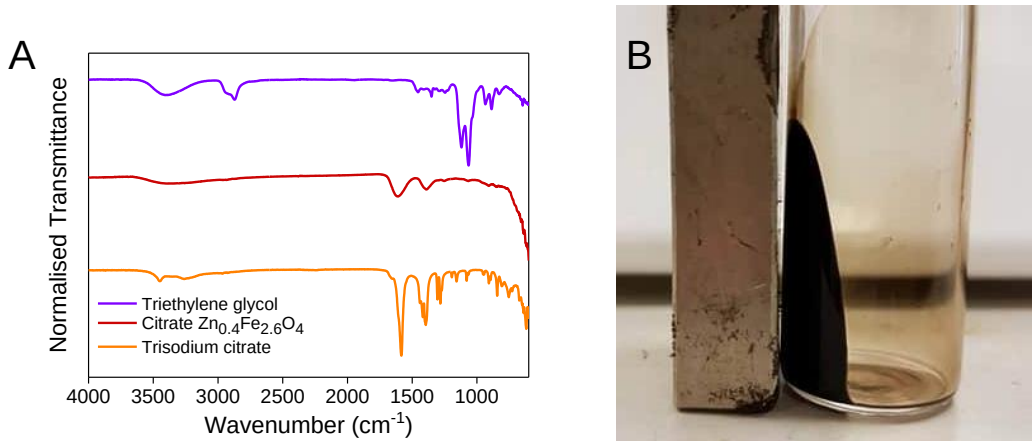

Figure 33: A) ATR-FTIR of TREG, trisodium citrate and citrate coated $Zn_{0.4}Fe_{2.6}O_4$ NPs. B) Digital image of stable citrate coated $Zn_{0.4}Fe_{2.6}O_4$ ferrofluid under the influence of a bar magnet.

3.2.2.3 Elemental Analysis

Atomic Emission Spectroscopy. The metallic content was assessed by ICP-OES and UV-Vis spectroscopy. For ICP-OES, a solid or liquid sample was digested in 70% HNO_3 and diluted to 1% for measurements. A calibration plot was prepared with ICP standards for iron and zinc and measurements were obtained with an Agilent Varian-720ES ICP-OES spectrometer.

Colourimetry. For UV-Vis analysis the sample was dissolved in 4 M HCl with mild heat at 65 °C and diluted if necessary. Hydroxylamine hydrochloride solution (50 µl, 0.15 M) were added in sodium acetate (450 µl, 1.5 M) solution. 200 µl of the digested sample were added and vortexed to facilitate the reduction of Fe^{3+} to Fe^{2+}. Finally, an acidic solution of 1,10-phenanthroline (300 µl, 0.06 M in 0.04 M HCl) was added and the vials were vortexed and stored overnight in the dark to facilitate the complexation. The same procedure was followed to prepare a calibration plot from $FeCl_2.4H_2O$ dissolved in 4 M HCl between 0.000625-0.02 mg_{Fe}/ml. Aliquots of 100 µl of each sample were plated in a clear 96-well plate and the absorbance values were taken at 510 nm on a Molecular devices SpectraMax Me^2 UV-Vis spectrometer.

3.2.2.4 Magnetic Properties Measurements

Magnetic measurements were performed on a Quantum Design MPMS3 SQUID-VSM. Powder samples were placed in gelatine capsules and immobilized with cotton wool. The gelatine capsule was placed in the interior of a diamagnetic plastic straw and measurements were taken between ±70 kOe. Data were corrected for diamagnetic contribution.

Zero-field cooled – field-cooled (ZFC-FC) measurements were recorded between 5-300 K at an applied field of 50 Oe.

The T_C was extracted from magnetoTGA measurements using a Discovery TGA, TA Instruments. Powder samples were placed in a single use aluminium crucible suspended on a platinum pan. The heating rate was set at 10 °C/min with a chamber nitrogen flow of 10 ml/min and a sample nitrogen flow of 25 ml/min. The temperature was increased from RT to 500 °C twice consecutively to first burn off ligands on the surface and then to reveal the T_C as a sudden decrease in weight due to loss of attraction to the electromagnet operating at 80% of its capacity.

3.2.2.5 Electron Microscopy

The NPs were visualized under a JEOL JEM 1200-EX electron microscope at an accelerating voltage of 120 kV. Samples were casted on a carbon-coated copper grid and air dried. High resolution TEM (HRTEM) and scanning transmission electron microscopy (STEM) with energy-dispersive X-ray spectroscopy (EDX) mapping were recorded on a Titan G^2 60-300 equipped with a coefficient spherical aberration image corrector operating at 300 kV. Elemental mapping was carried out in STEM with a condenser aperture of 70 µm and a windowless silicon drift detector. The sample was tilted 15° towards the EDX detector for acquisition.

3.2.2.6 X-ray Diffraction

Diffraction patterns of powder samples were recorded at RT on a PANalytical X'Pert^3 equipped with a cobalt source (λ=1.789 Å) between 20-110° on transmission-reflection spinning mode. The results were fitted and analysed by X'Pert HighScore Plus software.

Crystallite Size. The crystallite size was calculated by the Scherrer equation shown in equation (6).

$$\tau = \frac{K\lambda}{\beta \cos\theta} \tag{6}$$

Where τ is the crystallite size, K is the shape factor with a typical value of 0.9, λ is the wavelength of the X-ray source, β is the line broadening at half the maximum intensity and θ is the Bragg angle.

Lattice Strain. The lattice strain of the NPs was calculated based on the Williamson-Hall analysis as shown in equation (7).

$$\beta_{total} \cos\theta = \eta \sin\theta + \frac{K\lambda}{\tau} \tag{7}$$

Where β_{total} is the line broadening arising from all effects, θ is the Bragg angle, η is the lattice strain, K is the shape factor with a typical value of 0.9, λ is the wavelength of the X-ray source and τ is the crystallite size.

Lattice Parameter. To calculate the lattice parameter, Bragg's law, equation (8), was used to calculate the interplanar space d, which then relates to the lattice parameter according to equation (9).

$$n\lambda = 2d \sin\theta \tag{8}$$

$$d = \frac{\alpha}{\sqrt{h^2 + k^2 + l^2}} \tag{9}$$

Where n is a positive integer, λ is the wavelength of the X-ray source, d is the interplanar spacing, θ is the Bragg angle, α is the lattice parameter and h, k, l are Miller indices.

Percent Composition. The percentage of Fe_3O_4 and γ-Fe_2O_3 component in the synthesized Fe_3O_4@γ-Fe_2O_3 NPs was estimated using Vegard's law shown in equation (10).

$$\alpha_{A_{(1-x)}B_x} = (1-x)_{\alpha_A} + x_{\alpha_B} \tag{10}$$

Where α is the lattice parameter, x is the molar fraction and A and B are the two different materials.

3.2.2.7 Surface Monitoring

Infrared Spectroscopy. Surface ligands were identified by PerkinElmer Spectrum100 ATR-FTIR on dry powder samples at ambient conditions. Scans

were recorded between 600-4000 cm^{-1} and 20 scans were accumulated for each measurement. Spectra were analysed using the software Spectrum.

Thermogravimetric Analysis. Quantification of surface ligands was done by TGA under nitrogen flow up to 500 °C. Data were analysed by Trios software.

3.2.2.8 Photon Correlation Spectroscopy

Hydrodynamic Size. The hydrodynamic radius of the functionalized NPs was assessed by dynamic light scattering (DLS) measurements on a Malvern Zetasizer nano ZS operating with a 633 nm He-Ne laser.

Colloidal Stability. Solutions with different pH values or electrolyte concentrations were prepared and 1 drop of ferrofluid with a concentration of 10 mg_{Fe+Zn}/ml was added and mixed. The mixture was immediately filtered by syringe filtration (0.2 µm) and the filtrate was monitored for one week. All measurements were recorded at 25 °C in independent triplicates.

3.3 Results and Discussion

3.3.1 Nanoparticle Synthesis Under High Temperature with Autogenous Pressure

The synthesis of zinc ferrite NPs under high temperature and autogenous pressure was inspired by a previously developed polyol synthesis producing iron oxide NPs of high M_S values[92]. The reaction for the preparation of zinc ferrites involves the thermal decomposition of $Fe(acac)_3$ and $Zn(acac)_2.xH_2O$ in TREG at different ratios to produce zinc ferrite NPs with variable doping levels. As the temperature increases reaching the decomposition temperature of the precursors, the nucleation and growth steps of nanocrystal formation are initiated and decomposition products such as acetone, water and carbon dioxide build up and pressurize the vessel in accordance to the ideal gas law, PV=nRT, illustrated in Figure 34.

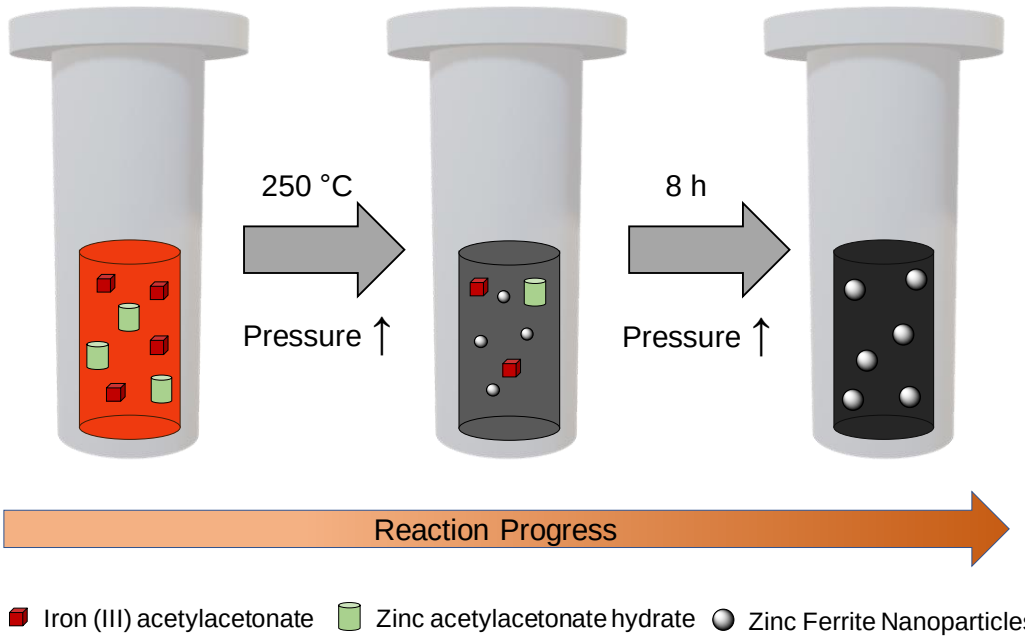

Figure 34: Schematic representation of the high temperature with autogenous pressure synthesis of zinc ferrite NPs in a Teflon-lined autoclave vessel.

To facilitate Zn^{2+} doping without affecting the size and morphology of the product, the total amount of $Fe(acac)_3$ and $Zn(acac)_2.xH_2O$ was kept constant while their ratio was systematically varied as shown in Table 2 to reproducibly produce zinc ferrite NPs with the corresponding composition as confirmed by ICP-OES or UV-Vis spectroscopy shown in Figure 35.

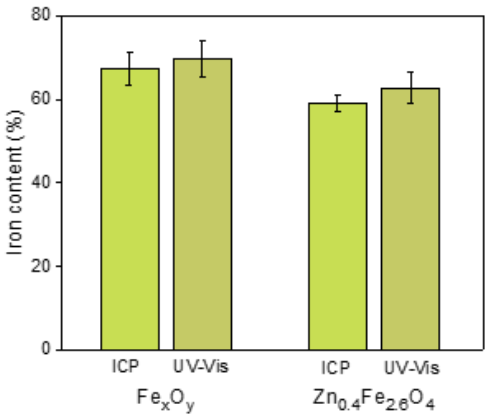

Figure 35: Comparison of ICP-OES and UV-Vis colourimetry on measuring the iron content of Fe_3O_4@γ-Fe_2O_3 and $Zn_{0.4}Fe_{2.6}O_4$ NPs (n=5, p>0.05).

The yield of the synthesis based on clean product was calculated according to equation (5) and was found to be 35 ± 2% for iron oxide and 40 ± 3% for $Zn_{0.4}Fe_{2.6}O_4$ NPs with no statistical difference between them based on a two-tailed t-test.

Table 2: Concentration of precursors used to prepare different Zn^{2+} doped ferrites. Values shown are averages of five syntheses per composition. The volume of TREG was constant at 20 ml.

Material	$Fe(acac)_3$ (mM)	$Zn(acac)_2.xH_2O$ (mM)
Fe_xO_y	200	0
$Zn_{0.2}Fe_{2.8}O_4$	187	13
$Zn_{0.4}Fe_{2.6}O_4$	174	26
$Zn_{0.7}Fe_{2.3}O_4$	153	47
$ZnFe_2O_4$	133	67

3.3.2 Material Characterisation

Structural Analysis. The size of the spherical $Zn_{0.4}Fe_{2.6}O_4$ NPs (Figure 36A) was compared with that of spherical iron oxide NPs produced by the same method and no statistical difference was observed as shown in Figure 36B and C after independent syntheses (n=3×300 NPs, $p>0.05$). HRTEM showed a single phase throughout the NP volume in both iron oxide and $Zn_{0.4}Fe_{2.6}O_4$ syntheses as shown in Figure 36D and E while the Fourier transform (FFT) patterns shown in Figure 36F and G reveal high periodicity within the NPs. Selected area electron diffraction (SAED) shows diffraction rings of spinel structures in both nanomaterials as indexed in Figure 36H and I. These results suggest that further analogous analyses between the two nanomaterials are possible since the iron oxide and $Zn_{0.4}Fe_{2.6}O_4$ NPs prepared by this high temperature with autogenous pressure method are morphologically and structurally the same.

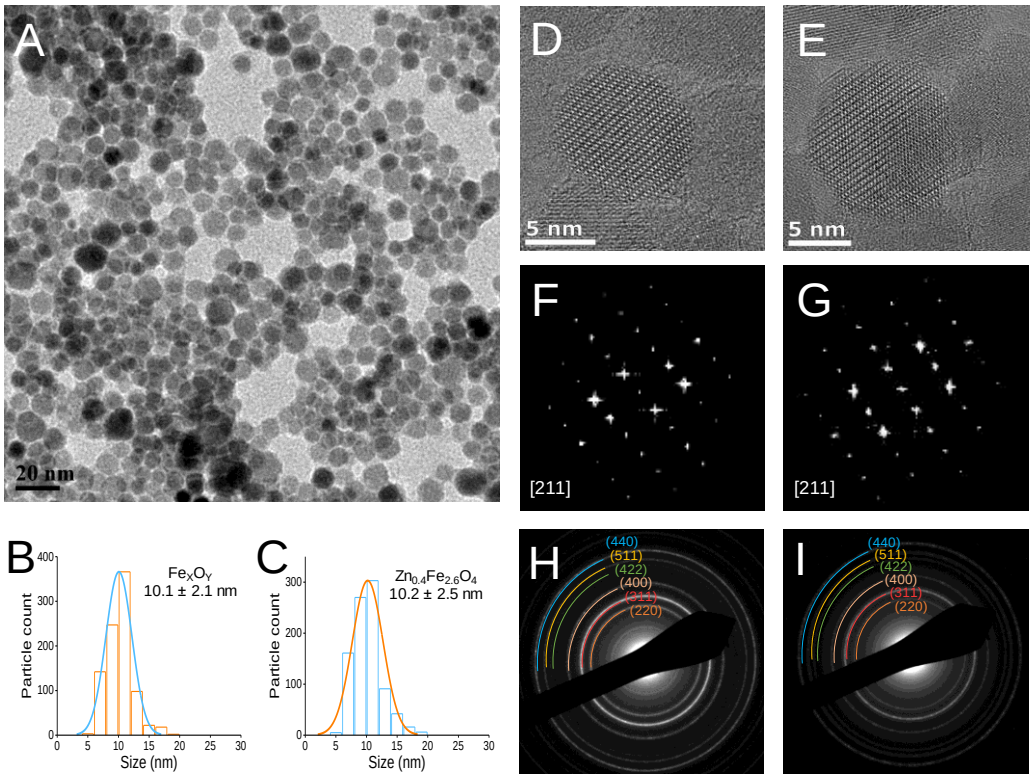

Figure 36: A) TEM image of $Zn_{0.4}Fe_{2.6}O_4$ NPs prepared under high temperature with autogenous pressure. B) and C) Size distributions, D) and E) HRTEM images, F) and G) FFT patterns down the [211] axis and H) and I) SAED patterns with denoted crystal planes for iron oxide and $Zn_{0.4}Fe_{2.6}O_4$ NPs respectively.

Due to a significant difference (~50 °C) in the decomposition temperature of the precursors (Figure 19) and in addition to SAED, XRD (Figure 37A) and EDX mapping (Figure 37B) were performed to rule out the formation of a ZnO phase prior to the formation of ferrites leading to a core-shell architecture.

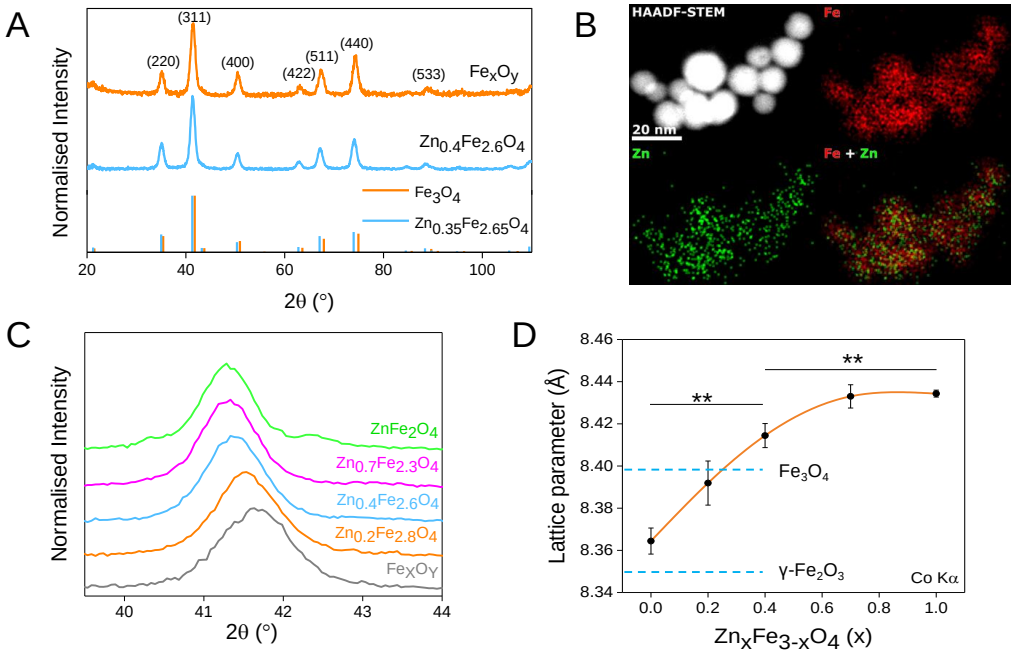

Figure 37: A) XRD patterns of iron oxide and $Zn_{0.4}Fe_{2.6}O_4$ NPs (ICDD references 01-075-0449 and 01-086-0510 respectively). B) Elemental mapping of iron and zinc by EDX. C) Magnified region around the (311) diffraction peak. D) Dependence of unit lattice parameter on the level of Zn^{2+} doping (n=3). Values reported as mean ± SEM. p-Values were calculated based on a two-tailed t-test: ** indicates $p<0.01$.

The uniform distribution of zinc and iron throughout the NP volume and in combination with SAED (Figure 36H and I) and XRD diffraction patterns (Figure 37A) show that only spinel based materials are formed. The uniform distribution of zinc and iron also excludes the formation of a $Zn_xFe_{3-x}O_4$@ZnO or Fe_xO_y@ZnO core-shell architectures. In accordance to a change of occupancy between the interstices of the lattice with cations of different ionic radius, the diffraction peaks are observed to shift in proportion to the Zn^{2+} doping level. A magnification of the most intense peak of the diffraction pattern of spinel structures (311) is shown in Figure 37C where the peak angle moves to lower values with increased doping. Bragg's law, shown in equation (8), relates the interplanar space with the angle at which a diffraction peak is observed. The interplanar space relates to the lattice parameter according to equation (9) and the effect of Zn^{2+} doping on the lattice parameter is shown in Figure 37D. The lattice parameter increases with increasing Zn^{2+} doping before reaching a plateau. In the case of γ-Fe_2O_3, the structure includes

vacancies in octahedral interstices $\left[(\mathrm{Fe}_8^{3+})_{\mathrm{Td}}\left(\mathrm{Fe}_{\frac{40}{3}}^{3+}\mathrm{V}_{\frac{8}{3}}\right)_{\mathrm{Oct}}\mathrm{O}_{32}\right]$, numbers refer to number of atoms in a unit cell, while Fe_3O_4 does not have vacancies $[(\mathrm{Fe}^{3+})_{\mathrm{Td}}(\mathrm{Fe}^{3+}\mathrm{Fe}^{2+})_{\mathrm{Oct}}\mathrm{O}_4]$ and consequently has an increased lattice parameter indicated with a blue line in Figure 37D. The introduction of Zn^{2+} displaces tetrahedral Fe^{3+} to octahedral interstices which changes the degree of inversion of the inverse spinel structure of iron oxide to a normal spinel. The ionic radius of Zn^{2+} is bigger than the ionic radius of high spin Fe^{3+} which it displaces[93]. The Fe^{3+} ion then occupies an octahedral interstice previously occupied by an Fe^{2+} ion which has a smaller ionic radius than Fe^{3+}. Hence the lattice must expand to accommodate the cation substitution and redistribution which is reflected in the lattice parameter shown in Figure 37D. Using Vegard's law, shown in equation (10), which describes the molar fraction of two solids in a mixture using the lattice parameter of materials, an estimate of the composition of the iron oxide NPs used herein was determined. The estimated content of Fe_3O_4 and γ-Fe_2O_3 is 50% each making the iron oxide NPs used herein a Fe_3O_4@γ-Fe_2O_3 composite.

In addition to TEM size measurements, the Scherrer equation shown in equation (6) can be applied on XRD data to calculate the crystallite size from the angle and broadening of a peak. Results obtained with either technique are in good agreement with each other verifying the results on a larger population of NPs as shown in Table 3. By combining the crystallite size, the peak position and broadening of the peak, a Williamson-Hall analysis shown in equation (7), can yield the lattice strain of the NPs which is related to interatomic bond changes, vacancies and defects[94]. Since the magnetic properties of these materials are tightly correlated to the interatomic coupling between cations at different interstices within the lattice structure, an increase in strain would be detrimental. As shown in Table 3, the lattice strain of the NPs does not change by the introduction of Zn^{2+} in the lattice ($n=3$, $p>0.05$).

Table 3: Lattice strain and size of Fe_3O_4@γ-Fe_2O_3 and $Zn_{0.4}Fe_{2.6}O_4$ NPs (n = 3). Values reported as mean ± SEM.

Material	d_{XRD} (nm)	d_{TEM} (nm)	Lattice strain (%)
Fe_3O_4@γ-Fe_2O_3	10.3 ± 0.7	10.1 ± 2.0	1.15 ± 0.08
$Zn_{0.4}Fe_{2.6}O_4$	9.9 ± 1.6	10.2 ± 2.5	1.1 ± 0.2

Magnetic Characterization. The magnetic properties of Fe_3O_4 come from the four unpaired electrons of the d^6 high-spin configuration of the Fe^{2+} cations only, since the d^5 high-spin Fe^{3+} are antiferromagnetically coupled by superexchange between octahedral and tetrahedral interstices[38]. The introduction of Zn^{2+} cations in the crystal with a d^{10} configuration and preferential localization in the tetrahedral interstices of the lattice due to σ-type interaction between the cation and the oxide anion, quench the antiferromagnetic coupling between the Fe^{3+} cations and enhance the magnetic properties of the material[95,96] as illustrated in Figure 38.

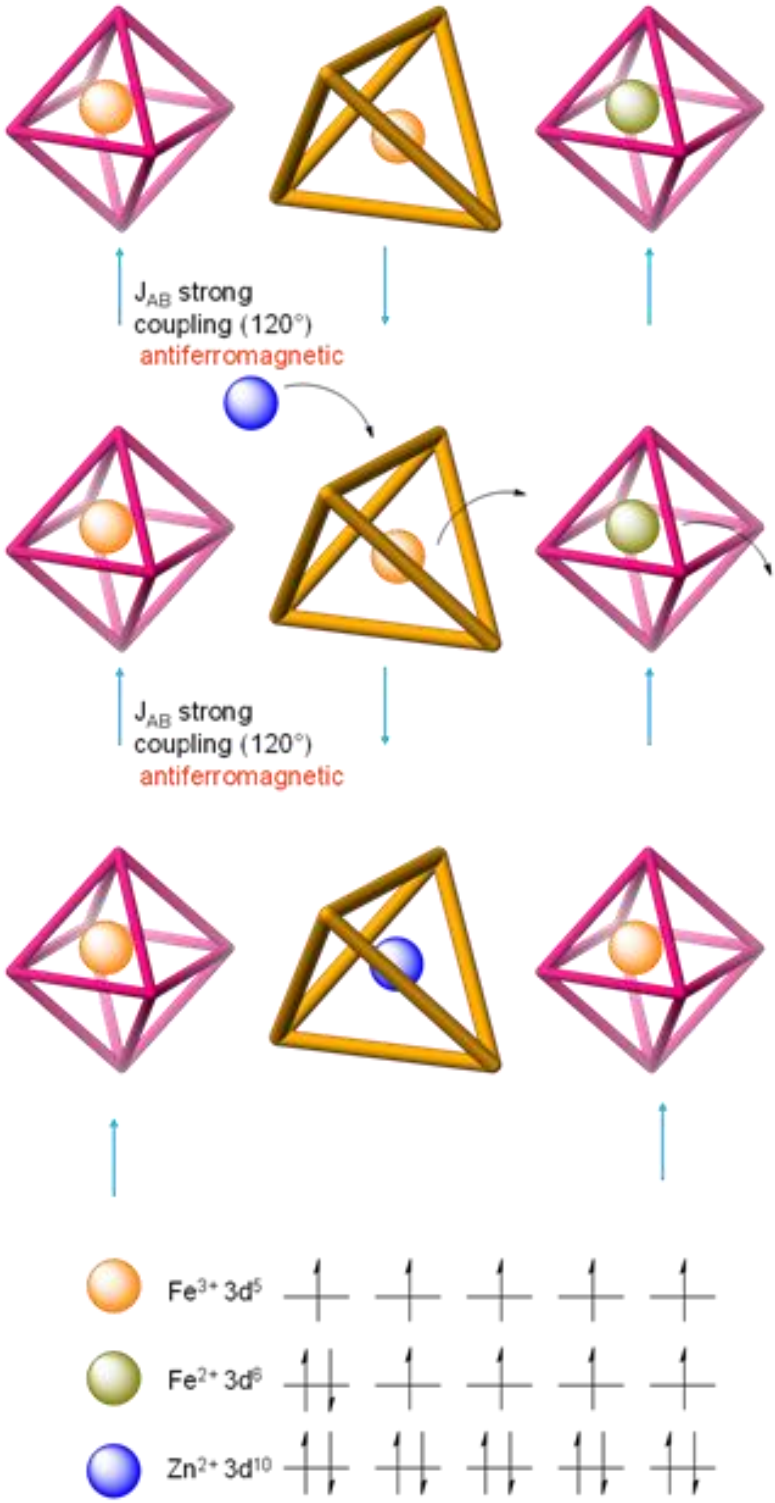

Figure 38: Illustration of antiferromagnetic coupling between octahedral and tetrahedral Fe^{3+} cations in a spinel lattice and subsequent quenching and augmentation of M_S by Zn^{2+} doping.

The synthesized NPs were characterized by means of their M_S, superparamagnetism, T_C and long-term magnetic stability as shown in Figure 39.

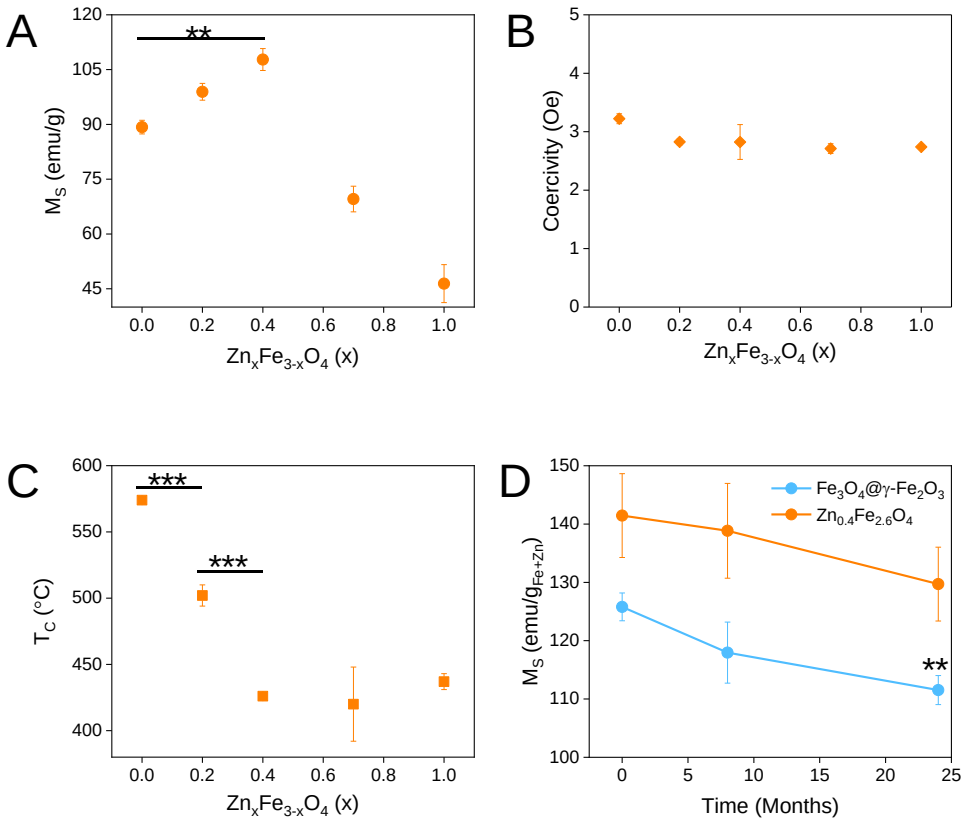

Figure 39: A) M_S (in emu per gram of material), B) Coercive field and C) T_C of synthesized ferrites with variable levels of Zn^{2+} doping (n=3). D) Long-term monitoring of the M_S of Fe_3O_4@γ-Fe_2O_3 and $Zn_{0.4}Fe_{2.6}O_4$ NPs. Values reported as mean ± SEM. p-Values were calculated based on a two-tailed t-test: * indicates $p<0.001$ and ** indicates $p<0.01$.**

The zinc ferrites exhibit complex doping-dependent M_S values with an observed increase of the M_S before diminishing with further increasing doping levels. An optimal doping level when the highest M_S values are obtained is approximately 13.5% with a molecular formula of $Zn_{0.4}Fe_{2.6}O_4$ which agrees with previous studies. Examples of zinc ferrite NPs published in literature with their corresponding size and M_S are tabulated in Table 4.

Table 4: Zinc ferrite NPs with their respective elemental composition, average size and M_S.

Composition	Average size (nm)	M_S (emu/g)	Reference
$Zn_{0.39}Fe_{2.61}O_4$	13.4	30	[173]
$Zn_{0.16}Fe_{2.84}O_4$	14	97	[174]
$Zn_{0.4}Fe_{2.6}O_4$	15	99.3[α]	[96]
$Zn_{0.34}Fe_{2.66}O_4$	17	64.6	[175]
$Zn_{0.4}Fe_{2.6}O_4$	22	105[α]	[29]
$Zn_{0.4}Fe_{2.6}O_4$	10.2	110	Shown herein

[α] value converted to emu/g of material from emu/g_{Fe+Zn}.

Among isotropic zinc ferrite NPs, the most magnetic to date was a 22 nm NP with an M_S value of 105 emu/g with a calculated volume of 5.6×10^{-24} m^3 prepared under high temperature conditions. The isotropic $Zn_{0.4}Fe_{2.6}O_4$ NPs presented herein, prepared under high temperature with autogenous pressure have a 10.2 nm size and 110 emu/g. Their size translates to ten times less magnetic volume at 0.5×10^{-24} m^3 rendering it the smallest isotropic zinc ferrite nanomaterial with the highest M_S prepared to date. Calculations on volume estimates are shown in Figure 40.

Calculation of volume of spherical nanoparticles.

$$V = \frac{4}{3}\pi r^3$$

Where V is the volume of a sphere, π is a constant (3.14) and r is the radius of the sphere.

A 22 nm spherical nanoparticle has a radius of 11 nm and 10 nm nanoparticle has a radius of 5 nm.

$$\therefore V_{22\,nm} = \frac{4}{3}\times\pi\times(11\times10^{-9}\,m)^3 = 5.6\times10^{-24}\,m^3$$

$$V_{10\,nm} = \frac{4}{3}\times\pi\times(5\times10^{-9}\,m)^3 = 0.5\times10^{-24}\,m^3$$

Figure 40: Volume calculation of spherical NPs.

Equally important is the true superparamagnetic nature of the NPs presented which makes them suitable for biomedical applications as shown from the coercivity measurements (Figure 39B) and T_B values (Table 5) obtained, unlike the next most magnetic zinc ferrite NPs with T_B values above ambient temperature.

Table 5: T_B of Fe_3O_4@γ-Fe_2O_3 and $Zn_{0.4}Fe_{2.6}O_4$ NPs (n = 3). Values reported as mean ± SEM. p-Values were calculated based on a two-tailed t-test: * indicates $p<0.05$.

Material	T_B (K)
Fe_3O_4@γ-Fe_2O_3	221 ± 23
$Zn_{0.4}Fe_{2.6}O_4$	175 ± 13
Significance	*

From T_B values the effective anisotropy (K_{eff}) can be estimated according to equation 11.

$$T_B = \frac{K_{eff} V}{k_B \ln\left(\frac{\tau_m}{\tau_0}\right)} \quad (11)$$

Where T_B is the blocking temperature (221 K for Fe_3O_4@γ-Fe_2O_3 and 175 K for $Zn_{0.4}Fe_{2.6}O_4$ NPs), K_{eff} is the effective anisotropy, V is the volume of the NPs, k_B is the Boltzmann constant (1.38×10^{-23} J/K), τ_m is the measurement time and τ_0 is the attempt time; the value $ln\left(\frac{\tau_m}{\tau_0}\right)$ has the value of 25 in typical laboratory measurements.

Given that the volume of both Fe_3O_4@γ-Fe_2O_3 and $Zn_{0.4}Fe_{2.6}O_4$ NPs, the Boltzmann constant and the natural logarithm function are constant, a reduced K_{eff} value is obtained for $Zn_{0.4}Fe_{2.6}O_4$ (1.21×10^{-5} J/m^3) compared to iron oxide NPs (1.52×10^{-5} J/m^3). As a sum of the surface and the magnetocrystalline anisotropy contributions, K_{eff} is defined as shown in equation 12 and it is shown that the magnetocrystalline anisotropy (K) of $Zn_{0.4}Fe_{2.6}O_4$ has a lower value than the K value of Fe_3O_4@γ-Fe_2O_3 NPs calculated in Figure 41.

$$K_{eff} = K + 6\frac{K_S}{d} \quad (12)$$

Where K_S is the surface anisotropy, K is the magnetocrystalline anisotropy, d is the diameter of the NPs (10.1×10^{-9} m for Fe_3O_4@γ-Fe_2O_3 and 10.2×10^{-9} m for $Zn_{0.4}Fe_{2.6}O_4$).

Calculation of K_{eff} and comparable evaluation of magnetocrystalline anisotropy of Fe_3O_4@γ-Fe_2O_3 and $Zn_{0.4}Fe_{2.6}O_4$ NPs.

$$T_B = \frac{K_{eff}V}{k_B \ln\left(\frac{\tau_m}{\tau_0}\right)} \quad \therefore \quad K_{eff} = \frac{T_B k_B \ln\left(\frac{\tau_m}{\tau_0}\right)}{V}$$

$$\therefore K_{eff_{Fe_3O_4@\gamma-Fe_2O_3}} = \frac{221\ K \times 1.38 \times 10^{-23}\ J/K \times 25}{0.5 \times 10^{-24}\ m^3} = 1.52 \times 10^{-5}\ J/m^3$$

$$\therefore K_{eff_{Zn_{0.4}Fe_{2.6}O_4}} = \frac{175\ K \times 1.38 \times 10^{-23}\ J/K \times 25}{0.5 \times 10^{-24}\ m^3} = 1.21 \times 10^{-5}\ J/m^3$$

$$K_{eff} = \mathrm{K} + 6\frac{K_S}{d}$$

$$6\frac{K_S}{d}_{Fe_3O_4@\gamma-Fe_2O_3} \equiv 6\frac{K_S}{d}_{Zn_{0.4}Fe_{2.6}O_4}$$

$$\therefore K \propto K_{eff}$$

$$Since\ K_{eff_{Fe_3O_4@\gamma-Fe_2O_3}} > K_{eff_{Zn_{0.4}Fe_{2.6}O_4}}$$

$$K_{Fe_3O_4@\gamma-Fe_2O_3} > K_{Zn_{0.4}Fe_{2.6}O_4}$$

Figure 41: Calculations of the K_{eff} of Fe_3O_4@γ-Fe_2O_3 and $Zn_{0.4}Fe_{2.6}O_4$ NPs and qualitative estimation of their K value.

This magnetic softening observed by Zn^{2+} doping could be used as a strategy to soften a borderline superparamagnetic/ferrimagnetic material and render it superparamagnetic, boosting its magnetic properties and retaining other properties of larger sized NPs. The softening of the material is also seen in the T_C values obtained where a reduction of more than 150 °C was observed for $Zn_{0.4}Fe_{2.6}O_4$ in comparison to Fe_3O_4@γ-Fe_2O_3 NPs shown in Figure 39C.

Of interest is how so small NPs could exhibit such high M_S values considering that based on the finite and very small size of NPs, ions with uncompensated spins should be a large proportion of the overall number of ions, up to 30% for

a 10 nm ferrite NP[97]. Also known as a spin-canted layer this effect becomes important at the nanoscale in contrast to the bulk form. This spin-canted layer is detrimental to the M_S of the nanomaterial and its effects are also more significant in smaller sized compared to larger sized NPs due to the surface to volume ratio changing proportionally as illustrated in Figure 42A. Over time and as Fe^{2+} oxidizes to Fe^{3+}, iron oxide-based nanomaterials might lose their magnetic properties. In the case of zinc ferrites, partial replacement of Fe^{2+} with Zn^{2+} which is redox inactive at ambient conditions extends the magnetic stability of the NPs as shown in Figure 39D for at least two years. Given that other high temperature reactions exist in literature describing the synthesis of magnetic NPs, the possible role of pressure in producing high quality NPs was investigated.

A

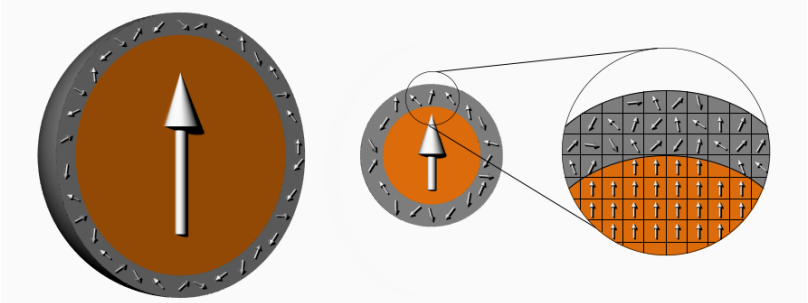

B

Pressure	Size (nm)	M_S (emu/g)	Lattice strain (%)
Autogenous	10.2 ± 2.5	108 ± 3	1.1 ± 0.2
Ambient	7.7 ± 1.7	80 ± 7	1.5 ± 0.3
Significance	***	**	*

Figure 42: A) Illustration of the proportion of spin-canting on large versus small sized NPs. B) Tabulated data of size, lattice strain and M_S measurements of $Zn_{0.4}Fe_{2.6}O_4$ NPs prepared under high temperature with ambient or autogenous pressure (n=3). Values reported as mean ± SEM. p-Values were calculated based on a two-tailed t-test: * indicates p<0.001, ** indicates p<0.01 and * indicates p<0.05.**

Effects of Pressure. In order to evaluate the role of pressure in NP synthesis and how it might relate to the preparation of high-quality nanomaterials, NPs prepared at ambient pressure (Figure 43) were used for comparison of their structural and magnetic properties.

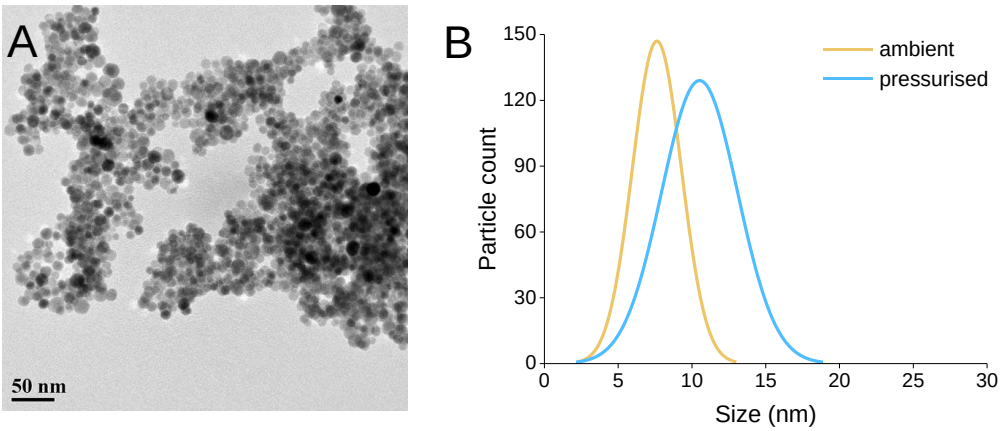

Figure 43: A) TEM of $Zn_{0.4}Fe_{2.6}O_4$ NPs prepared under ambient pressure. B) Size distribution histograms of $Zn_{0.4}Fe_{2.6}O_4$ NPs prepared at high temperature and ambient or autogenous pressure.

As it can be seen from Figure 42B, the size of the NPs prepared at ambient pressure is significantly smaller compared to NPs prepared under autogenous pressure. Interestingly, a significant increase in lattice strain is observed for NPs prepared at ambient pressure and consequently a decreased M_S value is also observed in accordance with the lattice dependent magnetic properties of the materials explained earlier. In conclusion, pressure has beneficial effects on NP synthesis producing superior materials to high temperature only synthetic protocols, in this case due to a better structured crystal.

Colloidal Stability. The NP surface was studied before and after washing procedures and a suitable functionalization protocol was developed for the successful conjugation of citrate molecules on the surface of the NPs to produce stable dispersions (Figure 33). The stability of the NPs was assessed in terms of colloidal stability over a range of pH values and electrolyte concentrations. The colloidal stability was assessed over a one-week period, over a pH range between 3-12 and electrolyte concentration range between 0-300 mM to mimic physiological pH (7.2) and tonicity (150 mM NaCl), as shown in Figure 44.

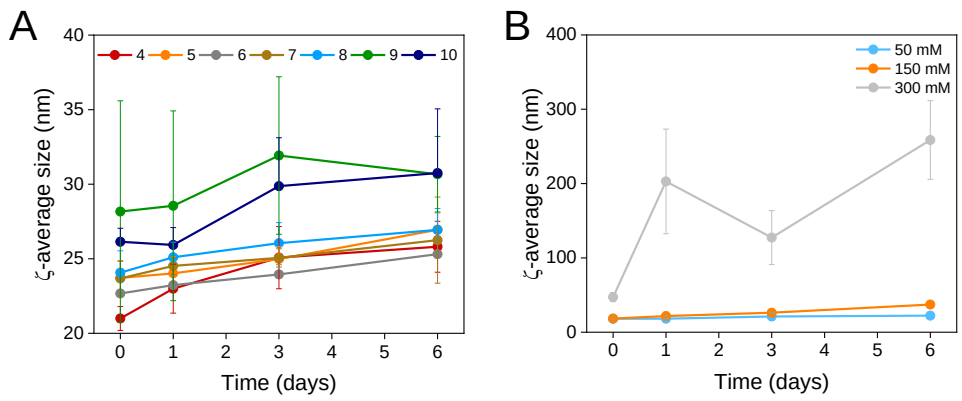

Figure 44: Colloidal stability of $Zn_{0.4}Fe_{2.6}O_4$ NPs at different A) pH values and B) electrolyte concentrations (n=3).

NPs had a short-lived colloidal stability at pH values of 11 and 12 (not shown) for 2 and 1 day respectively after which the hydrodynamic size increased sharply. At pH 3 the NPs precipitated immediately and hence no measurements could be obtained. NPs were stable between pH 4-10 for the duration of the study. The NPs exhibit good stability in electrolyte concentrations up to 150 mM. At 300 mM electrolyte concentration the NPs were unstable with sharp increases in their hydrodynamic size. The results suggest that the citrate stabilized NPs are stable in physiologically mimicking conditions (pH 7.2, 150 mM NaCl).

It is important for NPs to retain their original small size to be able to flow through blood capillaries unobstructed and successfully reach their destination. In practice, when NPs are injected in the bloodstream which has many entities such as red and white blood cells, platelets, proteins, hormones and small molecules, these can attach to the surface of the NPs.[55,98] Such action can increase the size of the NPs as well as screen their electrostatic charge leading to destabilisation. This phenomenon, known as protein corona formation, can have detrimental effects on the biodistribution of a given NP and the stability of NPs in more complex media such as cell growth media or blood should be tested.

Optical Properties. All energetic levels are quantised. Different wavelengths of the electromagnetic spectrum interact differently with molecules. Radio-waves interact with nuclear spins while infrared affects vibrational transitions,

UV-vis interacts with electronic states and microwaves with rotational motion. The energy needed to excite electrons is greater than the energy needed to excite vibrational levels. Each electronic state is split by many vibrational levels which themselves are split by rotational levels. To excite electrons by the absorption of a photon, the energy of the photon must be equal to or higher than the gap the electron is jumping from the ground state to the excited state. The minimum energy required is known as the bandgap energy (E_{gap}). The excited electron must return to its ground state and the process involves both radiative (normal arrows) and non-radiative (wavy arrows) processes. The excitation of the electron equals the energy of the absorbed photon. This excites the electron to the next electronic state while the vibrational level occupied in the excited electronic state depends on the exact energy of the photon. The transition from the excited to the ground electronic state occurs from the lower vibrational level of the excited electronic state to any of the vibrational levels of the ground state in a radiative process. It is clear then, that before the electronic transition occurs, energy is lost through vibrational energy known as thermal phonons or heat. Once in the ground electronic state, thermal energy continues to be released until the vibrational ground state is also reached. The process is illustrated in Figure 45.

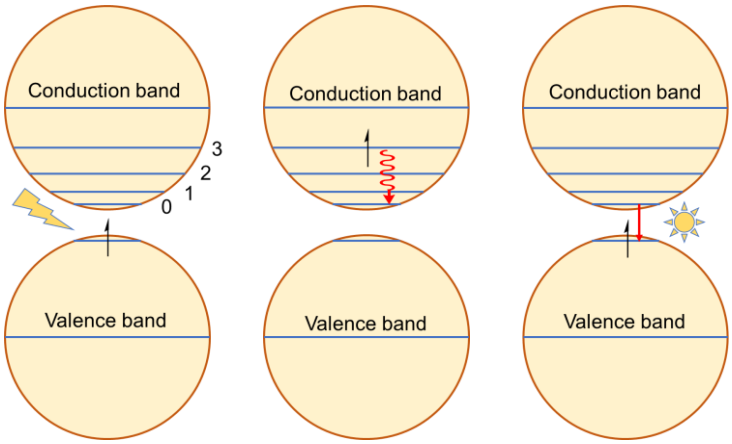

Figure 45: Illustration of the mechanism of photothermal conversion through vibrational relaxation.

Depending on the E_{gap} between the highest occupied molecular orbital (HOMO) and the lowest unoccupied molecular orbital (LUMO) materials are classified as conductors, semiconductors, or insulators. In the case of

insulators, the bandgap is so big, electrons cannot get excited from the valence band (ground state) to the conduction band (excited state). Fe_3O_4, with a band gap of 0.1 eV is a semiconductor with a very small bandgap[38]. The smaller the band gap the less energy is needed to excite an electron, and the less energy will be lost in radiative processes maximizing the light to heat conversion. This principle is currently used to modify materials for solar energy to heat conversion[99].

Fe_3O_4 and $Zn_{0.4}Fe_{2.6}O_4$ NPs have a dark colour indicating absorbance throughout the visible spectrum. This makes ferrite nanomaterials semiconductors and consequently they can find applications in semiconductor photothermia. $Zn_{0.4}Fe_{2.6}O_4$ appear darker compared to Fe_3O_4@γ-Fe_2O_3 at the same concentration as shown in Figure 46A which is indicative of a smaller bandgap. A smaller bandgap should result in augmented photothermal conversion due to less energy lost in radiative processes during electron relaxation illustrated in Figure 45.

To estimate the E_{gap} of each nanomaterial, UV-Vis-NIR spectra were recorded and converted to Tauc plots shown in Figure 46B and C respectively. The linear parts of the curves in the Tauc plots were extrapolated to y=0 to yield the E_{gap}. This method reveals a 30% reduction in the E_{gap} of $Zn_{0.4}Fe_{2.6}O_4$ with a value of 1.07 eV compared to 1.42 eV for Fe_3O_4@γ-Fe_2O_3 NPs illustrated in Figure 46D. If the mechanism of photothermal conversion is solely due to transformation of electromagnetic radiation to phonons (crystal vibrations) then $Zn_{0.4}Fe_{2.6}O_4$ NPs should perform better in photothermia.

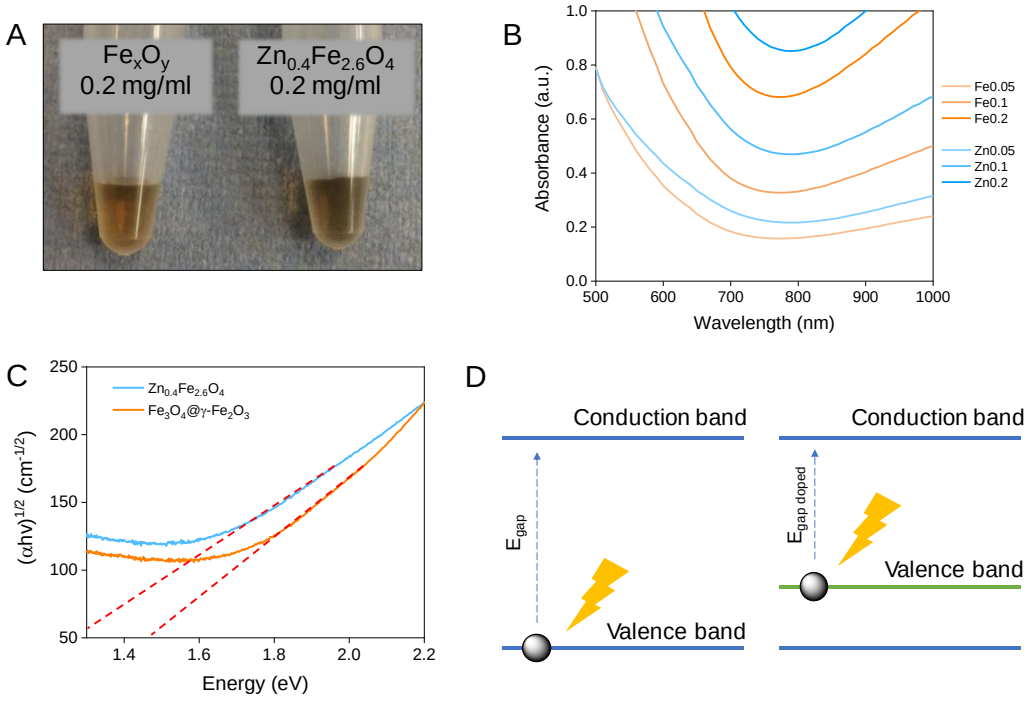

Figure 46: A) Digital photographs of Fe_3O_4@γ-Fe_2O_3 (left) and $Zn_{0.4}Fe_{2.6}O_4$ (right) NPs at a concentration of 0.2 mg_{Fe+Zn}/ml. B) UV-Vis-NIR spectra of Fe_3O_4@γ-Fe_2O_3 and $Zn_{0.4}Fe_{2.6}O_4$ NPs for concentrations between 0.05–0.2 mg_{Fe+Zn}/ml. C) Tauc plots of Fe_3O_4@γ-Fe_2O_3 and $Zn_{0.4}Fe_{2.6}O_4$ NPs with extrapolation of the linear region to y=0. D) Schematic of bandgap energy reduction by Zn^{2+} doping.

3.3.3 Reduction of Polydispersity Index by Digestive Ripening

For the commercialization and effective characterization of NPs, they should have reproducible properties. To this end, great efforts have been put into preparing monodisperse NPs with a large number of publications exploring the use of different solvents[28,100], surfactants[28,100], precursors[101] and other synthetic parameters. Even though some methods succeed in preparing monodispersed NPs, these are often irreproducible and/or require specialized techniques and equipment.

Liquid routes to the preparation of NPs involve the chemical transformation of molecular complexes or salts to supramolecular clusters/solid networks called nuclei, which are the templates where further deposition of material will occur upon[62,102]. These two steps consist of the classical nucleation and growth of the crystals, also referred to as the LaMer model. The process is divided into three distinct steps where the concentration of monomers is increasing in

solution. At a supersaturated state a burst nucleation occurs which brings the concentration of monomers down virtually prohibiting further nucleation and the rest of the monomer diffuses on existing nuclei. Detailed explanations[103] and mathematic derivations[102] of these processes have been described elsewhere.

Nucleation is a thermodynamically governed process and is accounted for by the sum of the surface free energy and the bulk free energy. Since the surface free energy is always positive and the bulk free energy always negative, there must be a critical size above which the clusters are sustainable and avoid redissolution. Supersaturation seems to have a drastic effect on nucleation and the present of surfactants can alter the surface free energy. Generally, this process is extremely fast and specialised instruments are needed to study.

The growth of nanocrystals is dependent on two processes, the diffusion of reactant to the surface of the crystal and the reaction on the surface for subsequent deposition. Growth can be a slow process and it has been studied extensively[103,104]. There are several different growth processes that can take place depending on the reaction conditions. If nanocrystal growth was solely controlled by diffusion there should not be a size spread, while experimental results sometimes show considerable polydispersity. Ostwald ripening is a thermodynamic process that explains the fact that big particles tend to grow bigger on the expense of re-dissolution of smaller particles. Coalescence and oriented attachment are also mechanisms where particles merge to form a single bigger particle. Lastly, intraparticle growth describes the transfer of monomer along the surface of the crystal for the formation of less energetic crystallographic planes. The presence of surfactants also plays a crucial and complex role. There are certain planes of materials that have higher affinity towards specific functional groups, and this differs from material to material. Some surfactants can prevent monomer from depositing on the seeds while some others cause their aggregation, sometimes so ordered that form ordered aggregates[61]. There are multiparametric complex reactions and interactions occurring at the atomic scale during the formation of NPs that is often difficult to understand or manipulate. To this end, a post-synthetic procedure was developed towards the reduction of size spread.

Digestive ripening (DR) as a post-synthetic procedure, had until recently only been applied to gold NPs to transform a polydisperse sample to monodisperse[105–107]. Due to its remarkable ability to produce size controlled, monodisperse NPs from an initially polydisperse sample, DR is now in the process of being extended to other NP systems such as CdSe and FeS_2 but to this date it has never been applied to ferrite-based materials[108,109]. In the process, NPs are suspended in an excess of surfactant which changes the energetics of the dissolution of monomers to and from the NP surface such that there is a thermodynamically stable size which the NPs tend towards to[105,110]. This equilibrium state is the key element of DR that allows such monodisperse NPs to be produced. The procedure in this work is based off that used by Yoder *et al.* on FeS_2 as this was deemed the closest system for which DR had been successfully applied[109]. The process is largely determined by the interaction between the ligand and the NP surface and it was believed this could be replicated for the ferrite system through exploiting surfactant-NP interactions. Synthetic variables, such as heating rate, solvent, temperature and the presence of monofunctional and multifunctional surfactants, have been studied leading to DR conditions reducing the polydispersity index (PDI) by 17% down to 9.4%.

The $Zn_{0.4}Fe_{2.6}O_4$ NPs presented herein have a large PDI value of 25%. Chemical and physical parameters were explored to reduce the PDI.

The reaction involves the thermolysis of acetylacetonate precursors which release acetone, CO_2 and H_2O as by-products. These gases pressurize the vessel hence the amount of precursor causally relates to the pressure developed within the vessel. The empty space above the reaction mixture is filled with these gases and consequently the more TREG present the less available ‘empty’ space and the higher the pressure. The resulting size and PDI of the NPs produced as the volume of solvent was varied between 5-20 ml are shown in Figure 47A. Within this range, there is a statistically significant increase in PDI from 21.1% to 24.6%. This indicates that pressure has a strong influence on PDI while size seems to be unaffected. Since the molarity of precursors was constant, it was speculated that an increase in TREG, which is hygroscopic, and the increase of $Zn(acac)_2.xH_2O$ which comes as the

hydrate could be a source of water in the reaction which has been shown to be detrimental to PDI[111]. Higher pressures could change the equilibrium vapour pressure of water from the reaction solution which could explain the worsening of PDI as the pressure is increased. The observed decrease at volumes above 20 ml is attributed to pressure release of the vessel as calculated based on the ideal and modified gas laws. This was also supported from liquid leaks.

The number of moles of precursor was then varied between 1-8 mmol whilst keeping the volume of TREG at 20 ml for which the resulting size and PDI of the NPs can be seen in Figure 47B.

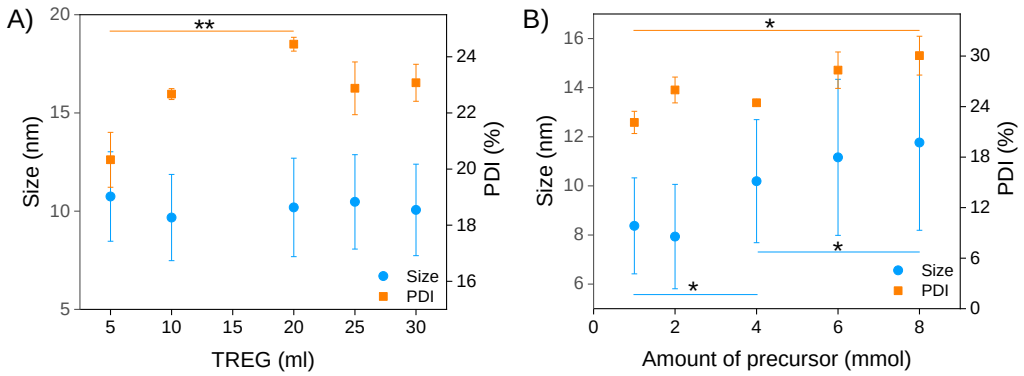

Figure 47: A) and B) Changes in size and PDI by varying the amount of TREG and precursors respectively in the high temperature reaction with autogenous pressure. Values reported as mean ± SD. p-Values were calculated based on a two-tailed t-test: ** indicates $p<0.01$ and * $p<0.05$.

It is already documented in literature that increasing the concentration of precursors for iron oxide NPs produces larger sizes with higher PDI values[112, 113]. Given that higher precursor concentration will produce more gasses resulting in a larger pressure, which has already been found to increase the PDI, one would expect the two effects to be additive. Indeed, as the moles of precursors was increased from 1-8 mmol the PDI increased significantly from 22.1% to 30.1%. This increase of 8% is over twice as large as that obtained from the pressure alone and was statistically significant. Overall, through increasing the number of moles of precursors, the NPs size changed from 8.4 ± 1.3 nm to 11.7 ± 2.3 nm. This increase is explained by a greater availability

of monomers after nucleation for NP growth[114]. This will lead to an extended growth period, which as the monomer concentration decreases will enter an Ostwald ripening regime explaining the increased PDI.

The interaction of various ligands with the NPs was investigated by introducing them in the reaction mixture. This included ligands with some bulk, such as alkyl chains or polymers with functional groups known to have high affinity for the ferrite surface such as phosphonates, carboxylates, amines, and 1,2-diols. Due to the hydrophilic nature of TREG, there was a limiting number of carbon atoms in an alkyl chain that could be solubilized in it. Decanoic acid, decylphosphonic acid, decylamine and 1,2-decanediol were used for the small alkyl chain to provide steric effects and functional groups to interact with the NPs surface. The effect of the amount of each surfactant was investigated as shown in Figure 48.

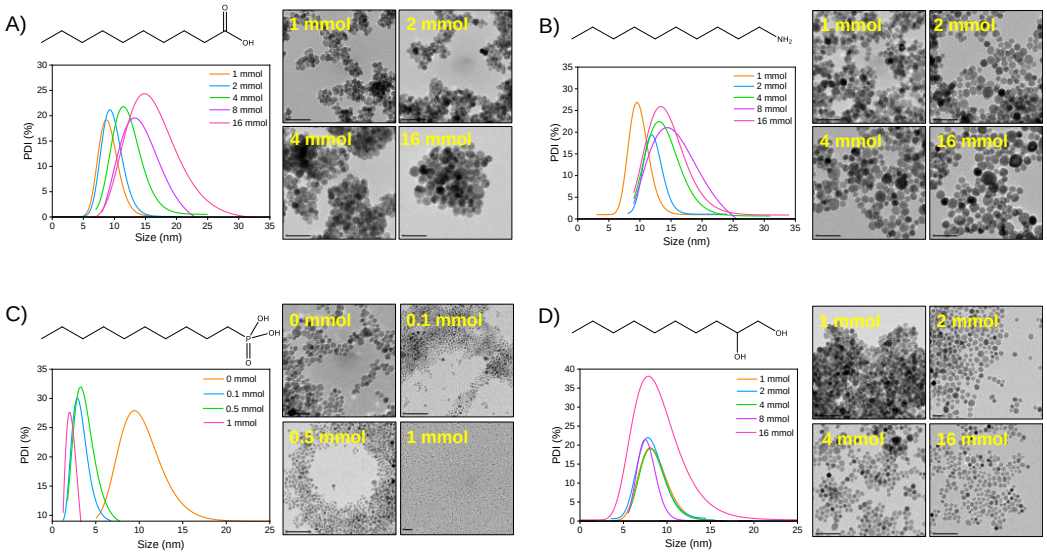

Figure 48: $Zn_{0.4}Fe_{2.6}O_4$ NPs synthesized under high temperature with autogenous pressure in the presence of A) decanoic acid, B) decylamine, C) decylphosphonic acid and D) 1,2-decanediol.

For decanoic acid and decylamine, an increasing trend in size was observed proportionally to the amount of surfactant added. At the highest tested amounts, 16 mmol of decanoic acid produced NPs with size 16.6 ± 4.0 nm (PDI: 24.3%) and for 16 mmol decylamine, 15.5 ± 4.0 nm (PDI: 25.8%), both statistically significant in comparison to the reference procedure (no ligand present). This would characterise both as ripening agents. They are increasing

the NP size through forming stable complexes with the monomers and reducing nucleation rates. These ripening agents also lead to significant decreases in the PDI at lower concentrations. At 1 mmol of decanoic acid the PDI was reduced to 19.1% from 24.5% and for 2 mmol of decylamine it was reduced to 19.4% also both statistically significant. It is possible that this reduction in the PDI comes from the stable complexes these surfactants form with the monomers. When the nucleation window has passed these complexes can feed the growth of the NPs[115] essentially putting them into the size focusing regime discussed by Sugitmo[116]. If too much ripening agent is added, then nucleation will be greatly inhibited, more complexes will be available for growth leading to larger particles and PDI values. Decylphosphonic acid on the other hand inhibited the NP growth, so much that when used in excess of 1 mmol no NPs could be observed under the TEM shown in Figure 48C. This difference in behaviour from that of decanoic acid and decylamine is a result of the strong tridentate bonding of the phosphonic acid group to the NP surface[117]. Given this inhibition of growth, the amount of decylphosphonic acid was decreased below 1 mmol in order to determine its effect on PDI. However, at 0.1 mmol the NPs produced were sized 3.2 ± 0.9 nm with a large increase in PDI of 27.7% with statistical significance of >99.9% compared to the reference reaction without surfactant. The influence of the decylphosphonic acid on growth mirrored that of a nucleating agent. By binding strongly to the surface of the NPs it was arresting growth, entirely at higher concentrations, producing much smaller NPs at lower concentrations. When compared to the synthesis without surfactants, 1,2-decanediol gave a slight reduction in the size of the NPs produced. This is in agreement with literature which shows diols forming strong bidentate bonds with iron oxide NPs[118]. The 1,2-decanediol is acting as a nucleating agent, like decylphosphonic acid, but with weaker binding to the NPs surface and so less inhibition of growth. At 4 mmol the NPs size is 8.6 ± 1.6 nm with a PDI of 19.0% which is statistically significant compared to the absence of a surfactant to >99.9%. Nucleating agents are known to hinder Ostwald ripening[119], which is likely the mechanism responsible for this improvement. Clearly, the functional group of the surfactant has a strong effect on how it interacts during the synthesis of NPs and can be used to alter both their size and PDI. Both the

ripening agents decanoic acid and decylamine along with the nucleating agent 1,2-decanediol were able to reduce the PDI significantly from 24.8% to 19%. The mechanisms by which these two types of surfactants are proposed to reduce the PDI are different and have been shown to give further improvements in combination[120].

Even though clear effects are obtained from singly functionalized surfactants, the values obtained are far from the 10% hallmark for good quality NPs. To this end, the potential of polymers was investigated. Histograms of the NPs synthesized using polyvinyl alcohol (PVA) and polyacrylic acid (PAA) can be seen in Figure 49A and B to be compared to 1,2-decanediol and decanoic acid respectively baring similar functional groups. In contrast to the reduction in NP size with increasing amount of surfactant observed with 1,2-decanediol, increasing the amount of PVA increases the size of the NPs produced from 9.7 ± 2.2 nm at 1 mmol to 15.9 ± 3.8 nm at 16 mmol with >99.9% statistical significance. This shift from a nucleating agent to the behaviour of a ripening agent could be explained by the greater separation between hydroxyl groups on the polymer backbone. This shifts the behaviour from the strong bidentate bonding of 1,2-decanediol to weaker monodentate bonding between PVA and the NP surface. The PDI is only marginally improved over that with no surfactant with a reduction of just 2.3%. Despite having the same functional group, PAA displays contrasting behaviour to decanoic acid. Increasing the amount of PAA from 1–8 mmol reduces the size of the NPs from 11.0 ± 3.5 nm to 8.6 ± 2.4 nm with >99.9% statistical significance. This shift from ripening agent for decanoic acid to nucleating agent for PAA, could imply that the binding strength to the surface of the NP has increased. Further, the much longer chain of the PAA (M_W=400,000 g/mol) would be decreasing monomer diffusion and sterically hinder the formation of the NPs. The last polymer tested, polyvinylpyrrolidone (PVP), interacts differently with the NPs compared to PVA and PAA. At 4 mmol the PDI is reduced to 18.0% which is statistically significant to >99% compared to the synthesis in the presence of no surfactant. Due to a stiffer polymer backbone due to the cyclic five-membered ring, it is speculated that less tangling and wrapping occurs in comparison to PVA which would improve the coordination of the polymer to the NP surface resulting in

an improved PDI. This is reflected in the size of the NPs which remains within 1 nm of that with no surfactant using 1–8 mmol of PVP indicating that the polymer chains cannot be significantly inhibiting growth at these concentrations. However, from 8 mmol to 16 mmol there is an increase in size and PDI from 10.7 ± 2.2 nm (PDI: 20.8%) to 15.0 ± 3.5 nm (PDI: 23.5%) which is statistically significant to >99%. These results appear to show that the increase in chain length from PVA and PAA increasingly restrict the growth of NPs. This is deduced from the opposite behaviour observed from that expected if the functional group were the dominant factor in determining growth with polymers as surfactants. In general, as a result of a lack of uniformity to this inhibition of growth, the PDI of the NPs synthesized using polymers only offered a marginal improvement over that with no surfactant. The exception to this behaviour was PVP which produced NPs sized 10.1 ± 1.8 nm with a PDI of 18%. This was attributed to the stiffer chains of the PVP reducing entanglement. From the results obtained from changing the reaction

parameters and addition of surfactant, none has achieved lowering the PDI below 10%.

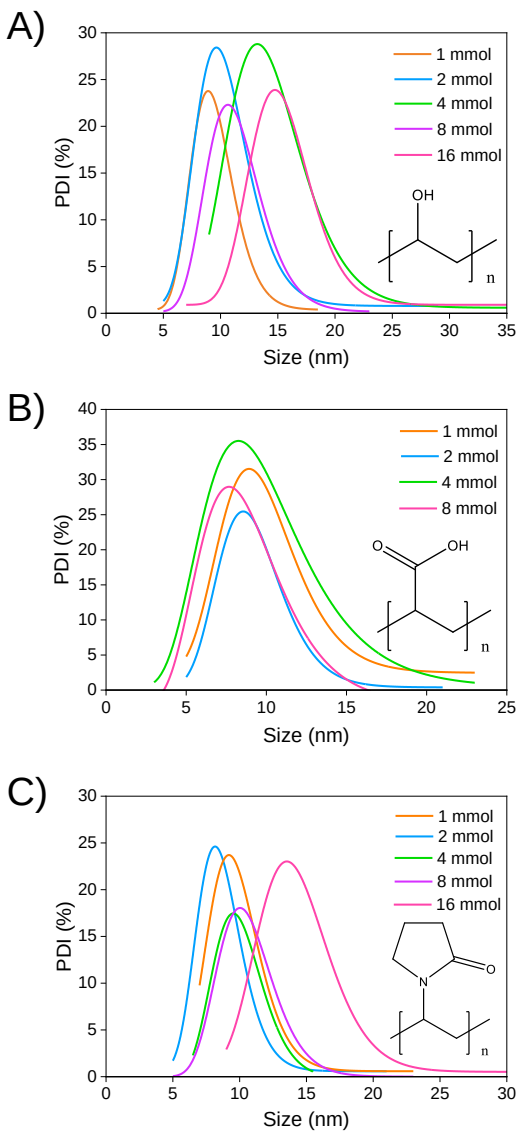

Figure 49: Size distributions of $Zn_{0.4}Fe_{2.6}O_4$ NPs prepared in the presence of (A) PVA, (B) PAA and (C) PVP at various proportions.

Due to the complexity of monitoring in detail reactions under pressure enclosed in an oven, the NPs prepared in the absence of any additives were used in a post-synthetic step for optimization. Based on synthetic conditions from other materials, 0.15 mmol of NPs were refluxed at 155 °C in 50 ml dimethylformamide (DMF) with dodecylamine (DDA). As a large excess of ligand is required in order for DR to occur[105], the ratio of the number of moles

of NPs to surfactant was varied from 1 : 32 to 1 : 256, for which the resulting size and PDI of the NPs are shown in Figure 50A and B.

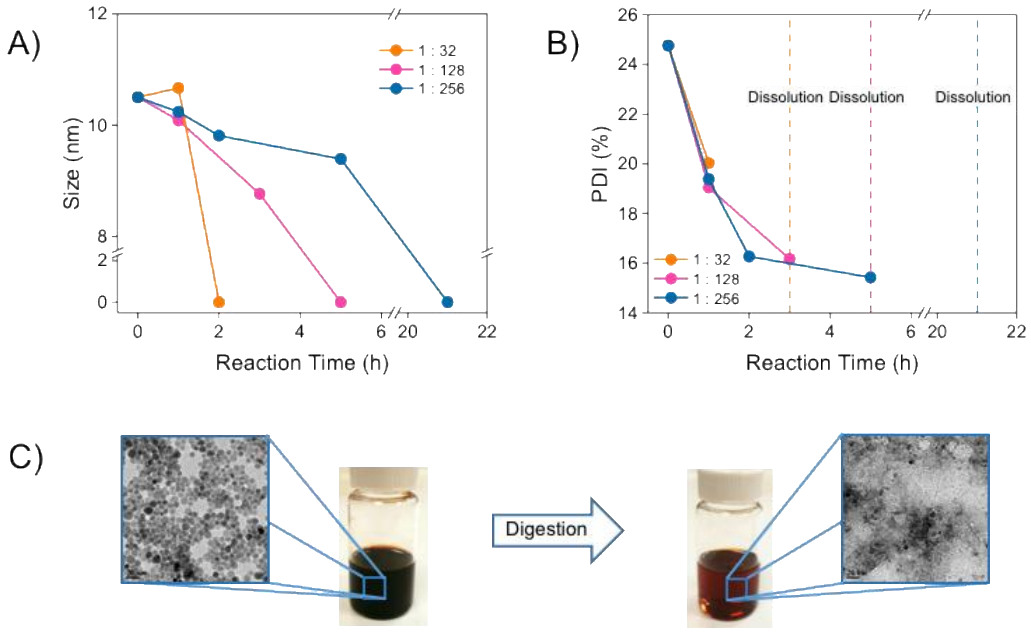

Figure 50: Change in A) size and B) PDI of NPs during DR with varying ratios of NPs to surfactant. C) Digital and TEM images of the NPs before DR and after complete dissolution.

The initial size of NPs was 10.5 ± 2.6 nm with a PDI of 24.7%. A significant improvement on this was observed in all cases with the best result obtained with more surfactant (1 : 256) after 5 h, resulting in NPs of 9.4 ± 1.4 nm with a PDI of 15.4%. For all three reactions the NPs slowly decreased in size and eventually completely dissolved, Figure 50C. This dissolution was faster the lower the concentration of ligand used which can be seen in Figure 50A. Control experiments in the absence of any ligands left the NPs unchanged even after 21 h of heating. A change in colour from black to brown is attributed to oxidation from prolonged heating and the high polarity of DMF. These results are in aggreement with literature ascribing the DR action solely to surfactants[106].

However, even though significant improvements in PDI were attained, the NPs were eventually dissolving even with remarkably high excess of ligand indicating that these reaction conditions were not producing a thermodynamically stable size. Lowering the temperature has previously

shown to prevent dissolution[110], hence the temperature was lowered to 110 °C. Due to the minimally better results of the 1 : 256 ratio compared to 1 : 128, the experiments at lower temperatures were performed with NPs : DDA ratio of 1 : 128.

It can be seen in Figure 51A that when the temperature of the reaction was reduced to 110 °C, the dissolution of NPs in DMF was slower, finishing at 21 h instead of 5 h for the experiment using the same concentration at 155 °C shown in Figure 50A and B. However, the NPs were still dissolving, and it was proposed that the polar nature of DMF (Figure 51C) could be the cause of this by coordinating the ligand monomer complexes and preventing redisposition on NPs. Consequently, the less polar non-coordinating solvents toluene and mesitylene were used and the size and PDI of the NPs produced in all three solvents can be compared in Figure 51A and B. Toluene was shown not to prevent dissolution of the NPs although largely delaying it to very long reaction times and gave NPs with low PDI of 14.2% at 84 h. This marks a significant reduction from the initial PDI value of 24.7% with only a small but significant decrease in size to 9.3 ± 1.3 nm. In contrast, the change in NP size at 60 h for mesitylene was not statistically significant from the initial size of the NPs (p=0.1) which is desirable for the equilibrium conditions sought after here.

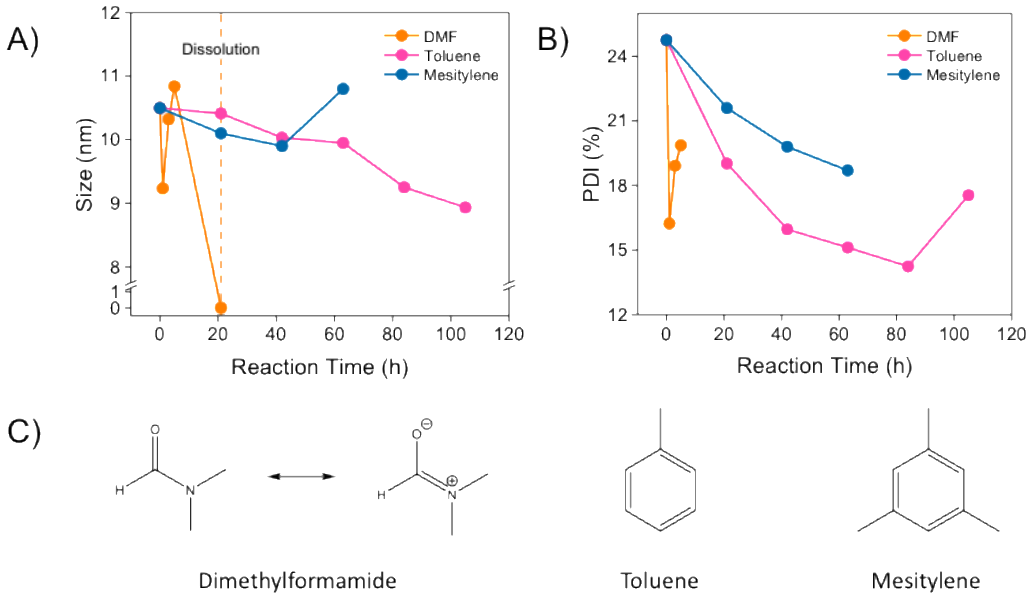

Figure 51: Change in A) size and B) PDI of the NPs during DR with different solvents. C) The molecular structures of the solvents used.

From the conclusions as to the nature of amine-based ligands, that of being ripening agents, it would seem likely that the DDA being used here is a ripening agent too. Ripening agents form soluble complexes with monomers which could have been the cause of the difficulty in preventing the NPs from dissolving during the DR process.

Changing the surfactant to a nucleating agent, which forms insoluble precipitates may prevent dissolution and improve the DR procedure. DPA was earlier found to behave as a very strong nucleating agent (Figure 48C) and so it was used in place of DDA. Due to the very strong effects observed with DPA at very low amounts, the molar ratio of NPs to surfactant changed to 1 : 30, matching that used by Prasad *et al*. for gold NPs also using a nucleating agent[106]. Within our experimental scope, mesitylene was the only solvent that did not show signs of dissolution within the experimental time-frame as seen in Figure 51. Using the nucleating agent DPA a size equilibrium is achieved successfully producing monodisperse NPs without a reduction in size. After 21 h the NPs were sized 13.8 ± 1.3 nm corresponding to a PDI of only 9.4%. This is below 10% which is widely accepted as a hallmark for high quality NPs. This marks a considerable improvement over the initial NPs, sized 10.5 ± 2.6 nm, which had a PDI of 24.7%. These results for DPA after 21 h can be seen in Figure 52 compared alongside the lowest PDI attained using DDA as the surfactant taking 83 h.

A)

Surfactant	Reaction time (h)	Size (nm)	PDI (%
No surfactant	N/A	10.5 ± 2.6	24.7
DDA	84	9.3 ± 1.3	14.2
DPA	21	13.8 ± 1.3	9.4

B)

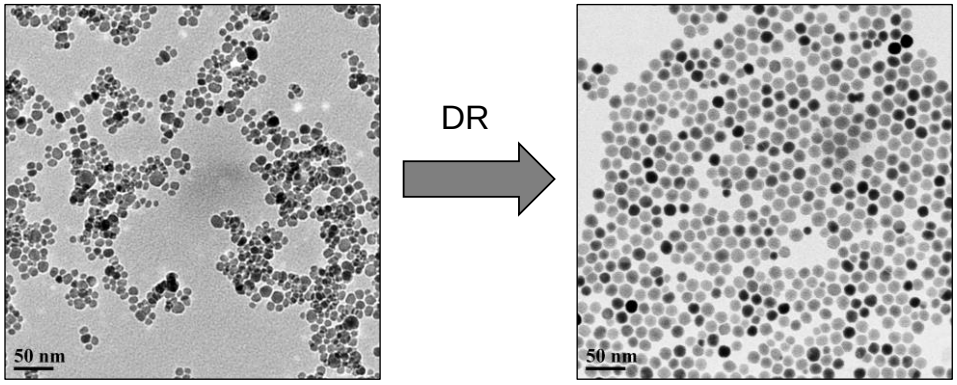

Figure 52: A) Tabulated data of the lowest achievable PDI values using DDA and DPA along with their sizes compared to the reference reaction. B) TEM images of $Zn_{0.4}Fe_{2.6}O_4$ NPs before and after DR with DPA.

3.4 Conclusion

A series of Zn^{2+} substituted ferrites were prepared and characterized using a high temperature with autogenous pressure synthesis. A Zn^{2+} level dependent augmentation of the M_S is observed with the highest value observed for the material with the composition $Zn_{0.4}Fe_{2.6}O_4$. The developed synthetic procedure produces material with less lattice strain compared to high temperature-only reactions leading to the most magnetic $Zn_{0.4}Fe_{2.6}O_4$ isotropic NPs with the smallest volume reported to date. The NPs dispersions prepared exhibit good colloidal stability in physiologically mimicking conditions and magnetic stability for at least two years. The $Zn_{0.4}Fe_{2.6}O_4$ NPs exhibit a decreased E_{gap} which could be exploited as a photothermal agent for cancer hyperthermia. Through a post-synthetic procedure, the PDI of the NPs was reduced to 9.4% from 24.7%.

4 Nanotoxicological Studies of Best-in-Class $Zn_{0.4}Fe_{2.6}O_4$ Nanoparticles and Their Applicability as an Agent for Cancer Hyperthermia

4.1 Introduction

Many materials show potential for several biomedical applications with great potential in treating disease, sometimes showing manifold increased performance compared to current standards. Within the scope of hyperthermia treatment there are two classes of materials that are used in biomedical nanotechnology; magnetic NPs that convert magnetic work to heat and noble metal NPs which transform light into heat[5-8]. Each modality has its own advantages and disadvantages such as effective heating, penetration to deep tissue and availability and cost of applicators. Metallic NPs such as gold, have been previously utilised for photothermal conversion through the localised plasmon resonance they exhibit[7,8]. Gold NPs absorb only a specific wavelength of light. Gold spheres normally absorb UV light not normally penetrating the skin while the gold nanorods that can be made to absorb in the NIR region currently contain silver which itself is toxic[121]. Organic materials have also shown this ability due to strong light absorption, although suffering from aging instability[11]. Therefore, there is a potential to utilise the semiconducting properties of magnetic NPs towards the development of a photothermal therapy (PTT) agent which is currently underexploited.

The process of moving pharmaceutics from the laboratory to clinical testing is long and thorough to ensure their safety prior to administrating such materials to human subjects. For such purposes, cell cultures are used to screen and prove concepts of safety and efficacy of new pharmaceutics. As such, the biocompatibility of the synthesised nanomaterial was thoroughly assessed.

4.2 Materials and Methods

4.2.1 Reagents

1,10-phenanthroline monohydrate (99%), hydroxylamine hydrochloride (ReagentPlus® 99%), nuclear fast red solution (0.1% in 5% aluminium sulfate), potassium hexacyanoferrate (II) trihydrate (98.5% ACS reagent), crystal violet solution for staining, sodium cacodylate trihydrate (98%), trypan blue 0.4% solution, Poncaeu S (0.1%) solution, tert-butyl hydroperoxide (TBHP) and sucrose (99.5%) were purchased from Merck, UK. 37% HCl was purchased from Acros Organics, UK. $FeCl_2.4H_2O$ (99.0%) was purchased from Honeywell, UK. Eagle minimum essential medium (EMEM), dimethyl sulfoxide (DMSO) (BioReagent, 99.9%) and sodium acetate anhydrous (ReagentPlus® 99.0%) were purchased from Sigma Life Science, UK. Fetal bovine serum (FBS), Penicillin/Streptomycin (P/S), GlutaMAX, Trypsin-EDTA 0.05%, phosphate buffered saline (PBS) and Dubelco's minimum essential medium (DMEM) were purchased from Gibco, UK. 3-(4,5-dimethylthiazol-2-yl)-2,5-diphenyltetrazolium bromide (MTT) (98%) was purchased from Alfa Aesar, UK. Paraformaldehyde (PFA) (96.5%) was purchased from TAAB, UK. Alamar Blue was purchased from Invitrogen, UK. Ethanol (100%) was purchased from HaymanKimia Ltd. Pierce lactose dehydrogenase (LDH) cytotoxicity assay kit, radioimmunoprecipitation assay buffer (RIBA), phosphatase and protease inhibitor cocktail, DRAQ7, NuPAGE LDS sample buffer (x4), Bolt MES SDS running buffer (x20), Bolt bis-tris gradient (4-12%) gels, bicinchoninic acid assay (BCA) kit, livin monoclonal antibody, Caspase 3 monoclonal antibody, Cytochrome C monoclonal antibody, heat shock protein (HSP) 70 monoclonal antibody, surviving monoclonal antibody were purchased from Thermo Scientific, UK. Anti-x-linked inhibitor of apoptosis (XIAP) monoclonal antibody was purchased from Abcam, UK. Fluorsave antifade solution was purchased from Calbiochem, UK. Water was purified by Purelab Ultra, Elga. All chemicals have been used without further treatment.

4.2.2 Experimental Methods

4.2.2.1 Cell Maintenance

Cell Culture Medium. All cell lines were grown in MEM supplemented with 10% FBS, 1% P/S and 1% GlutaMAX, referred to as a complete medium.

Cell Thawing. Cell lines were recovered from liquid nitrogen and quickly defrosted in a water bath at 37 °C. The suspension was gently transferred to a centrifuge tube and slowly topped up with pre-warmed complete medium with constant gentle swirling of the tube. After centrifugation (1500 g, 3 min) the cell pellet was resuspended in fresh complete medium and seeded in a culture flask. The flask was kept in a humidified incubator at 37 °C and 5% CO_2.

Cell Keeping. Tissue culture flasks were maintained in a humidified incubator at 37 °C and 5% CO_2. The growth medium was changed every other day with pre-warmed complete medium. Near confluency, cells were split to keep them in a logarithmic growth phase. To split the cells, the medium was removed, the cells were washed twice with PBS and detached with trypsin (0.05%). The enzyme was quenched with complete medium and cells isolated by centrifugation (1500 g, 3 min). After counting using a haemocytometer, the necessary number of cells was seeded in a new tissue culture flask and propagated in a humidified incubator at 37 °C and 5% CO_2.

Cell Storing. Excess cells were resuspended in complete medium supplemented with 1% DMSO. Acting quickly, the cells were added in freezing vials at a concentration of 1.5 million cells per vial and cooled down to -80 °C at a rate of 1 °C/min. The next day, the vials were placed in the liquid nitrogen cell bank.

4.2.2.2 Cellular Uptake of Nanoparticles

Quantification. The uptake of NPs was quantified by single cell magnetophoresis. U87-MG and MCF-7 cells were grown to near-confluency in T25 flasks. The medium was removed and NPs at a concentration of 0.2 mg_{Fe+Zn}/ml in complete EMEM medium were added in each flask and incubated between 1-24 h. After, the cells were washed with EMEM (2×3 ml) and PBS (2×3 ml). The cells were detached with trypsin and collected by centrifugation (1500 rpm, 3 min). 1 ml of complete EMEM was used to resuspend the cells to singe cell suspension by pipetting and transferred in a 1 mm thick Hellma chamber and subjected to a magnetic field (B=321 mT, gradB=4.7 T/m, Figure 53) generated by a neodymium permanent bar magnet.

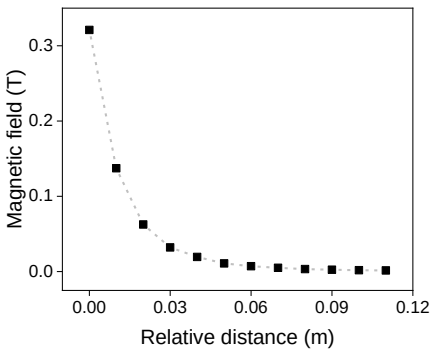

Relative Distance (m)	Magnetic Field (T)	Field Gradient (dB/dx)
0	0.321	
0.01	0.1373	-18.37
0.02	0.0626	-7.47
0.03	0.0321	-3.05
0.04	0.01945	-1.265
0.05	0.01089	-0.856
0.06	0.00717	-0.372
0.07	0.00507	-0.21
0.08	0.00337	-0.17
0.09	0.002495	-0.0875
0.1	0.001871	-0.0624
0.11	0.001535	-0.0336

Figure 53: Magnetic field measurements over distance using a gaussmeter for the bar magnet used in single cell magnetophoresis.

The cells are attracted to the magnet by the magnetic force expressed in equation 13.

$$\mathrm{F} = \mathrm{MgradB} \tag{13}$$

Where M is the magnetic moment.

The magnetic force is countered by Stoke drag force and equilibrium is quickly reached described in equation 14.

$$\mathrm{F_{drag}} = 6\pi\eta\mathrm{rV} \tag{14}$$

Where r is the cell radius, η the dynamic viscosity of water and V the speed of the cell.

Videos of the cell movements were recorded on a Leica DMIL inverted microscope equipped with an MC170 HD camera at 4 images per second. Using the image analysis software ImageJ, the diameter and distance travelled by cells were measured. Assuming a material density of 5×10^6 g/m^3 the amount of iron in each cell could be calculated by converting the cell magnetic moment using the magnetic moment of $Zn_{0.4}Fe_{2.6}O_4$ NPs at the field strength applied by the bar magnet from SQUID-VSM measurements.

Histology and Localization Studies. U87-MG cells were grown on glass cover slips in a clear 24-well plate at a seeding density of 1×10^5 cells/well. After overnight incubation, the cells were treated with different concentrations of NPs (0-300 μg_{Fe+Zn}/ml) in complete EMEM for 24 h. After, the cells were washed with medium (2×3 ml) and PBS (2×3 ml). Fresh complete medium was added to the cells and incubated for further 2-3 h to allow the cells to relax

from handling stress. Sucrose supplemented (2%) PFA solution in PBS (100 µl, 4%) was added to each well as a prefixation step and incubated at 37 °C for 10 min. After, the cells were washed with PBS (2×3 ml) and fixed with 100 µl of sucrose-PFA solution. After 10 min incubation at 37 °C the cells were stained with a 1 : 1 mixture of 4% HCl and 4% potassium hexacyanoferrate (II) trihydrate for 3 min. The cells were washed with water (2×100 µl) and counterstained with Nuclear Fast Red solution for 5 min. Stained cells were dehydrated with ascending alcohol by immersion in 70% (2 min) and 100% (5 min) ethanol. The cover slips were mounted on microscope slides over anti-fade oil and sealed with nail polish. Images were obtained on an inverted microscope Leica DMI6000B in bright field mode.

4.2.2.3 Toxicological Assessment

Metabolic Activity. For the MTT assay, U87-MG cells were plated in 96-well plates at a density of 5000 cells/well and incubated for 24 h. The experimental groups were exposed to NPs suspensions with concentrations up to 1500 μg_{Fe+Zn}/ml in complete EMEM with no phenol red and the cells were incubated for further 24 h. Dilution of the culture medium from NPs suspension was capped at 10% to prevent viability decrease from osmotic imbalance. The NPs were removed and syringe-filtered (0.2 µm) MTT solution (10 µl, 0.2 mg/ml) was added in each well and incubated for 4 h at 37 °C. After, the MTT solution was removed and DMSO (200 µl) was added to dissolve the purple formazan crystals on a plate shaker for 30 min. 150 µl of the supernatant were transferred in another 96-well plate and the absorbance was measured at 570 nm. The assay was performed in quadruplicate and statistical analysis was performed by two-way Anova using SPSS software.

Membrane Integrity. The LDH assay requires an optimum cell number which needs to fall within the linear part of the absorbance curve which needs to be experimentally determined for different cell lines as they have different physiological LDH activity. In conjunction with the cell growth curve and LDH activity with respect to cell number (Figure 54), 3000 cells/well was the experimentally determined optimum seeding number.

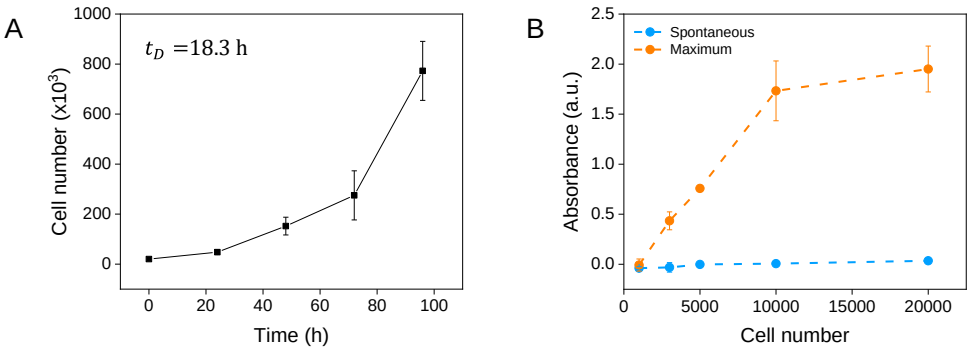

Figure 54: A) U87-MG cell growth curve. B) Spontaneous and maximum LDH activity controls with respect to cell number for optimum cell seeding number. n = 3. Values reported as mean ± SEM.

Cells were seeded in 96-well plates and incubated overnight. NPs were added to final concentrations between 0-1000 μg_{Fe+Zn}/ml. Complete EMEM, EMEM, spontaneous (ultrapure water) and maximum (10X lysis buffer) LDH activity (SA and MA respectively) served as controls. 24 h after, 50 µl of all samples were transferred into a clean 96-well plate and mixed with reaction mixture (50 µl). Wells treated with NPs rest on a bar magnet for 5 min to prevent transferring any NPs to the clean plate. The plate was left at RT for 30 min protected from light. Stop solution (50 µl) was added in all wells and the absorbance was measured at 490 nm and 680 nm. The absorbance values at 680 nm were subtracted from the 490 nm values before calculating cytotoxicity as shown in equation 15.

$$\%\ \text{Cytotoxicity} = \frac{\text{NPs activity} - \text{SA}}{\text{MA} - \text{SA}} \times 100 \qquad (15)$$

Proliferation. The clonogenic assay was performed by seeding 100 NP-treated U87-MG cells (0.2 mg_{Fe+Zn}/ml, 24 h) as single cell suspension per well of a 6-well plate. Untreated cells were used as controls. The cells were incubated at 37 °C, 5% CO_2. When large enough colonies were formed (50 cells or more to score), the medium was removed, cells were washed with PBS and fixed with 6% glutaraldehyde for 10 min. Colonies were stained with

crystal violet solution for 30 min and washed by immersion in water until clear, let air-dry and counted under a microscope.

4.2.2.4 Hyperthermia Measurements

In Suspension. Temperature was measured using an infrared thermal imaging camera (FLIR SC7000) in real time every second and processed with the software Altair. MFH was performed on a commercially available instrument from Nanoscale Biomagnetics, Spain. Field and frequencies for the AMF were electronically controlled using the software Magno. PTT was performed using lasers from Laser Components SAS, France, calibrated to irradiate samples with 0.3 W/cm^2 and 1 W/cm^2. Small volumes of samples (50-100 µl) were placed in Eppendorf tubes and treated with either method. The heating power was measured by the temperature plateau and specific absorption rate (SAR). The temperature plateau was directly measured by the infrared camera while the SAR value was calculated according to equation 16.

$$\mathrm{SAR} = \frac{\mathrm{m_{sample}} c}{\mathrm{m_{Fe+Zn}}} \frac{\mathrm{dT}}{\mathrm{dt}} \tag{16}$$

Where m_{sample} is the total mass of the sample (g), c is the specific heat capacity approximated to that of water (4.185 J/g/K), m_{Fe+Zn} is the total mass of iron and zinc in the sample (g) and dT/dt is the initial slope of the heating curve over the first 30 s.

In Cellular Confinement. The impact of cellular confinement was assessed in cacodylate fixed U87-MG cells. Briefly, cells were grown to near confluency, treated with 0.2 mg_{Fe+Zn}/ml $Zn_{0.4}Fe_{2.6}O_4$ NPs for 24 h, washed with PBS and trypsinised. Fixation was done with 0.2 M sodium cacodylate : 25% glutaraldehyde : water mixture with a ratio of 5 : 2 : 3. The cell pellet was resuspended in PBS and treated.

For live-cell experiments, cells were treated with NPs, washed with PBS and trypsinised. The cell pellet was treated with MFH or PTT (pre-equilibrated at 37 °C), resuspended in complete DMEM and plated in a 96-well plate. After 24 h, cells were washed with DMEM with no phenol red and incubated with DMEM with no phenol red supplemented with 10% Alamar Blue for 1 h. Then, 50 µl from each well were transferred to a clean plate and fluorescence was measured on a multimode plate reader Enspire, Perkin Elmer, at an excitation wavelength of 570 nm and fluorescence detection at 585 nm.

4.2.2.5 Protein Expression

Cell Lysis. A near confluent T75 tissue culture flask of U87-MG cells was treated with $Zn_{0.4}Fe_{2.6}O_4$ NPs at a final concentration of 10 μg_{Fe+Zn}/ml in complete medium. After 24 h, the cells were washed with PBS and trypsinised. The cells (approximately 7 million cells) were plated in three 60 mm Petri dishes and allowed to adhere for 4 h in the incubator at 37 °C and 5% CO_2. All Petri dishes were removed from the incubator and 2 of them treated with an 808 nm laser at 0.3 W/cm^2 for 0.5 min and 1 min respectively. They were then returned to the incubator for 2 h after which they were washed with ice-cold PBS and lysed. The lysis buffer was RIBA complemented with phosphatase and protease inhibitors (x2). The buffer (400 µl) was added in each petri dish, sat in ice and put on a shaker for 30 min. The resulting suspension was centrifuged (12000 rpm, 20 min, 3 °C) and the supernatant was collected and frozen until needed.

Bicinchoninic Acid Assay. Albumin standard was serially diluted to prepare concentrations from 0-2000 µg/ml. The working reagent was prepared by mixing 50 : 1 Reagent A : Reagent B provided in the kit, to produce a clear green solution. 25 µl of each standard was transferred in triplicate in a 96-well plate and 200 µl of working reagent was added in each. The plate was shaken for 30 s on a plate shaker and incubated at 37 °C for 30 min. The plate was returned to RT and the absorbance was taken at 562 nm on a multimode plate reader, infinite M200 Pro, TECAN. From the calibration plot the concentration of total protein in the unknown sample was calculated.

Western Blot. The necessary volume of cell lysate was added in each well of the gel to have 5 µg total protein. An equal volume of loading buffer was added, and the gels were running for approximately 1 h at 0.4 A. The dry transfer of the proteins to the membrane was performed using iBlot 2, ThermoFisher Scientific, at 20 V for 1 min, 23 V for 3 min and 25 V for 1 min. Successful transfer was confirmed by Ponceau S. The membrane was blocked by 5% BSA solution in PBST (PBS + 0.1% tween-20) for 2 h on a rocking platform. Proteins were probed with monoclonal antibodies prepared in 3% BSA solution for 1 h on a rocking platform. After thorough washing, the secondary antibody conjugated with horseradish peroxidase was incubated with the

membrane in 3% BSA for 1 h at RT. After washing off excess secondary antibody, bands were stained with Western ready and imaged on a ChemiDoc XRS+ system, Bio-Rad.

4.3 Results and Discussion

The way in which magnetic nanomaterials convert magnetic work to heat was explained in section 2.1.1. Although ferri- and ferromagnetic particles dissipate greater heat compared to superparamagnetic NPs, the field amplitude limit for application on human subjects does not allow for the utilisation of the full hysteresis loop, substantially reducing their heating efficiency. In multi-domain particles, the domain walls are less energetically demanding to move and take place at lower fields allowing for the full hysteresis loop at low fields[2]. Nevertheless, for clinical applications none of these two systems are suitable due to their permanent magnetic moment, restating the need for superparamagnetic NPs.

An alternative to MFH, is PTT. In this case, light, instead of magnetic energy, is converted into heat. To achieve light to heat conversion, a material must absorb light. Materials that are coloured under visible light indicate the absorbance of certain wavelengths of radiation. Fe_3O_4 and Fe_3O_4@γ-Fe_2O_3 are black/brown which indicates the absorption of the whole visible spectrum.

4.3.1 Considerations for Magnetic Fluid Hyperthermia

In the case of MFH, the field and frequency applied should be carefully selected to prevent damage to healthy tissue. If the product of frequency and field is above a certain limit induction heating will occur and the specificity of the treatment will be lost[60]. Such a criterion was first set in 1984 and has been the subject of debate ever since. This criterion is known as the Brezovich criterion and has a value of 4.5×10^8 $Am^{-1}s^{-1}$. Those experiments are not known to have been repeated and the use of smaller coils with multiple turns and off-axis field direction as opposed to a large big turn used in 1984 are substantially different conditions. These conditions are expected to reduce eddy currents and hence allow for a larger product of frequency and field. The current revised working value is set at 5×10^9 $Am^{-1}s^{-1}$ which is ten times larger than the

previous limit value. This safety limit has been adhered to in the following magnetothermal experiments.

4.3.2 Considerations for Photothermal Therapy

On the other hand, one should consider possible obstacles for the clinical translation of PTT. Unless the light will be delivered invasively, i.e. by a fibre optic, the skin is not invisible to all wavelengths of light. There are molecules in the body that can absorb or scatter light some of which are listed below.

Absorption	• Haemoglobin • Water • Melanin • Fat
Scattering	• Cell membrane • Mitochondria • Nuclei • Whole cells

Therefore, the wavelength of light that can penetrate the skin is limited to the near-infrared window between 650-1350 nm. In addition, the penetration depth is not very deep and is in the order of cm, hence non-invasive PTT should work best for superficial tumours.

4.3.3 Biocompatibility Studies

MTT is a colourimetric assay for the evaluation of cell metabolic activity as an indicator of alive and dead cells. Reduced nicotinamide adenine dinucleotide phosphate (NADPH)-dependent cellular oxidoreductase enzymes present within the cells can reduce a yellow soluble tetrazolium dye to its insoluble purple formazan as shown in Figure 55. This assay is being routinely used to screen materials as a first line of testing. It is a simple assay and only requires a UV-Vis plate reader to assess.

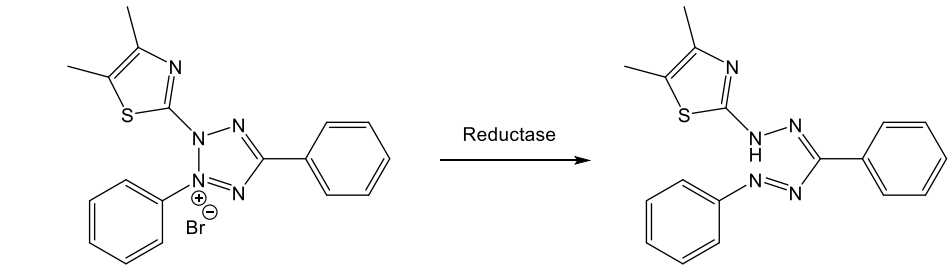

Figure 55: Principle of the MTT assay where a soluble tetrazolium is reduced to an insoluble purple formazan.

The LDH assay is another tool to assess the cytotoxicity of an agent by assessing the integrity of the cell membrane. It detects an enzyme in the growth medium which is only released from the cell upon membrane permeabilization which itself is indicative of cellular damage. This initiates a series of reactions eventually converting a tetrazolium salt to a formazan (Figure 56).

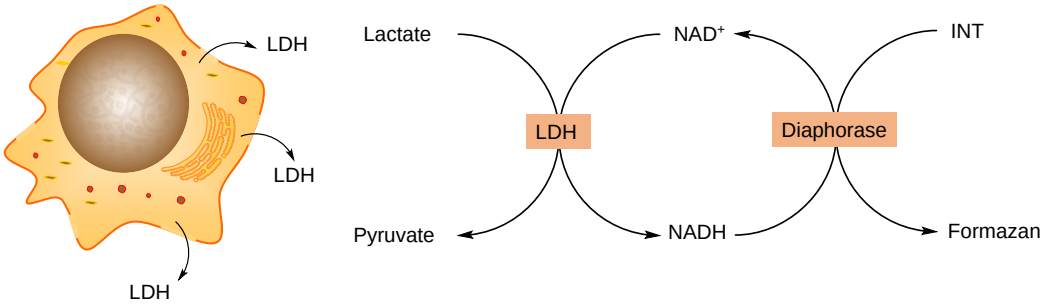

Figure 56: Principle of the LDH assay where leaking LDH results in a coloured product.

A clonogenic assay evaluates the ability of cells to survive and proliferate after treatment of a drug or radiation. This assay was used to evaluate any long-term effect of NP treatment. With conventional assays such as the MTT or LDH assays the assessment is based on immediate effects of toxicity while clonogenic assay requires the cells to grow over long periods of time therefore assessing their proliferation. A typical procedure involves the treatment of cells which are then plated as single cell suspensions and at low numbers. The individual cells eventually form colonies (at least 50 cells to score) which are stained and counted (Figure 57).

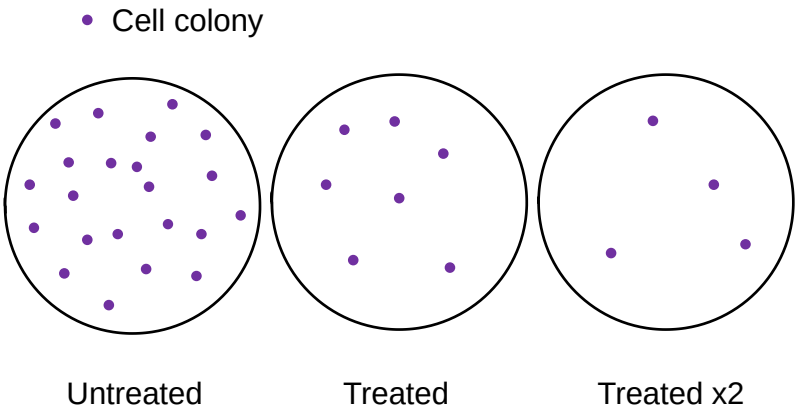

Figure 57: Illustration of colony formation for control and treated cells.

Prior to selecting a cell line to assess the cell viability after treatment with NPs, the NP uptake was evaluated between brain glioblastoma U87-MG and breast adenocarcinoma MCF-7 cells, both applicable for hyperthermia treatment, by single-cell magnetophoresis as described recently[122]. U87-MG cells were uptaking NPs more readily compared to MCF-7 as shown in Figure 58A and hence were used to assess the toxicity of the materials. To visualize the uptake of NPs, both cell lines were incubated with NPs for 24 h and then the cells were washed, fixed and the iron content stained with Prussian blue formation. The blue colour indicative of iron ions are profound in U87-MG cells while no blue colour could be detected inside the MCF-7 cells as it can be seen in Figure 58B and C respectively.

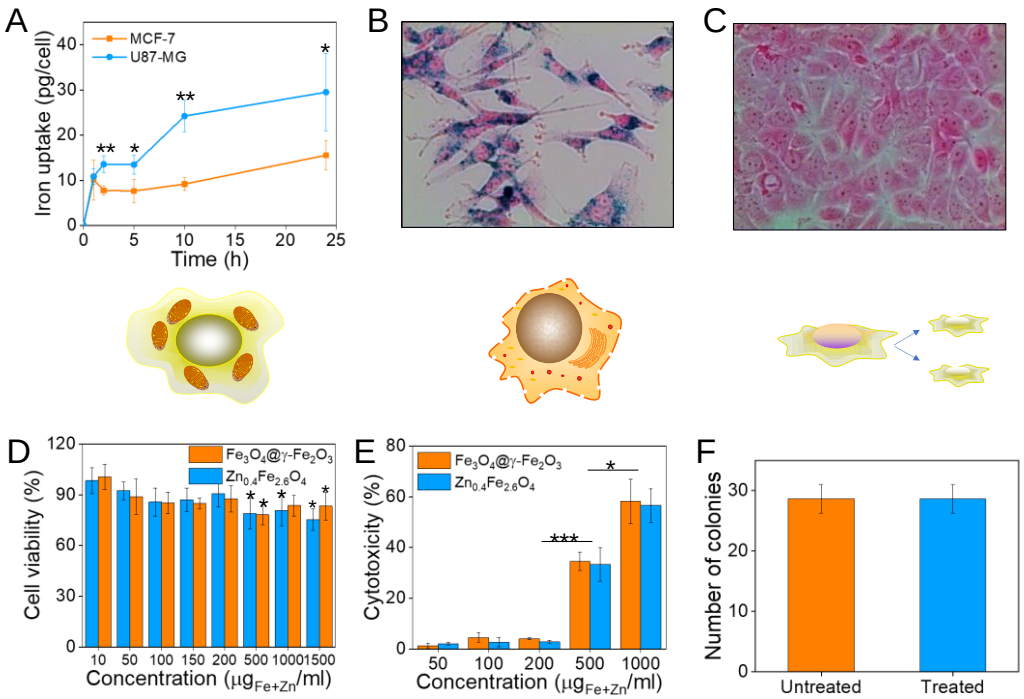

Figure 58: A) Iron uptake of U87-MG and MCF-7 cells as calculated from single-cell magnetophoresis incubated with 10 μg_{Fe+Zn}/ml $Zn_{0.4}Fe_{2.6}O_4$ NPs respectively for up to 24 h. B) and C) Optical microscope images of stained, with nuclear fast red and acidic potassium hexacyanoferrate (II) solutions, U87-MG and MCF-7 cells with incubated with 10 μg_{Fe+Zn}/ml $Zn_{0.4}Fe_{2.6}O_4$ NPs respectively for 24 h. D) Cell viability of U87-MG cells as measured by the MTT assay after treatment with Fe_3O_4@γ-Fe_2O_3 and $Zn_{0.4}Fe_{2.6}O_4$ NPs at different concentrations for 24 h. E) Cytotoxicity of Fe_3O_4@γ-Fe_2O_3 and $Zn_{0.4}Fe_{2.6}O_4$ NPs obtained by the LDH assay. F) Number of colonies formed from single-cell suspensions of U87-MG cells via clonogenic assay after treatment of cells with 0.2 mg_{Fe+Zn}/ml $Zn_{0.4}Fe_{2.6}O_4$ NPs for 24 h. Values reported as mean ± SEM. p-Values were calculated based on a two-tailed t-test: * indicates $p<0.001$, ** indicates $p<0.01$ and * indicates $p<0.05$.**

To quantify cell viability after treatment with NPs, U87-MG cells were incubated with Fe_3O_4@γ-Fe_2O_3 and $Zn_{0.4}Fe_{2.6}O_4$ NPs for 24 h after which the reduction of the tetrazolium salt was monitored by UV-Vis spectroscopy. Neither of the materials show significant decrease of cell viability up to 1500 μg_{Fe+Zn}/ml as shown in Figure 58D, concentrations much higher than previously tested[58,92]. Nanomaterials decreased cell viability to 80% for concentrations over 500 μg_{Fe+Zn}/ml. In addition to MTT, the enzyme LDH was measured as an indicator of cellular membrane integrity, another marker for cell health. Similarly to the MTT assay, the LDH assay reveals a similar trend

with concentrations over 500 μg_{Fe+Zn}/ml having a negative effect on the cells shown in Figure 58E. Further to metabolism and membrane integrity of cells which are short-term markers of cell health, a clonogenic assay was used to evaluate the longer-term impact of NPs. Accumulation of genetic changes, i.e. through reactive oxygen species (ROS) which can damage DNA and produce malfunctioning proteins whose accumulation can lead to apoptosis[123]. A clonogenic assay uses the cell cycle and proliferation of cells to assess cell health. Treating the cells with a high concentration of NPs of 200 μg_{Fe+Zn}/ml would exclude damages caused by metabolic and membrane integrity effects as seen previously with the MTT and LDH assays respectively and probe any genetic changes that would manifest themselves in longer timeframes than those used in the colourimetric assays. Cells formed the same numbers of colonies whether treated with $Zn_{0.4}Fe_{2.6}O_4$ NPs or not indicating that they are tolerated and do not alter protein expression or arrest the cell cycle, shown in Figure 58F. The fact that both materials exhibit the same trend in cell viability by two different assays, the unaffected proliferation when treated with NPs as well as the fact iron oxide is an FDA approved material shows that the developed $Zn_{0.4}Fe_{2.6}O_4$ NPs is a biocompatible and well-tolerated material.

4.3.4 Application in Hyperthermia

Magnetic NPs are typically used in MFH where their magnetic relaxation increases the internal energy of the system which dissipates to heat. Current obstacles for the clinical translation of MFH are the high concentration of NPs that need to reach the tumour due to the limited heating of superparamagnetic NPs. Many have relied on intratumoural injections to achieve the concentration of NPs needed at the site of interest, but this procedure is unlikely to become medical practice. Other potential approaches include the preparation of anisotropic NPs which have a higher magnetothermal conversion compared to isotropic NPs although no longer superparamagnetic, a prerequisite for *in vivo* applications. The Brezovich criterion is also an upper limit of the product between the frequency and amplitude of the AMF to prevent unspecific heating from induction of eddy currents which in attempts to make NPs heat is sometimes exceeded. Herein, superparamagnetic isotropic NPs of Fe_3O_4@γ-Fe_2O_3 and $Zn_{0.4}Fe_{2.6}O_4$ compositions were compared whilst complying with

the revised Brezovich criterion ($H \times f = 5 \times 10^9$ $Am^{-1}s^{-1}$).Our results indicate a magnetothermal performance typical of superparamagnetic NPs as shown in Figure 61D and E. Depending on the product of frequency and amplitude, the values of SAR and absolute change in temperature vary proportionally as shown in Table 6.

Table 6: Absolute change in temperature and SLP values of Fe_3O_4@γ-Fe_2O_3 and $Zn_{0.4}Fe_{2.6}O_4$ NPs at 20 mg_{Fe+Zn}/ml subjected to an AMF with different product of frequency and amplitude. Values reported as mean ± SEM. p-Values were calculated based on a two-tailed t-test: ** indicates $p<0.01$.

		ΔT ± S.D (°C)		SLP ± S.D (W/g_{Fe+Zn})	
Field (kA/m)	**Frequency (kHz)**	**Fe_3O_4@γ-Fe_2O_3**	**$Zn_{0.4}Fe_{2.6}O_4$**	**Fe_3O_4@γ-Fe_2O_3**	**$Zn_{0.4}Fe_{2.6}O_4$**
10.4	342	10.3 ± 1.2	10.7 ± 1.5	21.6 ± 2.8	23.4 ± 3.8
	471	17.9 ± 2.9	18.1 ± 2.7	38.5 ± 5.5	40.5 ± 6.8
Significance		**	**	**	**
14.4	342	17.6 ± 2.4	17.4 ± 2.2	37.2 ± 6.6	37.8 ± 5.9
	471	24.9 ± 2.2	25.0 ± 3.4	63.1 ± 6.6	63.1 ± 10.1
Significance		**	**	**	**

It is observed that the change in temperature achieved after heating the aqueous dispersions of NPs is proportional to concentration with Fe_3O_4@γ-Fe_2O_3 and $Zn_{0.4}Fe_{2.6}O_4$ NPs producing the same amount of heat, approximately 1 °C per mg_{Fe+Zn}. The SAR value which is a measure of the rate of heating (also called SLP) is desirable to be high to prevent thermal energy from dissipating to the surrounding tissue before it can elevate the tumour temperature. This property was found to be independent of concentration or the material and with a value typical of superparamagnetic NPs, in the 50-100 W/g_{Fe} range. Changing the frequency and amplitude of the AMF whilst remaining within the acceptable product between the two, the same absolute change in temperature and SAR is obtained as shown in Figure 59A and B.

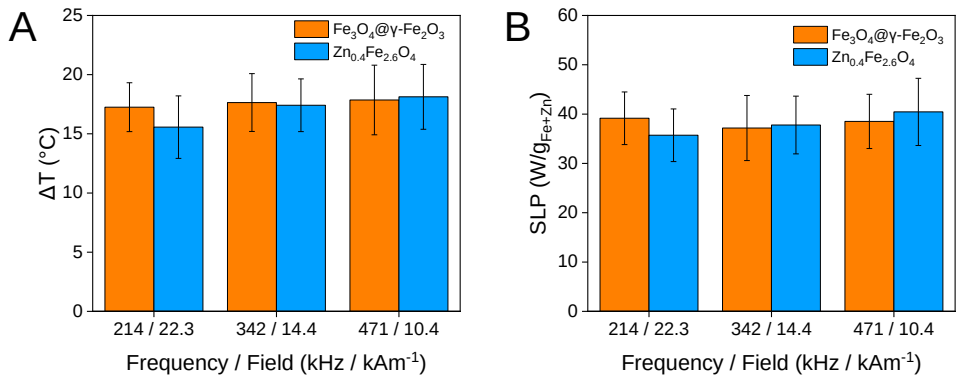

Figure 59: A) and B) is the absolute change in temperature and SLP values respectively, of Fe_3O_4@γ-Fe_2O_3 and $Zn_{0.4}Fe_{2.6}O_4$ NPs at a concentration of 20 mg_{Fe+Zn}/ml subjected to AMF of different combinations of frequency and field but the same product of the two (n = 3). Values reported as mean ± SEM.

An augmentation in performance with NPs of same size and morphology but higher M_S (Fe_3O_4@γ-Fe_2O_3 vs $Zn_{0.4}Fe_{2.6}O_4$) was not observed according to $P = \frac{\mu_0 \pi \chi_0 \nu^2 H^2 \tau_{N/B}}{\left[1+(\nu\tau_{N/B})^2\right]}$, where $\chi_0 = \frac{\mu_0 M_S^2 V}{kT}$, showing a dependence of the power generated to the square M_S value of the NPs. From the magnetic characterization it can be concluded that the introduction of Zn^{2+} causes magnetic softening and consequently a decrease in the K value reducing particle motion contribution to heating.

Recently, the ability of iron oxide NPs to produce heat from light was shown[5,122]. Herein, a thorough comparison between the two heating modalities, MFH and PTT, was evaluated and for the first time, the effect of the smaller bandgap of $Zn_{0.4}Fe_{2.6}O_4$ compared to iron oxide NPs (1.07 vs 1.42 eV respectively) was assessed for enhanced photothermal performance. Light wavelengths tested are within the near-infrared biological window[11] where water and other biomolecules do not quench the light (Figure 60).

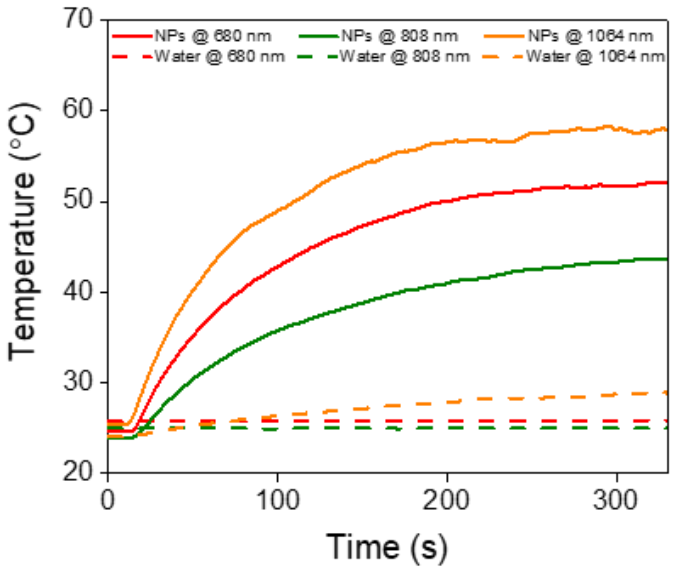

Figure 60: PTT treatment of aqueous suspension of NPs with 680, 808 and 1064 nm lasers compared to water only with the same lasers.

The photothermal performance of NPs is independent of laser wavelength at saturating conditions and it increases linearly with power density up to the values tested as shown in Figure 61A. In contrast to magnetothermal conversion, photothermal conversion saturates at very low concentrations (1 mg_{Fe+Zn}/ml) with a much bigger effect than MFH at much lower concentrations, Figure 61B. This is explained based on the limiting factor being the incoming light and not the light absorbing material, which when enough material is present, it will absorb the whole energy of the incoming light. SAR, also a measure of heating rate, is therefore inversely proportional to concentration in PTT, Figure 61C.

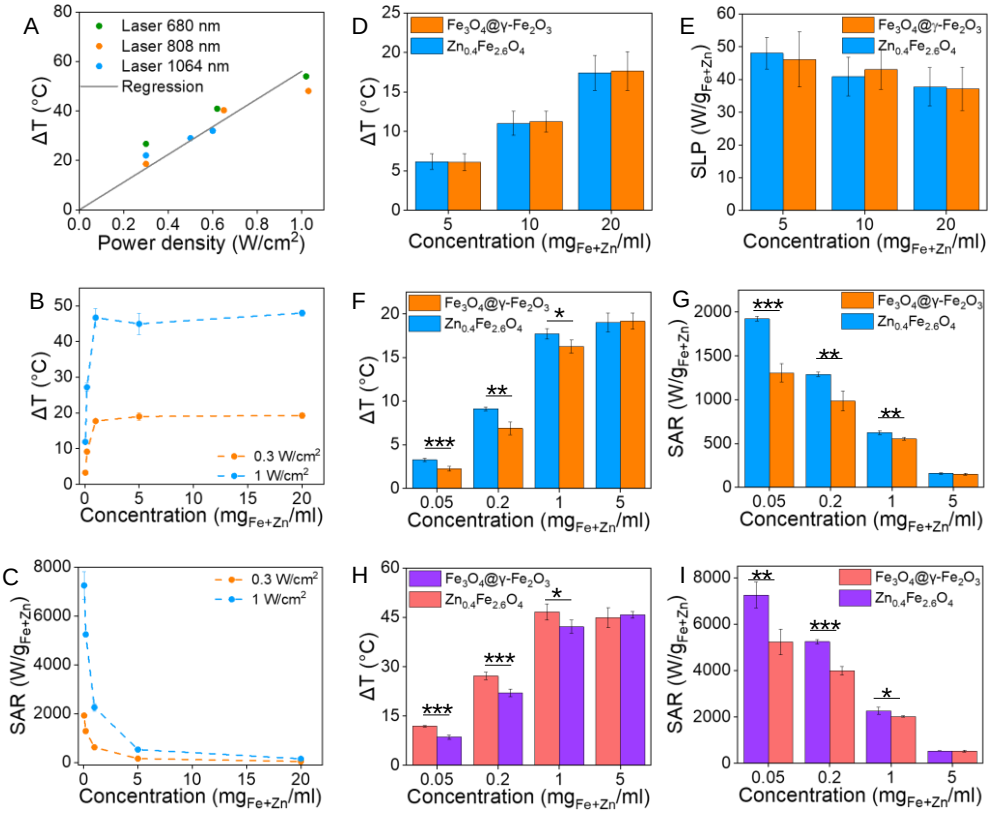

Figure 61: A) Change in temperature dependence on the power density of different wavelength lasers at a power density of 0.3 W/cm². B) Change in temperature and C) SAR values of $Zn_{0.4}Fe_{2.6}O_4$ NPs at different concentrations irradiated with an 808 nm laser at 0.3 and 1 W/cm². D) and E) Change in temperature and SAR values respectively of Fe_3O_4@γ-Fe_2O_3 and $Zn_{0.4}Fe_{2.6}O_4$ NPs at different concentrations under an AMF (f=342 kHz, H=14.4 kA/m). F) and G) Change in temperature and SAR values of Fe_3O_4@γ-Fe_2O_3 and $Zn_{0.4}Fe_{2.6}O_4$ NPs irradiated with 0.3 W/cm² at 808 nm and H) and I) show the same for 1 W/cm². Values reported as mean ± SEM. p-Values were calculated based on a two-tailed t-test: * indicates $p<0.001$, ** indicates $p<0.01$ and * indicates $p<0.05$.**

As the material has a dark colour with high molar attenuation coefficient (ε=111.1 $M^{-1}cm^{-1}$, derivation from Figure 62) the higher the concentration the less penetrating distance the light can travel before it is absorbed.

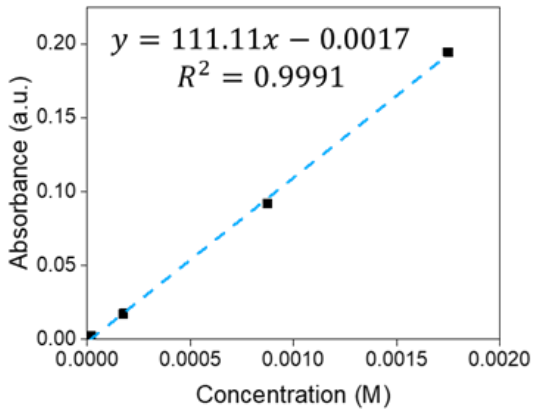

Figure 62: Absorbance of 808 nm light of $Zn_{0.4}Fe_{2.6}O_4$ NPs at different concentrations. The slope yields the molar attenuation coefficient according to Beer-Lambert law.

It is observed that $Zn_{0.4}Fe_{2.6}O_4$ NPs exhibit a higher photothermal effect compared to Fe_3O_4@γ-Fe_2O_3 NPs in both their ability to increase temperature and the rate with which they do so as it can be seen in Figure 61F and G. The effect is profound up to the saturating concentration of 1 mg_{Fe+Zn}/ml. The trend continues with increasing the power density to 1 W/cm^2, the $Zn_{0.4}Fe_{2.6}O_4$ NPs outperform Fe_3O_4@γ-Fe_2O_3 with decreasing concentration increasing the effect. At the minimum concentration tested of 0.05 mg_{Fe+Zn}/ml, $Zn_{0.4}Fe_{2.6}O_4$ NPs had SAR values of 1900 and 7000 W/g_{Fe+Zn} for 0.3 and 1 W/cm^2 while Fe_3O_4@γ-Fe_2O_3 had only 1300 and 5000, respectively. In comparison, MFH at a concentration of 1 mg_{Fe+Zn}/ml does not show any detectable increase in temperature. Comparing the optimal conditions for MFH (20 mg_{Fe+Zn}/ml) and PTT (1 mg_{Fe+Zn}/ml) the change in temperature is the same at about 18 °C for both modalities whilst the SAR value of PTT is more than 16 times bigger with 20 times less concentration. The ability to increase the heating effect whilst reducing the amount of material needed might offer a solution for the clinical translation of localized hyperthermia.

Both heating modalities have then been assessed *in vitro*, within cancer cells. Previous reports showed the magnetothermal effect diminishing once the NPs are associated with the cells while the photothermal effect remains unaffected[77]. This is in relation to the environment-dependent mechanism of

magnetothermal conversion (reorientation in space) and the independent mechanism of photothermal conversion (production of phonons by vibrational relaxation of excited electrons). In agreement with previous studies, the NPs presented herein experienced a small decrease in the magnetothermal effect (35 W/g_{Fe+Zn} vs 45 W/g_{Fe+Zn} for cellular confinement and aqueous suspension respectively), as shown in Figure 63A. This is because these NPs have a low shape anisotropy and therefore an order of magnitude less K_{eff} compared to other NPs such as magnetosomes, nanocubes or nanoflowers which suffer a ten-fold decrease in their SAR values[77,124]. This indicates that the NPs are relying more on Néel than Brown relaxation, the first is environment independent whilst the latter is environment-dependent due to physical reorientation of the particle, minimally affecting their heating properties in aqueous dispersions and in cells. Similarly, PTT results are in agreement with literature which states that the effect remains unaffected both in suspension and in cellular confinement shown in Figure 63A. It is important to note that the final temperature reached remained unchanged for both MFH and PTT in aqueous dispersions and in cells as shown in Figure 63B, only the heating rate changed slightly for MFH. Nevertheless, the change in temperature reached after incubation of $Zn_{0.4}Fe_{2.6}O_4$ NPs at a concentration of 0.2 mg_{Fe+Zn}/ml for 24 h with U87-MG cells (final concentration in cell pellet was 2 mg_{Fe+Zn}/ml) was inadequate for therapy using MFH while PTT reached thermoablation-level temperatures shown in Figure 63C. The effect of both thermotherapies was evaluated on live U87-MG cells with MFH achieving only 30% cell death while PTT achieved an impressive 100% cell death after 10 min treatment with a low laser power density of 0.3 W/cm^2 shown in Figure 63D. The above findings illustrate that semiconductor PTT is a more efficient thermotherapy than MFH and that Zn^{2+} doping in ferrite structures enhances the photothermal effect further.

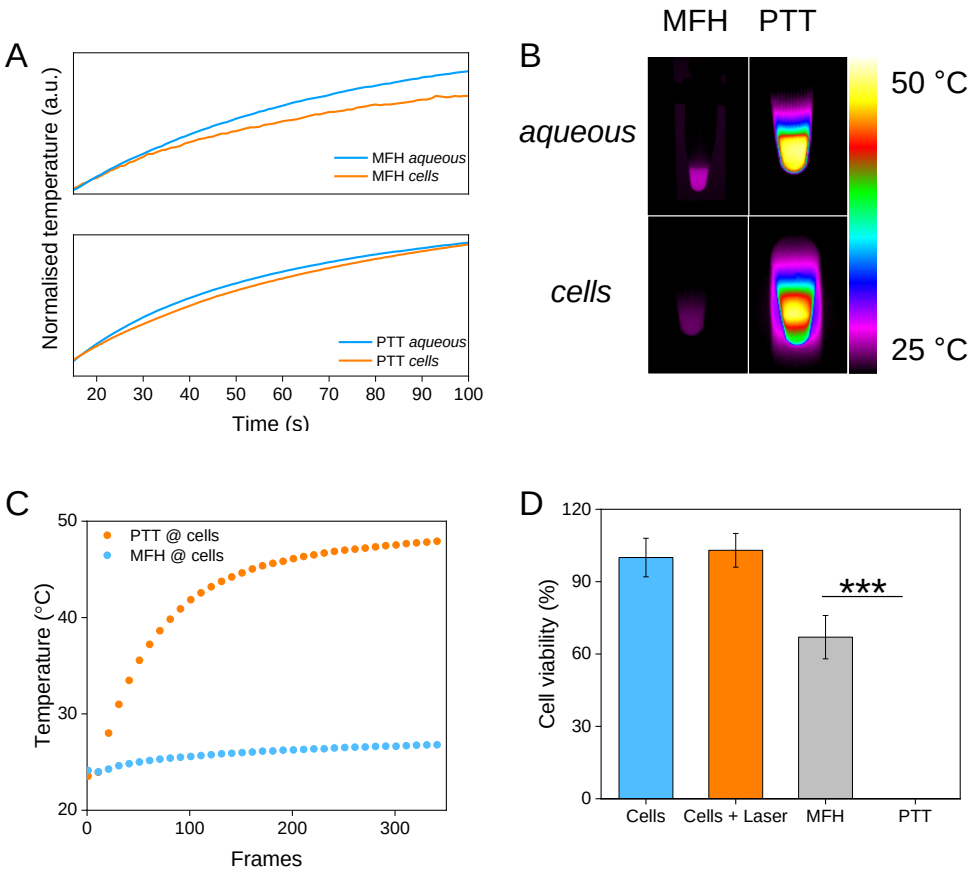

Figure 63: A) Initial part of heating curves of $Zn_{0.4}Fe_{2.6}O_4$ NPs *in situ* and *in vitro* at a concentration of 2 mg_{Fe+Zn}/ml under MFH and PTT treatment. B) Infrared images of NPs in suspension and in cells at the same concentration under MFH and PTT. C) Absolute temperature of U87-MG cell pellet with $Zn_{0.4}Fe_{2.6}O_4$ NPs at 2 mg_{Fe+Zn}/ml treated with MFH and PTT. D) Cell viability after MFH and PTT treatment as obtained from the Alamar blue assay. Values reported as average ± SD. p-Values were calculated based on a two-tailed t-test: * indicates $p<0.001$.**

4.3.4.1 Phenotypic and Biochemical Changes of U87-MG Cells After Photothermal Treatment - Identifying a Point-of-no-Return

Cells can recover from extreme damage in a process called anastasis[125] only recently discovered. This can be beneficial if exploited for the regeneration of neural cells or heart cells[126] which are for life as well as other diseases[127]. On the other hand, the same mechanism can also lead to cancer relapses[128]. Cells with an apoptotic phenotype are often assumed dead although recently, they have been shown to come back to life even after typical signs of cell death such as nuclear pyknosis, blebbing, changes in membrane integrity, DNA damage and others[125,128]. To this end, there has been a change of identifying

cell death beyond just morphological changes to include molecular changes and biochemical processes.

In order to develop an effective PTT cancer treatment and prevent relapses while minimising collateral damage to healthy cells, the minimum treatment time should be determined which would achieve a point-of-no-return for the target cell population. To this end, the morphological and molecular changes have been explored towards identifying a suitable treatment timeframe for the minimum laser exposure time to achieve complete cell death, even though a point-of-no-return remains controversial among experts[129]. It was shown in Figure 63D, that 10 min of treatment was enough time to achieve 100% cell death as determined by viability assay. Those experiments were performed in the small volume of an Eppendorf tube. Even after surgical removal of tumours, treating the tumour bed with PTT to kill residual cells should require a lot of time. Therefore, in the following experiments shorter times of 0.5-, 1- and 2-min laser exposure time were used to simulate practicality in clinical practice.

Cells loaded with $Zn_{0.4}Fe_{2.6}O_4$ NPs undergone treatment with the laser and monitored over time. Their phenotypic changes were imaged as shown in Figure 64.

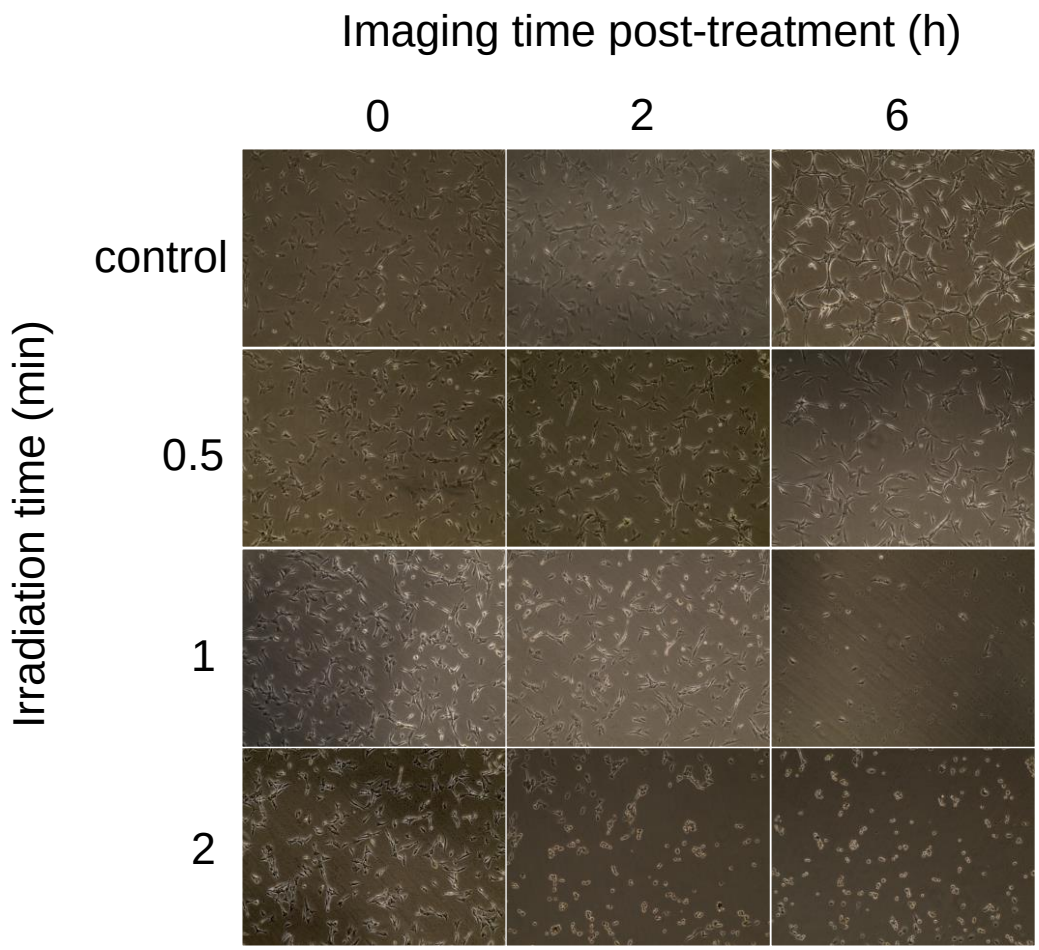

Figure 64: Optical imaging of U87-MG cells treated with $Zn_{0.4}Fe_{2.6}O_4$ NPs and laser irradiation for different times and their time-resolved morphological changes.

Untreated cells and NPs-loaded cells treated with 0.5-min laser exposure continue to normally grow indicating that the temperature reached was not high enough to induce cellular death. In contrast, cells treated with 1-min or longer show extensive cell death with 2 min exposure only showing detached cells (indicative of death) within the direct illumination area. Cells at the perimeter of direct illumination (Figure 66A) where still attached to the petri dish even though the global temperature of the dish was elevated to the same degree (Figure 65).

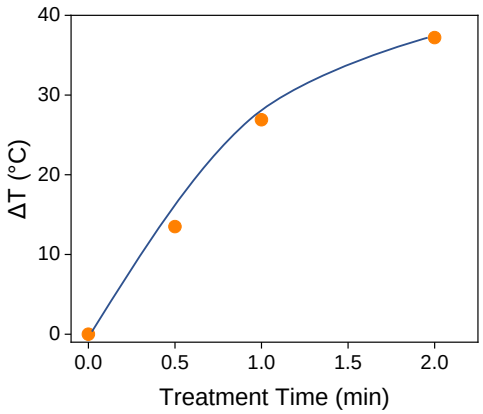

Figure 65: Absolute change in temperature of NPs-loaded U87-MG cells treated with 0.3 W/cm^2 808 nm laser for different times. The line is a guide to the eye.

Morphologically, cells at the periphery of the illumination area were identical with untreated cells despite the global temperature increase within the dish. Consequently, the cell-impermeant fluorescent dye DRAQ7 was used to differentiate permeabilized cells which is an early sign of cell death shown in Figure 66B. Immediately after treatment, no group shows significant dye activation. After 2 h, cells irradiated with laser start showing fluorescence even at 0.5 min which increases with time as evidenced by the increased signal. Cells irradiated with 1 min or more show significant blebbing at 2-6 h post-treatment which then disappears showing that cells are recovering. Morphologically healthy cells are permanently stained with DRAQ7 indicating a transient membrane permeabilization with consequent repair. This shows that cells not-directly irradiated with laser can suffer from damage due to global temperature increase but are able to restore normal functions and proliferate.

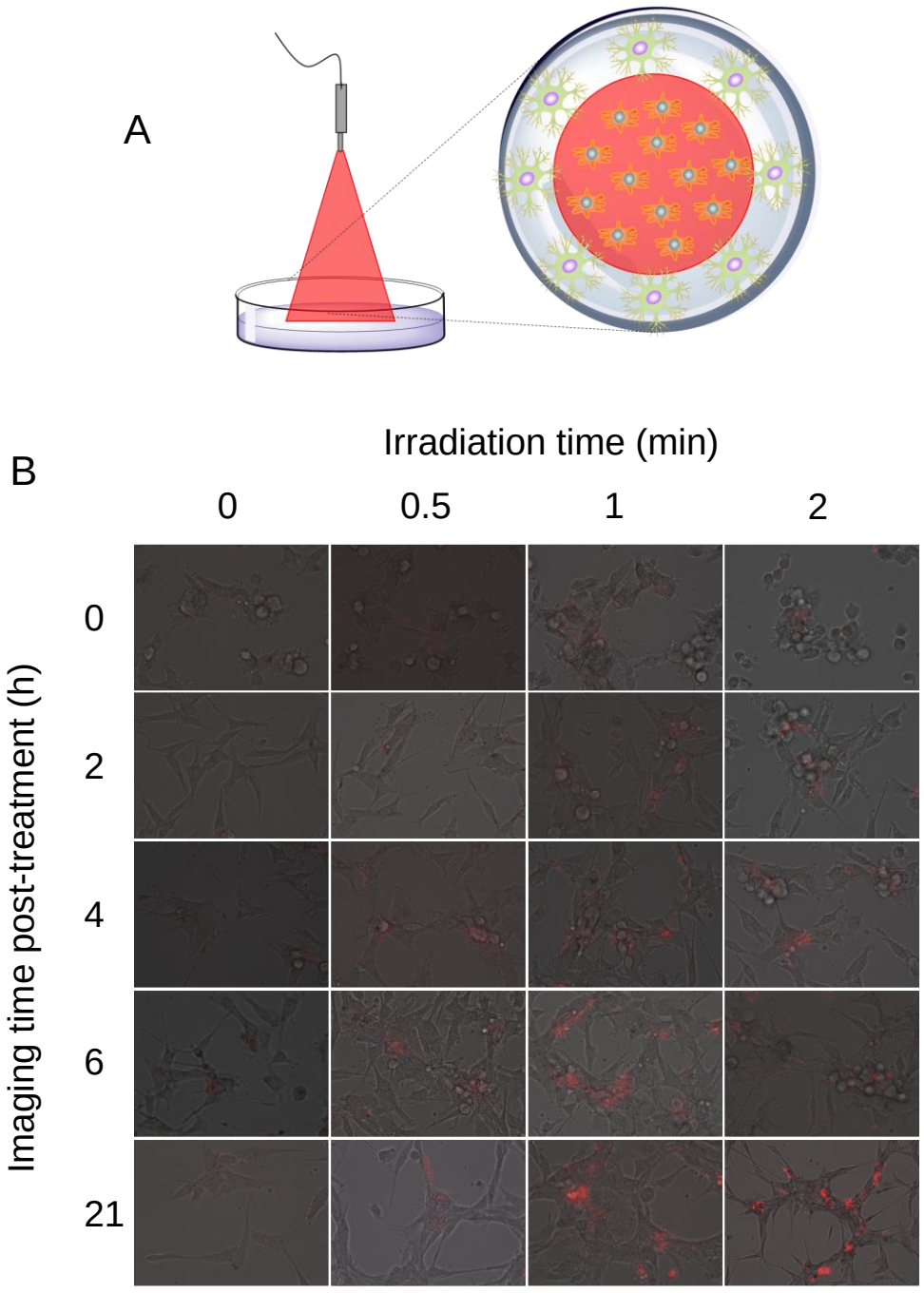

Figure 66: A) Schematic of laser treatment set-up on live cells. B) Merged images of optical and fluorescent microscopy of DRAQ7 loaded U87-MG cells treated with 0.3 W/cm^2 808 nm laser for different times and their time-dependent permeabilization.

Protein Expression. Proteins are essential parts of organisms and they participate virtually in every process. Cell homeostasis is also regulated by the production and degradation of proteins and so is survival and death. Cell death is often characterised based on the pathway leading to cell death with specific morphological and biochemical processes. Apoptosis and necrosis are the two

cell death pathways of interest herein where the first is the controlled dissection of cellular organelles and proteins and the consequent engulfment from other cells while necrosis is characterised by an uncontrolled death releasing cellular components on the surrounding cells, often leading to inflammation[130]. Ideally, the treatment trigger should cause the cells to undergo apoptosis irreversibly. For this purpose, a selection of proteins involved in apoptosis and survival mechanisms, as schematically shown in Figure 67, were monitored to reveal the biochemical impact of PTT on U87-MG cells and possibly identify, through morphological and biochemical data, an optimum treatment time.

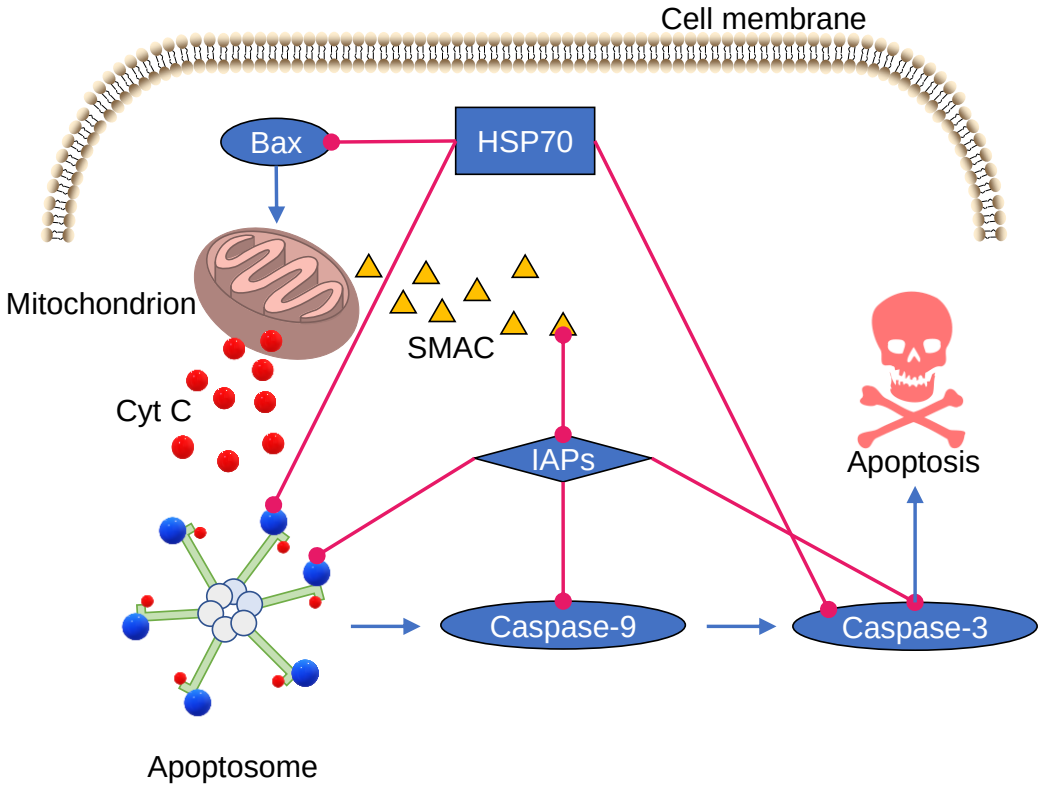

Figure 67: Cell signalling in selected apoptotic pathways.

Caspases. Caspases is a family of protease enzymes playing essential roles in programmed cell death[131]. Their function maintains cell homeostasis. While their overactivation leads to disease such as neurodegenerative diseases, their insufficient activation can lead to cancer and infection[130]. Caspases have been targeted to combat cancer[131]. Caspases are activated by the release of cytochrome C from mitochondria to the cytosol which assemble the

apoptosome converting inactive procaspases to the active enzymes, the caspases[131].

Caspase-3 is an executioner protein of apoptosis and plays a major role in chromatin condensation and DNA fragmentation. Its overexpression is indicative of apoptotic mechanisms being activated. Qualitative and quantitative analysis of caspase-3 regulation is shown in Figure 68. There is a physiological level of caspase-3 present in the control group shown in Figure 68A which does not show in fluorescent images (Figure 68B). Upon treatment with laser for 0.5 and 1 min, the levels of caspase-3 increase significantly and proportionally to the treatment time. In contrast, the levels of caspase-3 expression in the group treated with laser for 2 min shows significantly lower fluorescent signal. This might be the result of immediate cell death without undergoing the apoptotic signal transduction pathway, typical of necrosis since at 0 min after treatment cells treated for 2 min are already showing decreased fluorescence in Figure 68A. From the fluorescent images in Figure 68B, fluorescent intensity and therefore the level of caspase-3 expression 6 h after laser treatment seems similar. In conjunction with Figure 64 which shows the vast majority of cells detached, it is assumed that once fluorescence intensity is normalised to cell number, the caspase-3 level should be at least similar between groups 1-min and 2-min treatment.

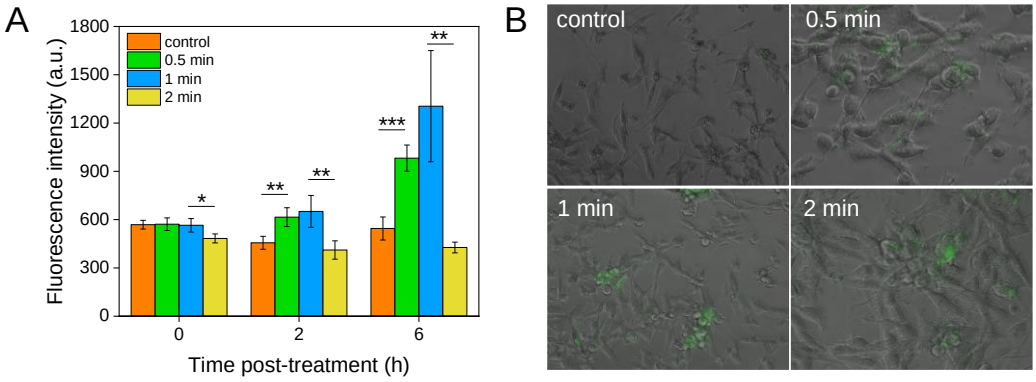

Figure 68: A) Quantitative measurement of caspase-3 (n = 3). B) Merged images of optical and fluorescent microscopy for qualitative detection of caspase-3 6 h post-treatment. Values reported as mean ± SD. p-Values were calculated based on a two-tailed t-test: * indicates $p<0.001$, ** indicates $p<0.01$ and * indicates $p<0.05$.**

Cytochrome C. Under stress, cells elevate the production of ROS in the mitochondria. The oxidation processes occurring from ROS, release cytochrome C to the cytosol which is normally located within the mitochondria. Its release to the cytoplasm is involved in the formation of the apoptosome which activates procaspase-9 leading to the activation of caspases-3 and -7 leading to onset of apoptosis[132].

Visualisation of ROS was performed on NPs-loaded U87-MG cells, cells treated with TBHP as a positive control and NPs-loaded cells irradiated with the laser for 0.5- and 1-min and imaged 2 and 6 h post-treatment as shown in Figure 69. At 2, 4 and 6 h after laser treatment, cells show an increase in ROS production for all treatment times. At 6 h, the ROS increase observed for 0.5 min laser treatment is statistically significant compared to control. Throughout, levels of ROS for 1- and 2-min laser treatment appear equal to or lower than controls. Taking into account the fluorescent images of 0.5- and 1-min laser treatment showing a higher signal for the longer treatment time it seems likely that cells at 2 min have undergone necrosis bypassing the intrinsic apoptotic pathway while cells treated with laser for 1-min are probably undergoing apoptosis and necrosis simultaneously explaining the reduced total fluorescent signal. This takes into account both the higher green fluorescent intensity in fluorescent imaging compared to controls but also the equal value of total fluorescent between control group and 1 min laser treatment time shown in Figure 68A.

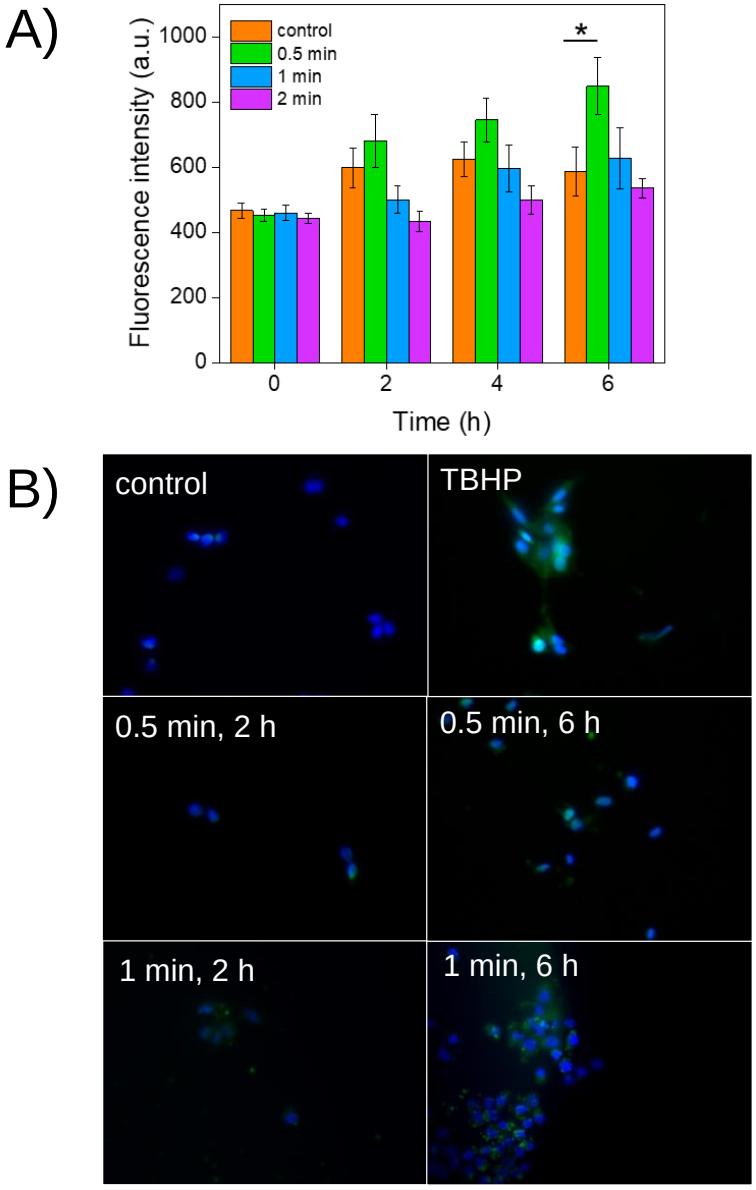

Figure 69: A) Quantitative measurement of ROS (n = 3) and B) Fluorescent microscopy images of U87-MG cells up to 6 h after treatment. Values reported as mean ± SD. p-Values were calculated based on a two-tailed t-test: * indicates $p<0.05$.

Heat Shock Protein 70. HSP70 is a family of proteins produced in response to biological stress including thermal shock[133]. It is a crucial part of cell's machinery in protein folding and protection from stress[133]. It stabilizes proteins against aggregation and remodels folding. They participate in protein disposal of damaged and defective proteins. HSP70 also inhibit apoptosis by blocking the binding of procaspase-9 to the apoptosome preventing the formation of caspase-3[134].

X-Linked Inhibitor of Apoptosis. XIAP, the most potent IAP identified[135], is an apoptotic suppressor by mediating the proteasomal degradation of apoptotic proteins such as caspase-3 and SMAC[136]. It is an inhibitor of caspase-3, -7 and -9. XIAP does not interfere with cytochrome C release[137].

Using western blot to qualitatively estimate the expression of HSP70 and XIAP, whole cell lysates have been used as shown in Figure 70. HSP70 (M_W=70 kDa) is upregulated compared to controls for all treatment times. XIAP on the other hand, shows a decreasing trend from controls up to 1-min treatment where cells exposed to 2-min laser irradiation show an increase of XIAP level close to controls. HSP70 levels are expected to increase as temperature denatures proteins and puts cell under thermal stress as it is this family of proteins who are responsible to maintain cell health including protein stabilisation and refolding. As shown in Figure 67, SMAC is released from mitochondria along with cytochrome C. As a negative regulator of XIAP its effect is observed as a decreased level of XIAP on western blot. This would prevent the inhibition of caspases from XIAP and allow for caspase dependent apoptosis to proceed and as such XIAP downregulation is considered another sign of apoptosis initiation[138]. As explained earlier, after 2-min irradiation time, cells directly illuminated are entirely detached hence they washed away before lysis. The level of XIAP measured then, must represent the population on the periphery of the petri dish.

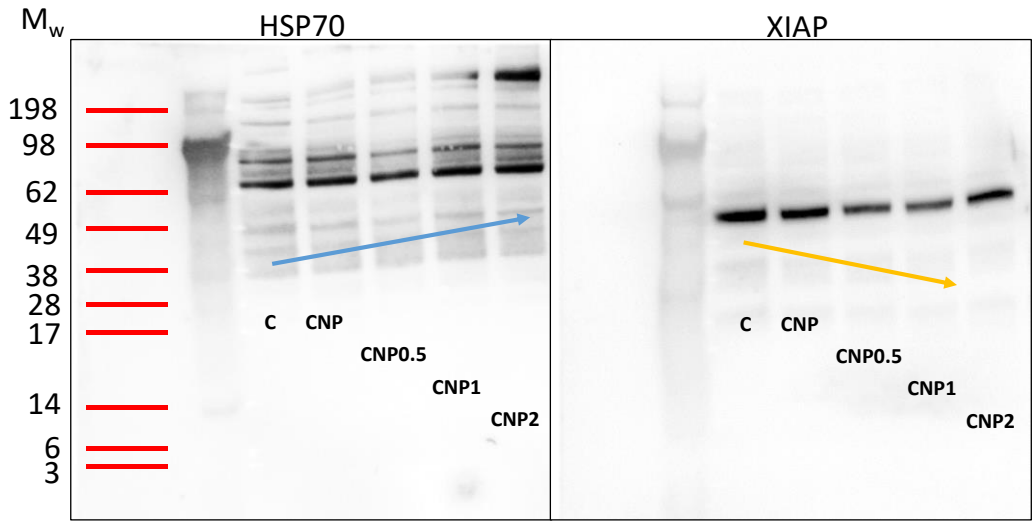

C: U87-MG cells only
CNP: U87-MG cells + Nanoparticles
CNP0.5: U87-MG cells + Nanoparticles + 0.5 min treatment
CNP1: U87-MG cells + Nanoparticles + 1 min treatment
CNP2: U87-MG cells + Nanoparticles + 2 min treatment

Figure 70: Peroxidase probed gels for the detection of proteins. From left to right are molecular weight ladder, cells (C), cells with NPs (CNP), cells with NPs treated with 0.3 W/cm^2 808 nm laser for 0.5-min (CNP0.5), 1-min (CNP1) and 2-min (CNP2).

4.4 Conclusion

Testing well above other cell viability tests on ferrite NPs published to date, the produced NPs show no signs of cytotoxicity up to 500 μg_{Fe+Zn}/ml and a viability of 80% at 1500 μg_{Fe+Zn}/ml based on metabolic activity. Similar results were obtained when assessing membrane integrity while the clonogenicity of cells is not affected by the NPs at all concentrations tested. These biocompatible-proven NPs show augmented performance compared to currently investigated iron oxide NPs in photothermia, a recent alternative cancer thermotherapy using magnetic NPs achieving total cell death in a short time. Besides, PTT is compared in-depth with the more typical MFH thermotherapeutic modality, resulting in an impressive enhanced potential. Live cells experiments using PTT show that inadequate treatment time induces signs of stress and damage to the cells although able to recover and proliferate given enough time. ROS production and Caspase-3 activation is observed for all treatment times. Initiation of the apoptotic transduction pathway is observed

at short treatment times between 0.5- and 1-min with necrosis suspected at 2-min or longer treatment times. Having shown *in vitro* biocompatibility and effectiveness in inducing cell death their biodistribution profile must be determined for further development.

5 Labelling of Citrated $Zn_{0.4}Fe_{2.6}O_4$ Nanoparticles with Radioactive Isotopes of Gallium for Real-Time Tracking *in Vivo.*

5.1 Introduction

The biodistribution profile of medicines is dependent on the physicochemical properties of a substance[139]. Depending on parameters such as size, charge and method of administration, materials may be excreted fast or exhibit prolonged circulation, may be more toxic or might accumulate in specific organs. Such examples include materials of less than 5 nm which are quickly excreted by renal clearance[140]. Above this size threshold, liver is the main organ of metabolising such materials. Comparing the charge of materials, positively charged materials cause haemolysis[141] when administered IV while neutral charges can avoid detection by the MPS[142] which is responsible for removing foreign bodies from circulation. Materials of less than 100 nm can accumulate in vascularised neoplasms as explained in section 1.2. It is thus important to evaluate the biodistribution profile of new medicines to confirm that the intended action occurs.

Traditionally, such studies occur by administering a medicine to animals which are then sacrificed at different time points, have their organs harvested and analysed for the drug. This can give a distribution profile *post-hoc*, requires many animals and it is laborious. In the interest of the 3Rs framework of the National Centre for Replacement, Refinement and Reduction of Animals in Research (NC3Rs) organisation[143] nuclear medicine imaging techniques were employed to obtain real-time tracking of NPs significantly reducing the number of animals sacrificed.

5.1.1 Nuclear Decay

Unstable nuclei lose energy in the form of radiation known as radioactivity. The emitted radiation is classified as α, β, or γ depending on whether the emitted particle is a helium nucleus, an electron or a photon as shown in Figure 71. Unintended exposure to radioactivity can be dangerous to human health. Controlled dosing though can be exploited in medicine, a subspecialty known as nuclear medicine.

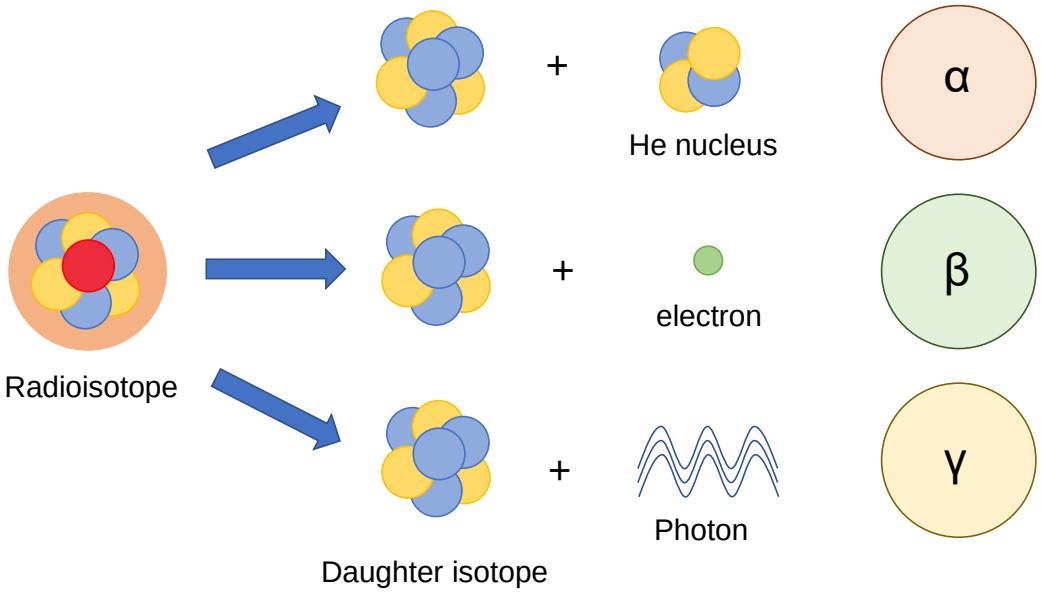

Figure 71: Radioactive decay of an unstable nucleus via α, β, and γ emission.

5.1.2 Nuclear Medicine

Nuclear medicine is a specialty of medicine which makes use of radioactive substances, or radiopharmaceuticals, to image and treat disease. Its focus is not in anatomic imaging rather it is about physiological function. Common nuclear medicine imaging techniques are single photon emission computed tomography (SPECT) or positron emission tomography (PET). Their use involves 2D and 3D imaging and are used to detect hyperthyroidism with ^{123}I, haemangioma detection with ^{99m}Tc even cancer detection, staging and follow-up with fludeoxyglucose with ^{18}F. To this end, nuclear medicine imaging techniques have been applied to monitor the biodistribution profile of NPs.

5.2 Materials and Methods

5.2.1 Reagents

$Fe(acac)_3$ (99%), $Zn(acac)_2.xH_2O$ (99.995% trace metals basis), TREG (ReagentPlus® 99%), 1,10-phenanthroline monohydrate (99%), hydroxylammonium hydrochloride (ReagentPlus® 99%), sodium acetate, human serum, glacial acetic acid, 37% hydrochloric acid (trace metals), ethanol (100%) and acetone (trace free) were purchased from Merck, UK. ^{67}Ga citrate injectable solution was obtained from CIS bio international,

France. PBS was purchased from Gibco, UK. Water was purified by milli-Q® integral system.

5.2.2 Experimental Methods

All radiolabelling experiments were performed at the Radiochemical Studies Laboratory of the Institute of Nuclear and Radiological Sciences and Technology, Energy and Safety at NCSR 'Demokritos'. The Radiochemical Studies Laboratory is licensed by the Greek Atomic Energy Commission (License number: A/435/4092/2017/22.03.17) for the use of radioactive sources.

Animals used for biodistribution studies were obtained from the breeding facilities of the Institute of Biosciences and Applications at NCSR 'Demokritos'. The experimental animal facility is registered according to the Greek Presidential Decree 56/2013 (Registration number: EL 25 BIO 022), in accordance to the European Directive 2010/63 which is harmonized with national legislation, on the protection of animals used for scientific purposes. All applicable national guidelines for the care and use of animals were followed. The study protocol was approved by the Department of Agriculture and Veterinary Service of the Prefecture of Athens (Protocol number: 1607/11-04-2018). The animals were housed in air-conditioned rooms under a 12 h light/dark cycle and allowed free access to food and water.

5.2.2.1 Elution of ^{68}Ga from ^{68}Ge Generator

For the elution of the generator, four solutions were prepared before the initiation of the procedure. Two hydrochloric acid solutions of 0.1 and 4 M and solutions N1 and N2 which have the following constituents:

N1
- 0.79 ml 37% trace free HCl
- 9.21 ml trace free H_2O
- Trace free acetone to 50 ml

N2
- 0.53 ml 37% trace free HCl
- 0.69 ml trace free H_2O
- Trace free acetone to 50 ml

In a designated, lead-shielded fume hood, HCl (7 ml, 0.1 M) was passed through a 0.2 µl syringe filter going directly into the generator at a slow rate. The liquid leaving the generator was passing through a resin column and all eluates were discarded. Air was passed through the line to remove all liquid. After, N1 (1 ml) was injected directly in the resin column and the eluate discarded including after passing air. The N2 was injected in the resin column but left in to soak for 5 min before passing it through. The eluent was collected in an Eppendorf tube. HCl (1 ml, 4 M) and air were passed through the resin column to wash it. The ^{68}Ga content was determined using specific activity measurements (Capintec, CRC-15R, USA).

5.2.2.2 Radioactive Labelling of $Zn_{0.4}Fe_{2.6}O_4$ Nanoparticles

The citrate coated NPs have many free carboxylate functional groups. Gallium has high affinity for carboxylate (COO^-) groups[144]. Laboratory generators exist to produce $^{68}GaCl_3$ as needed. ^{68}Ga was used for establishing an efficient labelling procedure due to its short half-life of 68 min which makes it safer to handle but also its abundance having a generator in-house. These conjugates were consequently used for acute biodistribution monitoring by PET. ^{67}Ga citrate was used to label NPs for longer term monitoring due to its longer half-life of 3.3 days monitored by SPECT.

Attachment of ^{68}Ga on Carboxylated Nanoparticles. The reaction of ^{68}Ga and citrated NPs was performed in a sodium acetate buffer. For the preparation of 50 ml buffer, sodium acetate trihydrate (0.245 g), water (25 ml), glacial acetic acid (469.5 µl) and 96% ethanol (5 ml) were mixed until homogenous and topped up with water. All reagents were of trace free purity. The NPs were diluted in sodium acetate buffer and ^{68}Ga solution was then added. The solution was heated on a lead-shielded heating block. The conjugation reaction was tested at different temperatures, NPs concentration and ^{68}Ga amount to increase the radiochemical yield (RcY). The product was purified by acetone precipitation, magnetic decantation and water washes until a stable suspension was obtained with high radiochemical purity (RcP). The reaction temperature was varied between 25-90 °C.

Attachment of ^{67}Ga on Carboxylated Nanoparticles. $^{67}GaCl_3$ would easily adopt to the procedure developed with $^{68}GaCl_3$. Unfortunately, its price was prohibiting, and hence alternative compounds had to be used. For this purpose, the commercially available formulation used in the clinic for SPECT imaging was used.

Determination of Radiochemical Yield. RcY refers to the percentage of attachment of the isotope vs the percentage of isotope in solution. To determine the radiochemical yield, a suitable stationary phase and conditions were determined to run radio thin layer chromatography (radio-TLC). The stationary phase was measured on a radio-TLC detector (Scan-RAM, LabLogic, UK).

Stability Studies. To assess the stability of the $^{67/68}$Ga-labelled NPs, 10 µl of a dilute suspension was added in 90 µl of water, PBS, and human serum at 37 °C. At pre-determined time points, radio-TLC or γ-counter (Packard, Cobra II, USA) were used to assess the percentage of free Ga (^{68}Ga and ^{67}Ga respectively) vs the conjugated Ga onto the NPs.

5.2.2.3 Ectopic Tumour Xenograft

U87-MG cells were cultured according to the method described in section 4.2.2.1. 1 million cells were subcutaneously injected under the front right arm (looking at mice from below) of adult severe combined immunodeficient (SCID) BALB/c mice. After approximately two weeks when the tumour has grown sufficiently the mice were used for biodistribution studies.

5.2.2.4 Administration of $^{67/68}$Ga Labelled $Zn_{0.4}Fe_{2.6}O_4$ Nanoparticles to Mice

Intravenous Administration. For IV administration, Ga-labelled NPs were injected through the orbital sinus on anaesthetised mice. Retroorbital (RO) administration was solely performed by a competent person to prevent eye injury.

Intranasal Administration. Intranasal (IN) administration was performed by casting drops of the Ga-labelled suspension on to the nostrils of mice (inverted position) and allowed to be inhaled naturally. Appropriate caution was taken to prevent drowning.

5.2.2.5 Nuclear Imaging

SPECT-CT. For SPECT-CT imaging, the mouse was placed on a heating pad and anaesthetised with isoflurane. After, the radiolabelled NPs were administered (150 µl, 20 MBq), the mouse was placed on the bed of the scanners (γ-cube and x-cube, Molecubes, Belgium) with continuous flow of isoflurane. For SPECT, a whole-body spiral acquisition of 30-60 min was carried out. The noise was removed, and a 1.6 Gauss smoothing filter was applied. MLEM reconstruction assumed 250 µm voxel size and 500 iterations using all energy peaks. For CT, a whole-body spiral acquisition at 50 kV was obtained. ISRA reconstruction with a 100 µm voxel size was applied.

Static and Dynamic PET. For PET measurements, the mouse was placed on a heating pad and anaesthetised with isoflurane. After the radiolabelled NPs were administered (50-100 µl, 1-3 MBq) the mouse was placed on the bed of the scanner (β-eye, BIOEMTECH, Greece). The whole-body planar acquisitions were collected in static and dynamic modes between 10-20 min scans. The PET heads were 6 cm apart and the energy window was 350-700 keV. Digital images were also obtained from the same instrument. Dynamic PET (dPET) is a series of images accumulated to produce a video of the radiopharmaceutical circulating in the body. Movies of dPET lasting for 2 min every 15 min were acquired for the first hour.

5.3 Results and Discussion

5.3.1 Monitoring of Radiolabelling by Radio-Thin Layer Chromatography

For the purpose of process development for efficient radiolabelling radio-TLC was used to determine the level of conjugated vs free ^{68}Ga, the principle is illustrated in Figure 72A. Different materials were employed to determine the most appropriate stationary phase, which needs to be experimentally determined for each material. For the effective separation of free $^{68}Ga^{3+}$, citric acid has been previously determined as a suitable mobile phase. After thorough testing, it was concluded that casting of NPs suspension on alumina and drying it at 60 °C for 5 min was adequate for effective separation of conjugated and free ^{68}Ga as shown in Figure 72B and C.

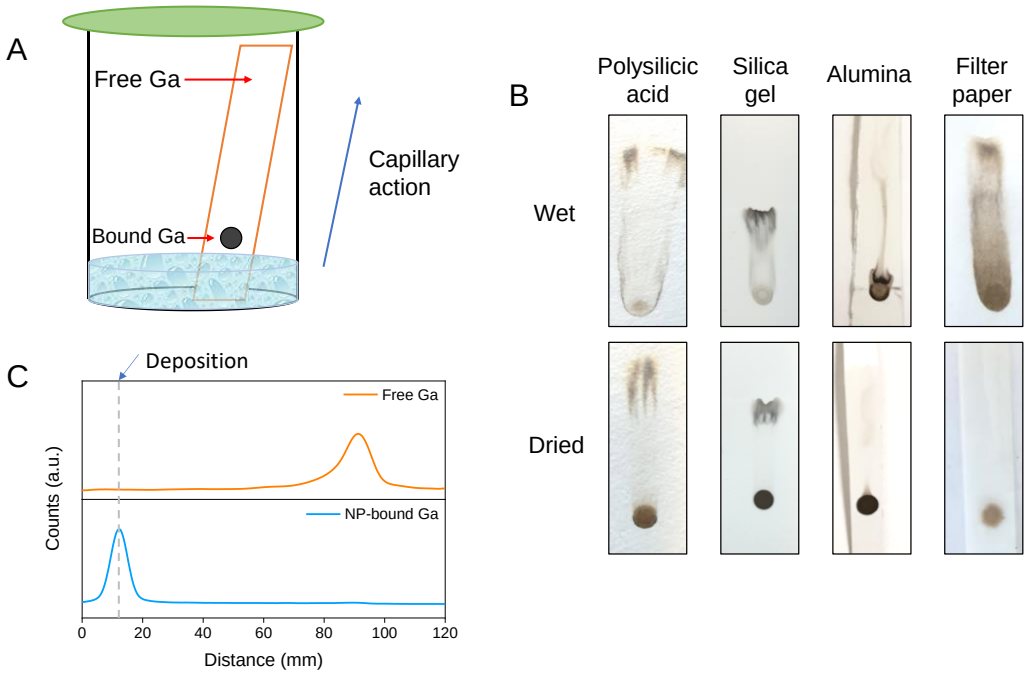

Figure 72: A) Schematic of the TLC set up. B) Various stationary phases used in separating free from bound ^{68}Ga on the NP surface right after drop casting (wet) and after drying for 5 min at 60 °C (dried). C) Radio-TLC result for bound and free ^{68}Ga.

Method Optimisation. Process development was done using ^{68}Ga which is easier to handle due to its short half-life. The procedure described in section 5.2.2.2 was used as a baseline for method optimisation. The temperature and time of the reaction as well as the ^{68}Ga% were varied and the RcY was assessed by radio-TLC. As shown in Figure 73, temperature had a huge effect on the RcY which at high enough temperatures reaches a plateau when no more ^{68}Ga can be conjugated on the NPs. Since the half-life of ^{68}Ga is short, the least amount of time resulting in the highest RcY was chosen at 30 min. In addition, the amount of ^{68}Ga present in the reaction mixture also affected the RcY with more ^{68}Ga resulting in a higher RcY. In combination, the optimum parameters were determined as 30 min at 90 °C with 33% ^{68}Ga content. The fact that more ^{68}Ga yields a higher RcY indicates that there are available carboxylate groups for attachment and the limiting factor is ^{68}Ga content, only limited by the concentration eluted from the generator. Kinetic factors are overcome by increasing the reaction temperature whilst it seems thermodynamic reasons do not allow for 100% RcY probably due to an established equilibrium which shifts according to ^{68}Ga% content.

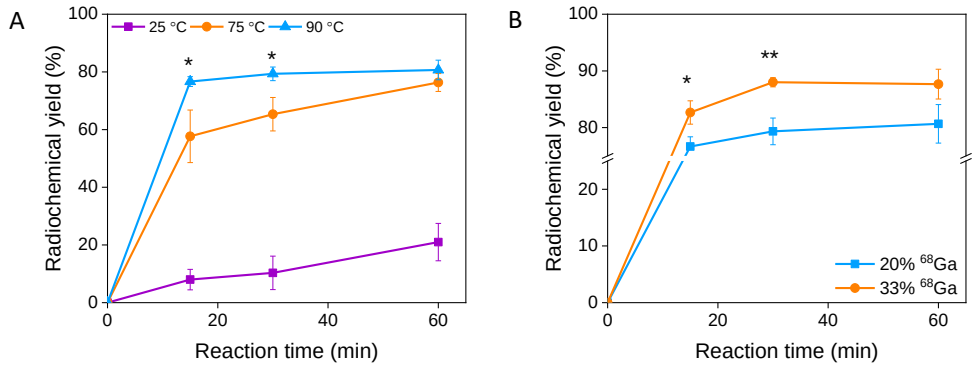

Figure 73: RcY as a function of A) reaction temperature and time and B) ^{68}Ga% and time (n = 3). Values reported as mean ± SEM. p-Values were calculated based on a two-tailed t-test: ** indicates p<0.01 and * indicates p<0.05.

The ferrofluid properties were reversibly lost during radiolabelling. To eliminate free ^{68}Ga and resuspend the NPs as a ferrofluid, water washes with magnetic decantation were performed until the pH reached 7. When the pH was neutral, an acetone precipitation, magnetic decantation and resuspension in water produced the initial consistency of ferrofluid. The washing procedure was effectively removing free ^{68}Ga with radiochemical purity (RcP) reaching 95% as shown in Figure 74.

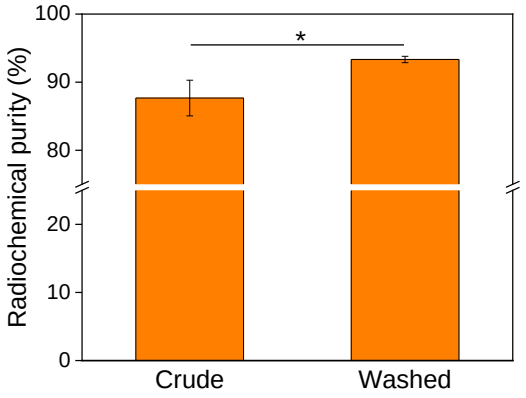

Figure 74: RcP of crude and washed ^{68}Ga-labelled $Zn_{0.4}Fe_{2.6}O_4$ NPs (n = 3). Values reported as mean ± SEM. p-Values were calculated based on a two-tailed t-test: * indicates p<0.05.

Conjugate Stability. The stability of the conjugate was assessed in water, PBS and human serum as described in section 5.2.2.2. The ^{68}Ga remained

attached to the NPs after washing and resists dilution (1:10). In PBS and human serum, ^{68}Ga showed a burst release of about 15% and then stabilised. The results are summarised in Figure 57. This is probably due to phosphates and macrocycles present in PBS and human serum respectively which would form a more stable complex with Ga compared to carboxylates[145].

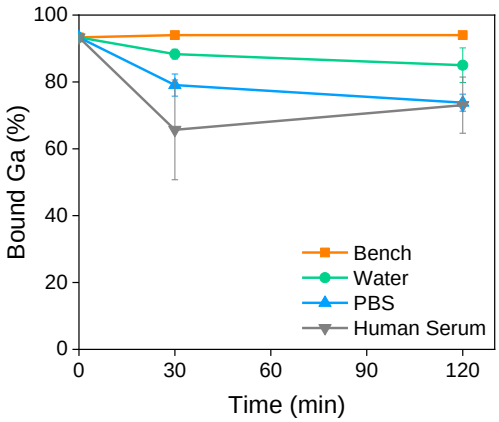

Figure 75: Stability of ^{68}Ga conjugated onto the surface of $Zn_{0.4}Fe_{2.6}O_4$ NPs upon dilution, phosphate buffer and human serum (n = 3). Values reported as mean ± SD.

5.3.2 Routes of Administration

Many NPs require a post-synthesis treatment to change the coating acquired during the synthesis with a more biocompatible or functional coating. Examples include biocompatible polymers[146], smart polymers[46], inorganic polymers[97], small molecules[147], peptides[122] and others. The primary goal is to control the stability of the NPs through electrosteric stabilisation in suspension and subsequently control their fate *in vivo*[148,149]. Coating of NPs should be carefully designed depending on the intended use, target, and route of administration. Oral administration involves acidic conditions of the stomach, neutralisation in the intestines and the opening of tight junctions for absorption from the intestines to systemic circulation[150]. IN administration requires prolonged residence in the nasal cavity for absorption to the trigeminal nerve or lymphatic system[151]. IV administration directly delivers a drug in the complex environment of blood where proteins tag foreign bodies for clearance in a process called opsonisation[54]. Additionally, liver and kidneys are constantly filtrating the blood to maintain a healthy environment.

In the case of MFH, the amount required to reach the tumour for an efficient treatment is not currently reached through IV administration while oral and IN routes are under-exploited. To by-pass this problem, scientists rely on intratumoural injections to reach the high doses of NPs required at the site of interest[152]. This method of administration is not currently used in clinical practice and carries high risk of metastasis through trauma hence it is not considered ideal for clinical translation. Given the alternative PTT treatment which is much more efficient in terms of the amount required to elevate the temperature to the same degree, IV and IN administration were performed and the amount of NPs reaching organs of interest was measured.

5.3.2.1 Intravenous Administration

The blood is a complex environment with many molecules and cells. Vitamins, hormones, proteins, erythrocytes, leukocytes, antibodies and platelets are some of the circulating bodies in it. Its function is to deliver nutrients and oxygen to tissues and remove metabolic waste outside the human body. It is a highly regulated component of the body, with a tight tolerable pH range and any imbalance can cause disease. Consequently, beyond the homeostatic mechanisms regulating blood composition, blood is guarded against foreign bodies such as viruses, bacteria, or NPs. Circulating proteins adsorb on the NPs tagging it for clearance[153]. The MPS recognises these proteins and remove the foreign body from circulation. To this end, polyethylene glycol (PEG) have shown the ability to reduce opsonisation and allow for longer circulation times[154]. Bi-functional PEG needed for the conjugation of biomolecules and electrostatic stability are expensive and require skilful chemistry. Other considerations for IV administration include, charge and charge density[155,156], the target cell population[156,157] as well as shape[32,157,158] and size[88,155,158] of NPs. Charge affects cellular uptake; the cell membrane of most cells carries a negative charge due to the terminal sialic acid of the glycocalyx and phospholipids in the membrane bilayer[159]. According to Coulomb's law, opposite charges attract each other and therefore a positively charged particle would be attracted to the cell membrane leading to enhanced uptake[17]. On the contrary, there would be an energetic barrier between a negatively charged particle and a negatively charged cell surface.

Nevertheless, positive charges are not considered optimal for biological applications because they seem to be more cytotoxic than negatively charged particles of similar size[156] due to higher interaction with plasma membrane causing haemolysis[141]. An example of how different types of cells affect the cytotoxicity results is the phagocytic cells which preferentially interact with anionic particles and shown to be more cytotoxic than cationic NPs[156] while non-phagocytic cells show higher cytotoxicity with positively charged particles[156]. In all cases, size and shape are important factors and, in some experiments, were shown to play a bigger role than charge[156]. The importance of a carefully selected coating is then apparent as it serves many purposes; stabilising the particles in the biological environment but also ensure they interact with what were initially designed to.

Many elaborate coatings have been attached to magnetic NPs and tested *in vivo* although few, if any, succeeded in delivering the required amount to the tumour for effective MFH. Given the enhanced performance of PTT against MFH and the manifold less material needed to increase the temperature to the same degree, the negatively charged and biocompatible molecule, citrate was evaluated as it is biocompatible and to serve as a baseline for future work.

IV administration via the tail vain proved to be problematic. SCID mice have a smaller size than physiological mice and their vessels are easy to brake resulting in thrombosis. Consequently, a series of unsuccessful attempts going upwards the tail vein were causing unnecessary stress and suffering to the animal. As a cumulative result, a larger number of mice would have to be used as many would be rendered unusable after having their tails thrombosed. It was then considered necessary to find another IV route and as such the orbital sinus seemed a reasonable alternative. The orbital sinus takes a lot of skill to do successfully and safely to prevent damage to the eye and for this reason an experienced animal handler performed these administrations. The orbital sinus is underexploited due to the dangers posed to the eyes of the mice. With careful technique, this can prove an efficient IV route reducing the number of animals used. Although the chances of clinical translation of retroorbital administration are practically zero, herein it was used purely as an IV method since studies have shown that IV administration through the tail vein and the

orbital sinus are equal for all biodistribution concerns[160]. The acute biodistribution was monitored with dynamic PET (dPET) for the first 20 min post-administration. Static PET scans were performed at 1, 2 and 3 h post-administration before the activity of ^{68}Ga diminished. As shown in Figure 76, PET scans of mice indicate accumulation to the area of liver and spleen post retro-orbital administration. This is in accordance with administration of highly charged NPs which strongly interact with opsonins leading to their accumulation in the clearance organs.

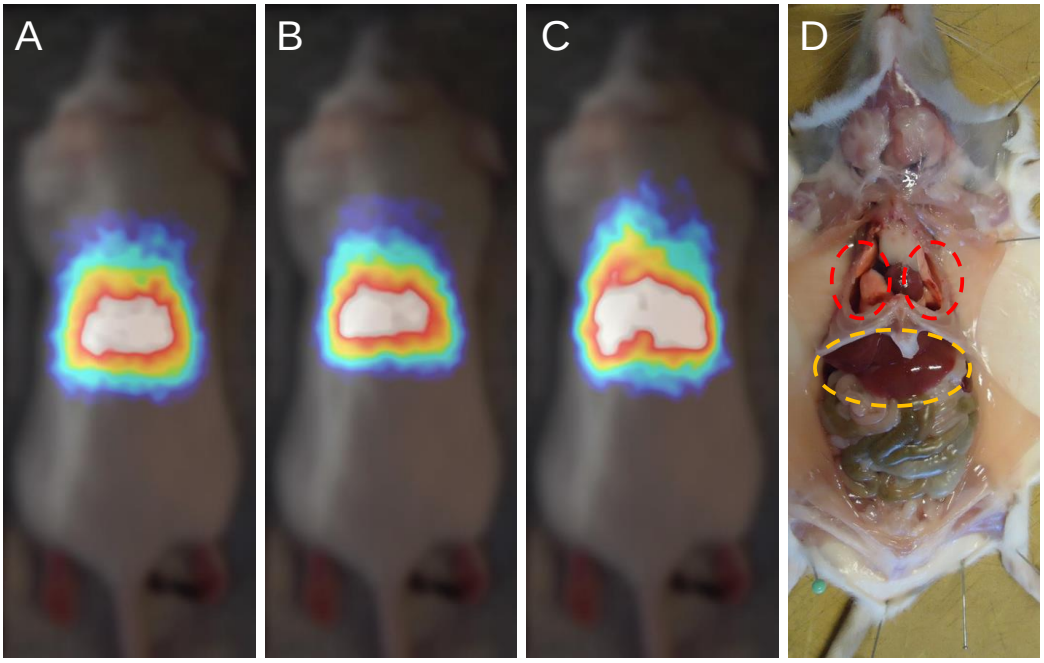

Figure 76: A), B) and C) Static PET scans co-registered with digital images of SCID BALB/c mice retro-orbitally administered with ^{68}Ga-labelled $Zn_{0.4}Fe_{2.6}O_4$ NPs, 1, 2 and 3 h post-administration respectively. D) Digital image of a dissected mouse with lungs and liver indicated in red and yellow ovals, respectively.

A similar pattern has been observed after 24 h of administration as shown in SPECT-CT images in Figure 77.

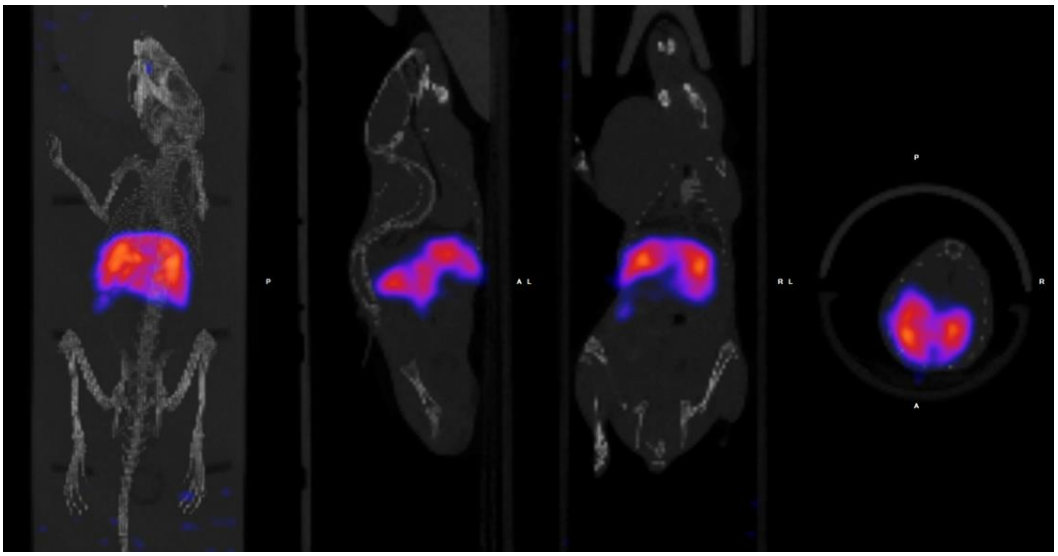

Figure 77: SPECT-CT scan of mouse 24 h post retro-orbital administration of ^{67}Ga-labelled $Zn_{0.4}Fe_{2.6}O_4$ NPs.

5.3.2.2 Intranasal Administration

Recently, the IN route has been exploited for vaccines[151,161] and direct delivery of medicines[162,163] to the brain by-passing the blood brain barrier (BBB) which is a significant obstacle for delivering drugs to the brain[164]. The role of the BBB is neuroprotective as it regulates which molecules go in and out of the brain as well as blocking viruses and bacteria. It also blocks approximately 100% of large molecule neurotherapeutics and antibodies[164]. Therefore, there is a great potential for nanotechnology to aid in the delivery of molecules to the brain. The trigeminal nerve connects areas such as the eye, the nose and mouth with the brain as illustrated in Figure 78[165].

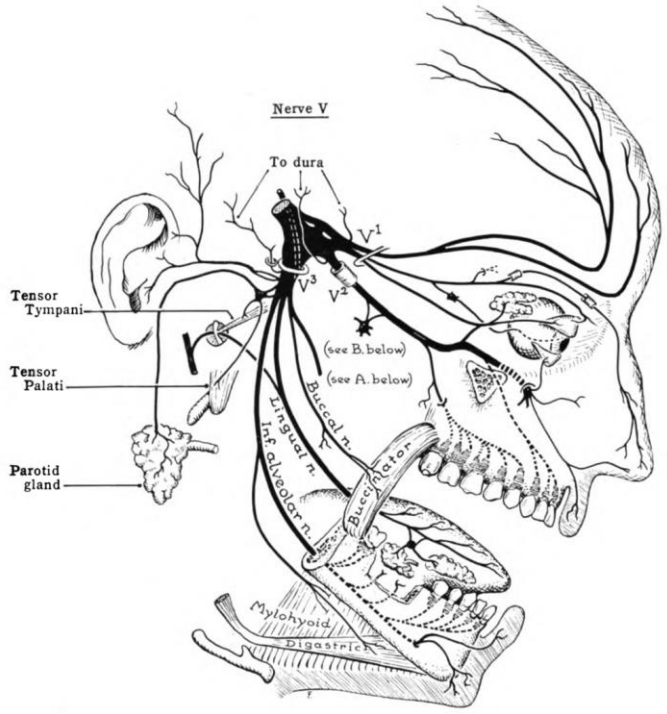

Figure 78: Illustration of the distribution of the trigeminal nerve.

Physiology of the Intranasal Cavity. To achieve sufficient delivery of substances from the nasal cavity to the trigeminal and olfactory nerves, the physiology of the area needs to be taken into consideration to determine what properties can be exploited to enhance this effect. The respiratory segment of the nasal cavity, specifically the septum, hosts the nasopalatine nerve (part of the trigeminal nerve) while at the olfactory segment of the nose the olfactory region hosts the olfactory nerve. The upper respiratory system is covered with a ciliated pseudostratified columnar epithelium which acts as a protective barrier[166]. The mucus-excreting goblet cells produce mucus to trap pathogens and foreign particles while the ciliated cells are responsible for mucociliary clearance[166]. Since cells have a negative charge on their surface due to the glycocalyx a positive charge would increase the residence time of particles in the cavity increasing the potential for passive transfer of NPs to the nerves[166]. Another strategy of entering the submucosal layer is the use of penetration enhancers which ideally reversibly open the intercellular junctions between the epithelial cells allowing the paracellular transport of materials to the sub-mucosa[167]. In addition to the paracellular transport pathway, the transcellular pathway carries larger materials through the cells via non-specific or receptor-

mediated endocytosis[168]. The methods of transport across the mucosa are illustrated in Figure 79.

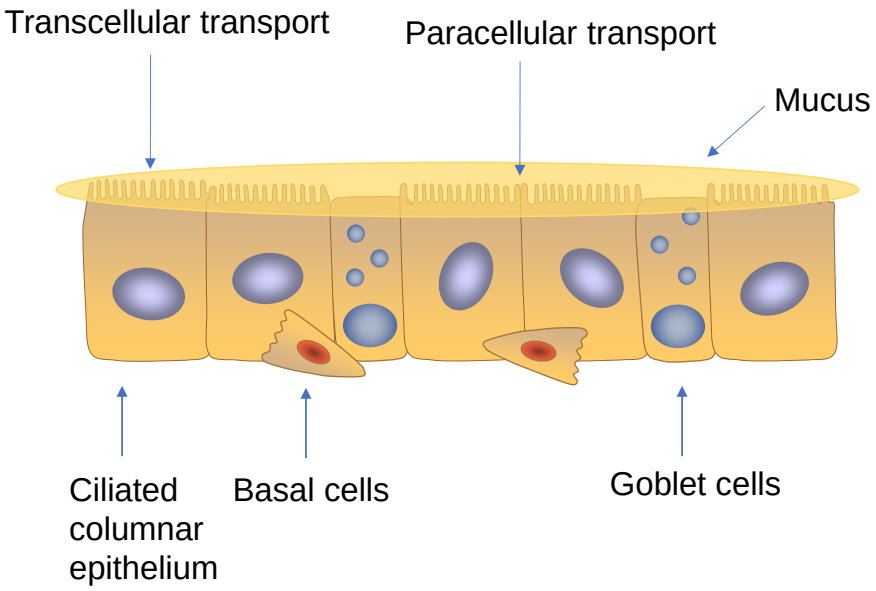

Figure 79: Illustration of the IN mucosa and epithelium.

Since the positive charge of various polymers used in IN delivery was shown not to be the only factor in successfully exploiting the IN cavity[168], the negatively charged citrated $Zn_{0.4}Fe_{2.6}O_4$ NPs were used for IN delivery for comparison of their biodistribution profile against the same NPs administered IV to deliver NPs to the brain. This would serve as a reference biodistribution for any future work to achieve higher amounts reaching the brain via the IN route.

To compare the biodistribution profile via the two administration routes, ^{68}Ga-labelled $Zn_{0.4}Fe_{2.6}O_4$ NPs have been administered (50-200 µl for IV, 20 µl for IN) and mice were sacrificed after 2 h. The biodistribution profiles for both routes are shown in Figure 80.

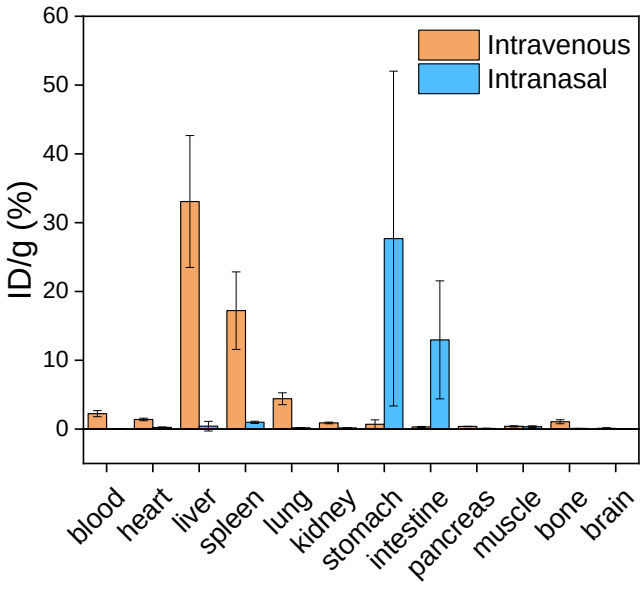

Figure 80: Biodistribution at 2 h of ^{68}Ga-labelled $Zn_{0.4}Fe_{2.6}O_4$ NPs after retroorbital and intranasal administrations (n = 4). Values reported as mean ± SD.

The distribution vastly differs between IV and IN administrations. IV shows accumulation in the liver, spleen, and lungs while IN administration shows mainly stomach and intestines. The percentage reaching the tumour with either technique is around 0.1%. Given that the concentration of the NPs was 30 mg_{Fe+Zn}/ml this means the actual mass of NPs reaching the brain would not be suffice for either PTT or MFH. Even though time was shown to increase the tumour accumulation monitored over 72 h reaching more than 0.5% (Figure 81) this route surely needs further work such as introducing a positive charge to increase residence time in the septum or exploit the use of penetration enhancers. One suggestion would be a chitosan based polymer which offers biocompatibility, water solubility, control over the methylation and consequently the amount of positive charge it will carry and tentative evidence in scientific literature of its ability to cross the nasal mucosa[151,162,169].

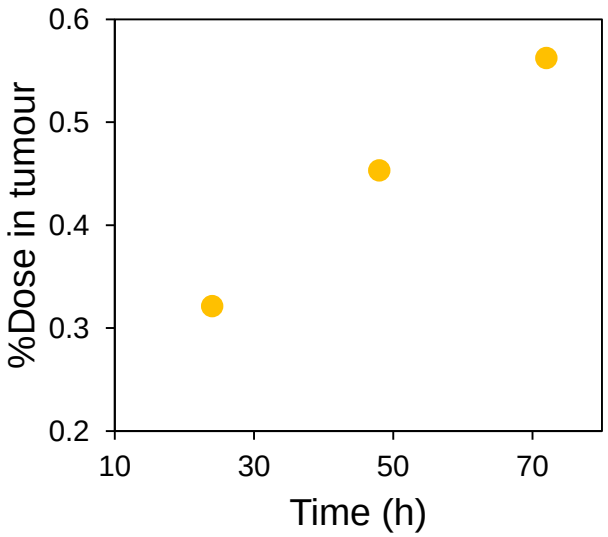

Figure 81: Time dependence of %dose of administered NPs reaching the tumour xenograft (n = 1).

5.4 Conclusion

Citrated $Zn_{0.4}Fe_{2.6}O_4$ NPs were successfully radiolabelled with ^{68}Ga and ^{67}Ga. Method optimisation took in account the reaction time, temperature, and amount of Ga to yield NPs with up to 95% RcP. These NPs were administered in physiological mice via the IV and IN routes and their distribution was monitored by PET, SPECT-CT and γ-counter. NPs mainly accumulate in the liver and spleen after IV administration while NPs accumulate mainly in the stomach and intestines after IN administration. There was a time-dependent increase in accumulation in the tumour up to 72 h reaching up to 0.5% of the administered dose. NPs administered with either method were well tolerated with no adverse events observed in any of the animals. The results suggest that further work needs to be done to achieve successful IN delivery of NPs to the brain.

6 Conclusion – Future Work

Highly performing anisotropic nanomaterials have been proven difficult to prepare. The crystal habit of ferrites renders their direct synthesis challenging. Many of the reported protocols for such syntheses require special conditions regulating pressure and temperature to remove residual water and gases from raw materials prior to experimenting, introducing variability among batches. Studying individual steps of their synthetic protocols in greater detail did reveal further information but unfortunately to no avail. The preparation of anisotropic NPs of different composition than the desired, such as iron oxide-hydroxides which are better suited for anisotropic growth was also investigated. Such NPs were used as an intermediate which would then be converted to iron oxide by reduction as previously shown to occur by Mohapatra et al.[56] The procedures followed and those developed, successfully convert the material to iron oxide although fail to retain a uniform anisotropic shape and superparamagnetic nature. This is the case with others that attempted to do such a conversion who to do so introduce inorganic coatings on the material prior to reduction to limit the space ions can move about.[170,171,70] The inability to consistently produce NPs with certain specifications hindered their further development and a different approach was therefore taken.

Although ferrite nanomaterials, especially those with spherical geometry, have been known for some time, it is evidenced from this work that they can still be perfected through careful exploitation of their chemistry. Use of pressure during synthesis was shown to produce materials outperforming previous members of its class. The crystals made were of higher quality in terms of lattice strain which consequently translates to better magnetic properties, a property onto which many applications of magnetic NPs rely on such as medical imaging and drug delivery. In addition, the introduction of Zn^{2+} ions in the crystal lattice further augmented their magnetic properties and extended the retention of their magnetic properties in time by replacing oxidizable Fe^{2+} ions with redox inactive Zn^{2+}. Digestive ripening, a procedure never used in ferrite NPs, was adopted to successfully reduce the polydispersity of the NPs from 24.7% to 9.4% entering the hall of high-quality nanomaterials.

The potential of Zn-doped ferrite NPs was assessed in the current topic of magnetic hyperthermia. The modality has received approval from the European union for brain malignancies and is currently under clinical assessment for other types of cancers by MagForce AG. Magnetothermal performance was shown to be typical of superparamagnetic NPs which is underwhelming for effective clinical use. A novel approach to induce heat using magnetic NPs is the exploitation of their semiconducting properties used to convert light into heat upon the application of a laser. This method is conventionally encountered with noble-metal NPs with exceptional performance[77,172] but was shown to work equally well with the Zn-doped NPs prepared. An inverse relationship to dose was shown which itself is a great obstacle in the translation of many superparamagnetic NPs to clinical agents for magnetic hyperthermia treatment. Also, Zn-doped NPs out-performed iron oxide NPs due to better-suited properties for photothermal conversion achieving complete cell death within clinically acceptable settings at short treatment times of 10 min or less.

Citrate molecules grafted on the surface of the NPs allowed for the preparation of a magnetic ferrofluid with good colloidal stability in biologically mimicking conditions. This allowed for further evaluation of their potential toxicity *in vitro*. The biocompatibility of the NPs was shown to be excellent with various assays such as MTT, LDH and clonogenic assays. Brain glioblastoma cells seemed unaffected up to 200 µg/ml in terms of their metabolic functions and membrane integrity. Furthermore, the clonogenicity of the cells was not affected which translates into a healthy cell population in the absence of long-term genetic changes.

The biodistribution profile of the NPs was assessed *in vivo* by radiolabelling the NPs and monitoring the circulation of NPs in real-time using SPECT-CT and PET. Procedures for radiolabelling efficiency and purity were developed to attach Ga isotopes to free carboxylate groups of the citrate coating of the NPs exceeding 90% labelling. The NPs were administered intravenously and intranasally and their biodistribution was monitored by PET and SPECT-CT imaging and verified by a γ-counter. The studies performed indicate that although citrate grafting confers great colloidal stability the aim of non-

invasively delivering the NPs to the brain cannot be effectively achieved with less than 1% of the administered dose reaching the brain after 72 h whilst the majority of the administered dose is accumulated in the clearance organs, the liver and kidneys.

There is potential for technological advancements through nanotechnology. The future of NPs seems bright with potential applications in clinical practice, laboratory instrumentation and methods and electronics just to name a few. Magnetic NPs have just made it through to clinical and certain laboratory applications. The scope of this work revolved around clinical applications and therefore the lack of approval from FDA and EMA for any zinc ferrite material to date is concerning. Based on overwhelming evidence that zinc ferrites outperform currently investigated iron oxide NPs and appear as biocompatible as iron oxides should provide enough incentive for material scientists to investigate these materials further hopefully obtaining approval. In addition to a highly-performing magnetic core there is an urgent need to successfully develop an appropriate coating for such NPs to achieve adequate colloidal stability, deliver the NPs to their intended location and of course exhibit low toxicity. To this end, an interdisciplinary approach from material scientists, polymer chemists, biologists and physicians is necessary to strike a balance towards a functioning product.

7 References

(1) van der Zee, J. Heating the Patient: A Promising Approach? *Ann. Oncol.* **2002**, *13* (8), 1173–1184. https://doi.org/10.1093/annonc/mdf280.

(2) Thanh, N. T. K. *Magnetic Nanoparticles From Fabrication to Clinical Applications*; CRC press, 2012.

(3) Horsman, M. R.; Overgaard, J. Hyperthermia: A Potent Enhancer of Radiotherapy. *Clin. Oncol.* **2007**, *19* (6), 418–426. https://doi.org/10.1016/j.clon.2007.03.015.

(4) Luo, S.; Wang, L. F.; Ding, W. J.; Wang, H.; Zhou, J. M.; Jin, H. K.; Su, S. F.; Ouyang, W. W. Critical Review Clinical Trials of Magnetic Induction Hyperthermia for Treatment of Tumours. *OA Cancer* **2014**, *1* (2), 1–6.

(5) Espinosa, A.; Di Corato, R.; Kolosnjaj-Tabi, J.; Flaud, P.; Pellegrino, T.; Wilhelm, C. Duality of Iron Oxide Nanoparticles in Cancer Therapy: Amplification of Heating Efficiency by Magnetic Hyperthermia and Photothermal Bimodal Treatment. *ACS Nano* **2016**, *10* (2), 2436–2446. https://doi.org/10.1021/acsnano.5b07249.

(6) Shen, S.; Wang, S.; Zheng, R.; Zhu, X.; Jiang, X.; Fu, D.; Yang, W. Magnetic Nanoparticle Clusters for Photothermal Therapy with Near-Infrared Irradiation. *Biomaterials* **2015**, *39*, 67–74. https://doi.org/10.1016/j.biomaterials.2014.10.064.

(7) Chen, J.; Glaus, C.; Laforest, R.; Zhang, Q.; Yang, M.; Gidding, M.; Welch, M. J.; Xia, Y. Gold Nanocages as Photothermal Transducers for Cancer Treatment. *Small* **2010**, *6* (7), 811–817. https://doi.org/10.1002/smll.200902216.

(8) Alkilany, A. M.; Thompson, L. B.; Boulos, S. P.; Sisco, P. N.; Murphy, C. J. Gold Nanorods: Their Potential for Photothermal Therapeutics and Drug Delivery, Tempered by the Complexity of Their Biological Interactions. *Adv. Drug Deliv. Rev.* **2012**, *64* (2), 190–199. https://doi.org/10.1016/j.addr.2011.03.005.

(9) MagForce AG The Nanomedicine Company https://www.magforce.com/en/home/ (accessed Apr 15, 2020).

(10) Karponis, D.; Azzawi, M.; Seifalian, A. An Arsenal of Magnetic Nanoparticles; Perspectives in the Treatment of Cancer. *Nanomedicine* **2016**, *11* (16), 2215–2232. https://doi.org/10.2217/nnm-2016-0113.

(11) Jaque, D.; Martínez Maestro, L.; del Rosal, B.; Haro-Gonzalez, P.; Benayas, A.; Plaza, J. L.; Martín Rodríguez, E.; García Solé, J. Nanoparticles for Photothermal Therapies. *Nanoscale* **2014**, *6* (16), 9494–9530. https://doi.org/10.1039/c4nr00708e.

(12) Lee, H.; Shin, T.-H.; Cheon, J.; Weissleder, R. Recent Developments in Magnetic Diagnostic Systems. *Chem. Rev.* **2015**, 150810120525005. https://doi.org/10.1021/cr500698d.

(13) Llandro, J.; Palfreyman, J. J.; Ionescu, a.; Barnes, C. H. W. Magnetic Biosensor Technologies for Medical Applications: A Review. *Med. Biol. Eng. Comput.* **2010**, *48* (10), 977–998. https://doi.org/10.1007/s11517-010-0649-3.

(14) Fennimore, A. M.; Yuzvinsky, T. D.; Han, W. Q.; Fuhrer, M. S.; Cumings, J.; Zetti, A. Rotational Actuators Based on Carbon Nanotubes. *Nature* **2003**, *424* (6947), 408–410. https://doi.org/10.1038/nature01823.

(15) The University of Memphis, Department of Chemistry https://www.memphis.edu/chem/faculty-huang/research.php (accessed Dec 10, 2018).

(16) Kolhatkar, A.; Jamison, A.; Litvinov, D.; Willson, R.; Lee, T. *Tuning the Magnetic Properties of Nanoparticles*; 2013; Vol. 14. https://doi.org/10.3390/ijms140815977.

(17) Bertrand, N.; Wu, J.; Xu, X.; Kamaly, N.; Farokhzad, O. C. Cancer Nanotechnology: The Impact of Passive and Active Targeting in the Era of Modern Cancer Biology. *Adv. Drug Deliv. Rev.* **2014**, *66*, 2–25. https://doi.org/10.1016/j.addr.2013.11.009.

(18) Prager, G. W.; Zielinski, C. C. Angiogenesis in Cancer. *Biochem. Basis*

Ther. Implic. Angiogenes. **2013**, *2* (3), 335–356. https://doi.org/10.1007/978-1-4614-5857-9_18.

(19) Yuan, F.; Dellian, M.; Fukumura, D.; Leunig, M.; Berk, D. A.; Torchilin, V. P.; Jain, R. K. Vascular Permeability in a Human Tumor Xenograft: Molecular Size Dependence and Cutoff Size1. **1995**, 3752–3757.

(20) Oh, E.; Delehanty, J. B.; Sapsford, K. E.; Susumu, K.; Goswami, R.; Blanco-Canosa, J. B.; Dawson, P. E.; Granek, J.; Shoff, M.; Zhang, Q.; et al. Cellular Uptake and Fate of PEGylated Gold Nanoparticles Is Dependent on Both Cell-Penetration Peptides and Particle Size. *ACS Nano* **2011**, *5*, 6434–6448. https://doi.org/10.1021/nn201624c.

(21) Kolhar, P.; Anselmo, A. C.; Gupta, V.; Pant, K.; Prabhakarpandian, B.; Ruoslahti, E.; Mitragotri, S. Using Shape Effects to Target Antibody-Coated Nanoparticles to Lung and Brain Endothelium. *Proc. Natl. Acad. Sci.* **2013**, *110* (26), 10753–10758. https://doi.org/10.1073/pnas.1308345110.

(22) Gromnicova, R.; Davies, H. A.; Sreekanthreddy, P.; Romero, I. A.; Lund, T.; Roitt, I. M.; Phillips, J. B.; Male, D. K. Glucose-Coated Gold Nanoparticles Transfer across Human Brain Endothelium and Enter Astrocytes in Vitro. *PLoS One* **2013**, *8* (12). https://doi.org/10.1371/journal.pone.0081043.

(23) Dhar, S.; Kolishetti, N.; Lippard, S. J.; Farokhzad, O. C. Targeted Delivery of a Cisplatin Prodrug for Safer and More Effective Prostate Cancer Therapy in Vivo. *Proc Natl Acad Sci U S A* **2011**, *108* (5), 1850–1855. https://doi.org/10.1073/pnas.1011379108.

(24) Demortière, a; Panissod, P.; Pichon, B. P.; Pourroy, G.; Guillon, D.; Donnio, B.; Bégin-Colin, S. Size-Dependent Properties of Magnetic Iron Oxidenanocrystals. *Nanoscale* **2011**, *3* (1), 225–232. https://doi.org/10.1039/C0NR00521E.

(25) Wetterskog, E.; Agthe, M.; Mayence, A.; Grins, J.; Wang, D.; Rana, S.; Ahniyaz, A.; Salazar-Alvarez, G.; Bergström, L. Precise Control over Shape and Size of Iron Oxide Nanocrystals Suitable for Assembly into

Ordered Particle Arrays. *Sci. Technol. Adv. Mater.* **2014**, *15* (5), 055010. https://doi.org/10.1088/1468-6996/15/5/055010.

(26) Hugounenq, P.; Levy, M.; Alloyeau, D.; Lartigue, L.; Dubois, E.; Cabuil, V.; Ricolleau, C.; Roux, S.; Wilhelm, C.; Gazeau, F.; et al. Iron Oxide Monocrystalline Nanoflowers for Highly Efficient Magnetic Hyperthermia. *J. Phys. Chem. C* **2012**, *116* (29), 15702–15712. https://doi.org/10.1021/jp3025478.

(27) Shavel, A.; Liz-Marzán, L. M. Shape Control of Iron Oxide Nanoparticles. *Phys. Chem. Chem. Phys.* **2009**, *11*, 3762–3766. https://doi.org/10.1039/b905768d.

(28) Thanh, N. T. K.; Dung, N. T.; Tung, L. D.; Thanh, C. T.; Ong, Q. K.; Chuc, N. Van; Maenosono, S.; Lu, L. T. Synthesis of Magnetic Cobalt Ferrite Nanoparticles with Controlled Morphology, Monodispersity and Composition: The Influence of Solvent, Surfactant, Reductant and Synthetic Condition. *Nanoscale* **2015**. https://doi.org/10.1039/C5NR04266F.

(29) Noh, S. H.; Na, W.; Jang, J. T.; Lee, J. H.; Lee, E. J.; Moon, S. H.; Lim, Y.; Shin, J. S.; Cheon, J. Nanoscale Magnetism Control via Surface and Exchange Anisotropy for Optimized Ferrimagnetic Hysteresis. *Nano Lett.* **2012**, *12*, 3716–3721. https://doi.org/10.1021/nl301499u.

(30) Goodarz Naseri, M.; Saion, E. Bin; Ahangar, H. A.; Hashim, M.; Shaari, A. H. Synthesis and Characterization of Manganese Ferrite Nanoparticles by Thermal Treatment Method. *J. Magn. Magn. Mater.* **2011**, *323* (13), 1745–1749. https://doi.org/10.1016/j.jmmm.2011.01.016.

(31) Liu, C.; Zou, B.; Rondinone, A. J.; Zhang, Z. J. Chemical Control of Superparamagnetic Properties of Magnesium and Cobalt Spinel Ferrite Nanoparticles through Atomic Level Magnetic Couplings. *J. Am. Chem. Soc.* **2000**, *122* (26), 6263–6267. https://doi.org/10.1021/ja000784g.

(32) Ispas, C.; Andreescu, D.; Patel, A.; Goia, D. V.; Andreescu, S.; Wallace, K. N. Toxicity and Developmental Defects of Different Sizes and Shape

Nickel Nanoparticles in Zebrafish. *Environ. Sci. Technol.* **2009**, *43* (16), 6349–6356. https://doi.org/10.1021/es9010543.

(33) Lacroix, L. M.; Lachaize, S.; Falqui, A.; Blon, T.; Carrey, J.; Respaud, M.; Dumestre, F.; Amiens, C.; Margeat, O.; Chaudret, B.; et al. Ultrasmall Iron Nanoparticles: Effect of Size Reduction on Anisotropy and Magnetization. *J. Appl. Phys.* **2008**, *103* (7), 2006–2009. https://doi.org/10.1063/1.2837625.

(34) Lacroix, L.-M.; Huls, N. F.; Ho, D.; Sun, X.; Cheng, K.; Sun, S. Stable Single-Crystalline Body Centered Cubic Fe Nanoparticles. *Nano Lett.* **2011**, *11* (4), 1641–1645. https://doi.org/10.1021/nl200110t.

(35) Pal, S. K.; Bahadur, D. Shape Controlled Synthesis of Iron-Cobalt Alloy Magnetic Nanoparticles Using Soft Template Method. *Mater. Lett.* **2010**, *64* (10), 1127–1129. https://doi.org/10.1016/j.matlet.2010.01.086.

(36) Green, L. A. W.; Thuy, T. T.; Mott, D. M.; Maenosono, S.; Kim Thanh, N. T. Multicore Magnetic FePt Nanoparticles: Controlled Formation and Properties. *RSC Adv.* **2014**, *4* (3), 1039. https://doi.org/10.1039/c3ra44319a.

(37) Wu, H.; Qian, C.; Cao, Y.; Cao, P.; Li, W.; Zhang, X.; Wei, X. Synthesis and Magnetic Properties of Size-Controlled FeNi Alloy Nanoparticles Attached on Multiwalled Carbon Nanotubes. *J. Phys. Chem. Solids* **2010**, *71* (3), 290–295. https://doi.org/10.1016/j.jpcs.2009.12.079.

(38) Cornell, R. M.; Schwertmann, U. *The Iron Oxides: Structure, Properties, Reactions, Occurences and Uses*; Wiley-VCH: Weinheim, 2004. https://doi.org/10.1002/3527602097.ch1.

(39) Lalena, J. N.; Cleary, D. A. *Principles of Inorganic Materials Design: Second Edition*; 2010. https://doi.org/10.1002/9780470567548.

(40) Krishnan, K. M.; Pakhomov, A. B.; Bao, Y.; Blomqvist, P.; Chun, Y.; Gonzales, M.; Griffin, K.; Ji, X.; Roberts, B. K. Nanomagnetism and Spin Electronics: Materials, Microstructure and Novel Properties. *J. Mater. Sci.* **2006**, *41* (3), 793–815. https://doi.org/10.1007/s10853-006-6564-1.

(41) Thanh, T. *Magnetic Nanoparticles: From Fabrication to Clinical Applications*; CRC press, 2012.

(42) Lee, J. S.; Myung Cha, J.; Young Yoon, H.; Lee, J.-K.; Kim, Y. K. Magnetic Multi-Granule Nanoclusters: A Model System That Exhibits Universal Size Effect of Magnetic Coercivity. *Sci. Rep.* **2015**, *5* (January), 12135. https://doi.org/10.1038/srep12135.

(43) Sherwood, J.; Lovas, K.; Rich, M.; Yin, Q.; Lackey, K.; Bolding, M. S.; Bao, Y. Shape-Dependent Cellular Behaviors and Relaxivity of Iron Oxide-Based T $_1$ MRI Contrast Agents. *Nanoscale* **2016**. https://doi.org/10.1039/C6NR06158C.

(44) Kim, B. H.; Lee, N.; Kim, H.; An, K.; Park, Y. Il; Choi, Y.; Shin, K.; Lee, Y.; Kwon, S. G.; Na, H. Bin; et al. Large-Scale Synthesis of Uniform and Extremely Small-Sized Iron Oxide Nanoparticles for High-Resolution t(1) Magnetic Resonance Imaging Contrast Agents. *J. Am. Chem. Soc.* **2011**, *133*, 12624–12631. https://doi.org/10.1021/ja203340u.

(45) Agarwal, R.; Brunelli, S. M.; Williams, K.; Mitchell, M. D.; Feldman, H. I.; Umscheid, C. A. Gadolinium-Based Contrast Agents and Nephrogenic Systemic Fibrosis: A Systematic Review and Meta-Analysis. *Nephrol. Dial. Transplant.* **2009**, *24* (3), 856–863. https://doi.org/10.1093/ndt/gfn593.

(46) Hervault, A.; Dunn, A. E.; Lim, M.; Boyer, C.; Mott, D.; Maenosono, S.; Thanh, N. T. K. Doxorubicin Loaded Dual PH- and Thermo-Responsive Magnetic Nanocarrier for Combined Magnetic Hyperthermia and Targeted Controlled Drug Delivery Applications. *Nanoscale* **2016**, *8*, 21–24. https://doi.org/10.1039/C5NR07773G.

(47) McBain, S. C.; Yiu, H. H. P.; Dobson, J. Magnetic Nanoparticles for Gene and Drug Delivery. *Int. J. Nanomedicine* **2008**, *3* (2), 169–180. https://doi.org/10.2147/IJN.S1608.

(48) Hervault Aziliz; Kim, T. N. T. Magnetic Nanoparticle- Based Therapeutic Agents for Thermo-Chemotherapy Treatment of Cancer. *Nanoscale* **2014**, *6*, 11553–11573. https://doi.org/10.1039/C4NR03482A.

(49) Stamopoulos, D.; Benaki, D.; Bouziotis, P.; Zirogiannis, P. N. In Vitro Utilization of Ferromagnetic Nanoparticles in Hemodialysis Therapy. *Nanotechnology* **2007**, *18* (49), 495102. https://doi.org/10.1088/0957-4484/18/49/495102.

(50) Chen, H.; Kaminski, M. D.; Liu, X.; Mertz, C. J.; Xie, Y.; Torno, M. D.; Rosengart, A. J. A Novel Human Detoxification System Based on Nanoscale Bioengineering and Magnetic Separation Techniques. *Med. Hypotheses* **2007**, *68* (5), 1071–1079. https://doi.org/10.1016/j.mehy.2005.04.047.

(51) MediSieve www.medisieve.com (accessed Oct 31, 2019).

(52) Khurshid, H.; Alonso, J.; Nemati, Z.; Phan, M. H.; Mukherjee, P.; Fdez-Gubieda, M. L.; Barandiarán, J. M.; Srikanth, H. Anisotropy Effects in Magnetic Hyperthermia: A Comparison between Spherical and Cubic Exchange-Coupled FeO/Fe3O4 Nanoparticles. *J. Appl. Phys.* **2015**, *117* (17), 17A337. https://doi.org/10.1063/1.4919250.

(53) Das, R.; Alonso, J.; Nemati Porshokouh, Z.; Kalappattil, V.; Torres, D.; Phan, M. H.; Garaio, E.; Garc??a, J. ??ngel; Sanchez Llamazares, J. L.; Srikanth, H. Tunable High Aspect Ratio Iron Oxide Nanorods for Enhanced Hyperthermia. *J. Phys. Chem. C* **2016**, *120* (18), 10086–10093. https://doi.org/10.1021/acs.jpcc.6b02006.

(54) Rahman, M.; Laurent, S.; Tawil, N.; Yahia, L. H. *Protein- Nanoparticle Interactions*; Springer Series in Biophysics 15. https://doi.org/10.1007/978-3-642-37555-2_2.

(55) Safi, M.; Courtois, J.; Seigneuret, M.; Conjeaud, H.; Berret, J. F. The Effects of Aggregation and Protein Corona on the Cellular Internalization of Iron Oxide Nanoparticles. *Biomaterials* **2011**, *32* (35), 9353–9363. https://doi.org/10.1016/j.biomaterials.2011.08.048.

(56) Mohapatra, J.; Mitra, A.; Tyagi, H.; Bahadur, D.; Aslam, M. Iron Oxide Nanorods as High-Performance Magnetic Resonance Imaging Contrast Agents. *Nanoscale* **2015**, *7* (20), 9174–9184. https://doi.org/10.1039/c5nr00055f.

(57) Guardia, P.; Di Corato, R.; Lartigue, L.; Wilhelm, C.; Espinosa, A.; Garcia-Hernandez, M.; Gazeau, F.; Manna, L.; Pellegrino, T. Water-Soluble Iron Oxide Nanocubes with High Values of Specific Absorption Rate for Cancer Cell Hyperthermia Treatment. *ACS Nano* **2012**, *6* (4), 3080–3091. https://doi.org/10.1021/nn2048137.

(58) Lartigue, L.; Hugounenq, P.; Alloyeau, D.; Clarke, S. P.; Lévy, M.; Bacri, J. C.; Bazzi, R.; Brougham, D. F.; Wilhelm, C.; Gazeau, F. Cooperative Organization in Iron Oxide Multi-Core Nanoparticles Potentiates Their Efficiency as Heating Mediators and MRI Contrast Agents. *ACS Nano* **2012**, *6*, 10935–10949. https://doi.org/10.1021/nn304477s.

(59) Pankhurst, Q. A.; Connolly, J.; Jones, S. K. Applications of Magnetic Nanoparticles in Biomedicine. *J. Phys. D. Appl. Phys.* **2003**, *36*, 167–181.

(60) Obaidat, I.; Issa, B.; Haik, Y. Magnetic Properties of Magnetic Nanoparticles for Efficient Hyperthermia. *Nanomaterials* **2015**, *5* (1), 63–89. https://doi.org/10.3390/nano5010063.

(61) Hemery, G.; Keyes, A. C.; Garaio, E.; Rodrigo, I.; Garcia, J. A.; Plazaola, F.; Garanger, E.; Sandre, O. Tuning Sizes, Morphologies, and Magnetic Properties of Mono-vs. Multi-Core Iron Oxide Nanoparticles through Control of Added Water in the Polyol Synthesis. *Inorg. Chem.* **2017**, *56*, 8232–8243. https://doi.org/10.1021/acs.inorgchem.7b00956.

(62) Lassenberger, A.; Grünewald, T. A.; Van Oostrum, P. D. J.; Rennhofer, H.; Amenitsch, H.; Zirbs, R.; Lichtenegger, H. C.; Reimhult, E. Monodisperse Iron Oxide Nanoparticles by Thermal Decomposition: Elucidating Particle Formation by Second-Resolved in Situ Small-Angle X-Ray Scattering. *Chem. Mater.* **2017**, *29* (10), 4511–4522. https://doi.org/10.1021/acs.chemmater.7b01207.

(63) Guardia, P.; Riedinger, A.; Nitti, S.; Pugliese, G.; Marras, S.; Genovese, A.; Materia, M. E.; Lefevre, C.; Manna, L.; Pellegrino, T. One Pot Synthesis of Monodisperse Water Soluble Iron Oxide Nanocrystals with High Values of the Specific Absorption Rate. *J. Mater. Chem. B* **2014**, *2*

(28), 4426. https://doi.org/10.1039/c4tb00061g.

(64) Xia, Y.; Xiong, Y.; Lim, B.; Skrabalak, S. E. Shape-Controlled Synthesis of Metal Nanocrystals: Simple Chemistry Meets Complex Physics? *Angew. Chemie - Int. Ed.* **2009**, *48* (1), 60–103. https://doi.org/10.1002/anie.200802248.

(65) Sun, H.; Chen, B.; Jiao, X.; Jiang, Z.; Qin, Z.; Chen, D. Solvothermal Synthesis of Tunable Electroactive Magnetite Nanorods by Controlling the Side Reaction. *J. Phys. Chem. C* **2012**, *116* (9), 5476–5481. https://doi.org/10.1021/jp211986a.

(66) Rishikeshi, S. N.; Joshi, S. S.; Temgire, M. K.; Bellare, J. R. Chain Length Dependence of Polyol Synthesis of Zinc Ferrite Nanoparticles: Why Is Diethylene Glycol so Different? *Dalton Trans.* **2013**, *42* (15), 5430–5438. https://doi.org/10.1039/c2dt32026f.

(67) Mourdikoudis, S.; Liz-Marzán, L. M. Oleylamine in Nanoparticle Synthesis. *Chem. Mater.* **2013**, *25* (9), 1465–1476. https://doi.org/10.1021/cm4000476.

(68) Sondjaja, R.; Alan Hatton, T.; Tam, M. K. C. Clustering of Magnetic Nanoparticles Using a Double Hydrophilic Block Copolymer, Poly(Ethylene Oxide)-b-Poly(Acrylic Acid). *J. Magn. Magn. Mater.* **2009**, *321* (16), 2393–2397. https://doi.org/10.1016/j.jmmm.2009.02.136.

(69) Zhao, J.; Lin, W.; Chang, Q.; Li, W.; Lai, Y. Adsorptive Characteristics of Akaganeite and Its Environmental Applications: A Review. *Environ. Technol. Rev.* **2012**, *2515* (March 2015), 1–13. https://doi.org/10.1080/09593330.2012.701239.

(70) Xu, W.; Wang, M.; Li, Z.; Wang, X.; Wang, Y.; Xing, M.; Yin, Y. Chemical Transformation of Colloidal Nanostructures with Morphological Preservation by Surface-Protection with Capping Ligands. *Nano Lett.* **2017**, acs.nanolett.7b00758. https://doi.org/10.1021/acs.nanolett.7b00758.

(71) Chandy, K. . Thermal Transformation of B-Ferric Oxyhydroxide. *Mineral.*

Mag. **1965**, *35* (272), 666–669.

(72) Blesa, M. A.; Mijalchik, M.; Villegas, M.; Rigotti, G. Transformation of Akaganeite into Magnetite in Aqueous Hydrazine Suspensions. *React. Solids* **1986**, *2* (1–2), 85–94. https://doi.org/10.1016/0168-7336(86)80066-3.

(73) Ponce, A. M.; Vujaskovic, Z.; Yuan, F.; Needham, D.; Dewhirst, M. W. Hyperthermia Mediated Liposomal Drug Delivery. *Int. J. Hyperthermia* **2006**, *22* (3), 205–213. https://doi.org/10.1080/02656730600582956.

(74) Kumar, C. S. S. R.; Mohammad, F. Magnetic Nanomaterials for Hyperthermia-Based Therapy and Controlled Drug Delivery. *Adv. Drug Deliv. Rev.* **2011**, *63* (9), 789–808. https://doi.org/10.1016/j.addr.2011.03.008.

(75) Zhan, S.; Yang, Y.; Shen, Z.; Shan, J.; Li, Y.; Yang, S.; Zhu, D. Efficient Removal of Pathogenic Bacteria and Viruses by Multifunctional Amine-Modified Magnetic Nanoparticles. *J. Hazard. Mater.* **2014**, *274*, 115–123. https://doi.org/10.1016/j.jhazmat.2014.03.067.

(76) Huy, T. Q.; Chung, P. Van; Thuy, T. Protein A-Conjugated Iron Oxide Nanoparticles for Separation of Vibrio Cholerae from Water Samples. **2014**, *44* (0), 73–82. https://doi.org/10.1039/C4FD00152D.

(77) Espinosa, A.; Kolosnjaj-tabi, J.; Abou-hassan, A.; Sangnier, A. P.; Curcio, A.; Silva, A. K. A.; Corato, R. Di; Neveu, S.; Pellegrino, T.; Liz-marzán, L. M.; et al. Magnetic (Hyper) Thermia or Photothermia ? Progressive Comparison of Iron Oxide and Gold Nanoparticles Heating in Water , in Cells , and In Vivo. *Adv. Funct. Mater.* **2018**, *1803660*, 1–16. https://doi.org/10.1002/adfm.201803660.

(78) Lacroix, L.; Lachaize, S.; Falqui, A.; Respaud, M.; Chaudret, B. Iron Nanoparticle Growth in Organic Superstructures. *J. Am. Chem. Soc.* **2009**, *131*, 549–557. https://doi.org/10.1021/ja805719c.

(79) Dung, N. T.; Long, N. V.; Tam, L. T. T.; Nam, P. H.; Tung, L. D.; Phuc, N. X.; Lu, L. T.; Kim Thanh, N. T. High Magnetisation, Monodisperse

and Water-Dispersible CoFe@Pt Core/Shell Nanoparticles. *Nanoscale* **2017**, *9*, 8952–8961. https://doi.org/10.1039/C6NR09325F.

(80) Meffre, A.; Mehdaoui, B.; Connord, V.; Carrey, J.; Fazzini, P. F.; Lachaize, S.; Respaud, M.; Chaudret, B. Complex Nano-Objects Displaying Both Magnetic and Catalytic Properties: A Proof of Concept for Magnetically Induced Heterogeneous Catalysis. *Nano Lett.* **2015**, *15*, 3241–3248. https://doi.org/10.1021/acs.nanolett.5b00446.

(81) Magaye, R.; Zhao, J.; Bowman, L.; Ding, M. Genotoxicity and Carcinogenicity of Cobalt-, Nickel- and Copper-Based Nanoparticles. *Exp. Ther. Med.* **2012**, *4*, 551–561. https://doi.org/10.3892/etm.2012.656.

(82) Jalem, R.; Rushton, M. J. D.; Manalastas, W.; Nakayama, M.; Kasuga, T.; Kilner, J. A.; Grimes, R. W. Effects of Gallium Doping in Garnet-Type Li7La3Zr2O12 Solid Electrolytes. *Chem. Mater.* **2015**, *27*, 2821–2831. https://doi.org/10.1021/cm5045122.

(83) Guria, A. K.; Dutta, S. K.; Adhikari, S. Das; Pradhan, N. Doping Mn2+ in Lead Halide Perovskite Nanocrystals: Successes and Challenges. *ACS Energy Lett.* **2017**, *2*, 1014–1021. https://doi.org/10.1021/acsenergylett.7b00177.

(84) Zhang, M.; Cao, Y.; Wang, L.; Ma, Y.; Tu, X.; Zhang, Z. Manganese Doped Iron Oxide Theranostic Nanoparticles for Combined T 1 Magnetic Resonance Imaging and Photothermal Therapy. *ACS Appl. Mater. Interfaces* **2015**, *7*, 4650–4658. https://doi.org/10.1021/am5080453.

(85) Zhou, Z.; Wang, L.; Chi, X.; Bao, J.; Yang, L.; Zhao, W.; Chen, Z.; Wang, X.; Chen, X.; Gao, J. Engineered Iron-Oxide-Based Nanoparticles as Enhanced T1 Contrast Agents for Efficient Tumor Imaging. *ACS Nano* **2013**, *7*, 3287–3296. https://doi.org/10.1021/nn305991e.

(86) Lima-Tenório, M. K.; Gómez Pineda, E. a.; Ahmad, N. M.; Fessi, H.; Elaissari, A. Magnetic Nanoparticles: In Vivo Cancer Diagnosis and Therapy. *Int. J. Pharm.* **2015**, *493* (1–2), 313–327. https://doi.org/10.1016/j.ijpharm.2015.07.059.

(87) Dreaden, E. C.; Austin, L. A.; Mackey, M. A.; El-Sayed, M. A. Size Matters: Gold Nanoparticles in Targeted Cancer Drug Delivery. *Ther. Deliv.* **2012**, *3*, 457–478. https://doi.org/10.4155/tde.12.21.

(88) Yang, L.; Kuang, H.; Zhang, W.; Aguilar, Z. P.; Xiong, Y.; Lai, W.; Xu, H.; Wei, H. Size Dependent Biodistribution and Toxicokinetics of Iron Oxide Magnetic Nanoparticles in Mice. *Nanoscale* **2015**, *7*, 625–636. https://doi.org/10.1039/C4NR05061D.

(89) Zyba, S. J.; Shenvi, S. V; Killilea, D. W.; Holland, T. C.; Kim, E.; Moy, A.; Sutherland, B.; Gildengorin, V.; Shigenaga, M. K.; King, J. C. A Moderate Increase in Dietary Zinc Reduces DNA Strand Breaks in Leukocytes and Alters Plasma Proteins without Changing Plasma Zinc. *Am. J. Clin. Nutr.* **2016**, *105*, 343–351. https://doi.org/10.3945/ajcn.116.135327.

(90) Ho, E.; Ames, B. N. Low Intracellular Zinc Induces Oxidative DNA Damage, Disrupts P53, NFkappa B, and AP1 DNA Binding, and Affects DNA Repair in a Rat Glioma Cell Line. *Proc. Natl. Acad. Sci. U. S. A.* **2002**, *99*, 16770–16775. https://doi.org/10.1073/pnas.222679399.

(91) Eide, D. J. The Oxidative Stress of Zinc Deficiency. *Metallomics* **2011**, *3*, 1124–1129. https://doi.org/10.1039/c1mt00064k.

(92) Hachani, R.; Lowdell, M.; Birchall, M.; Hervault, A.; Mertz, D.; Begin-Colin, S.; Thanh, N. T. K. Polyol Synthesis, Functionalisation, and Biocompatibility Studies of Superparamagnetic Iron Oxide Nanoparticles as Potential MRI Contrast Agents. *Nanoscale* **2015**, *8*, 3278–3287. https://doi.org/10.1039/C5NR03867G.

(93) Shannon, R. D. Revised Effective Ionic Radii and Systematic Studies of Interatomie Distances in Halides and Chaleogenides. L Du Pont de Nemours The Effective Ionic Radii of Shannon & Prewitt [Acta Cryst . (1969), B25 , 925-945] Are Revised to Include More Unusual Ox. *Acta Crystallogr. Sect. A* **1976**, *32*, 751–767.

(94) Li, S.; Sellers, M. S.; Basaran, C.; Schultz, A. J.; Kofke, D. A. Lattice Strain Due to an Atomic Vacancy. *Int. J. Mol. Sci.* **2009**, *10*, 2798–2808.

https://doi.org/10.3390/ijms10062798.

(95) Burdett, J. K.; Price, S. L.; Price, G. D. Role of the Crystal-Field Theory in Determining the Structures of Spinels. *J. Am. Chem. Soc.* **1982**, *104*, 92–95. https://doi.org/10.1021/ja00365a019.

(96) Jang, J. T.; Nah, H.; Lee, J. H.; Moon, S. H.; Kim, M. G.; Cheon, J. Critical Enhancements of MRI Contrast and Hyperthermic Effects by Dopant-Controlled Magnetic Nanoparticles. *Angew. Chemie - Int. Ed.* **2009**, *48*, 1234–1238. https://doi.org/10.1002/anie.200805149.

(97) Coşkun, M.; Can, M. M.; Coşkun, Ö. D.; Korkmaz, M.; Fırat, T. Surface Anisotropy Change of CoFe2O4 Nanoparticles Depending on Thickness of Coated SiO2 Shell. *J. Nanoparticle Res.* **2012**, *14*, 1197. https://doi.org/10.1007/s11051-012-1197-6.

(98) Moore, T. L.; Rodriguez-Lorenzo, L.; Hirsch, V.; Balog, S.; Urban, D.; Jud, C.; Rothen-Rutishauser, B.; Lattuada, M.; Petri-Fink, A. Nanoparticle Colloidal Stability in Cell Culture Media and Impact on Cellular Interactions. *Chem. Soc. Rev.* **2015**, *44*, 6287–6305. https://doi.org/10.1039/c4cs00487f.

(99) Wang, J.; Li, Y.; Deng, L.; Wei, N.; Weng, Y.; Dong, S.; Qi, D.; Qiu, J.; Chen, X.; Wu, T. High-Performance Photothermal Conversion of Narrow-Bandgap Ti $_2$ O $_3$ Nanoparticles. *Adv. Mater.* **2016**, 1–6. https://doi.org/10.1002/adma.201603730.

(100) Qiao, L.; Fu, Z.; Li, J.; Ghosen, J.; Zeng, M.; Stebbins, J.; Prasad, P. N.; Swihart, M. T. Standardizing Size- and Shape-Controlled Synthesis of Monodisperse Magnetite (Fe 3 O 4) Nanocrystals by Identifying and Exploiting Effects of Organic Impurities. *ACS Nano* **2017**, *11*, 6370–6381. https://doi.org/10.1021/acsnano.7b02752.

(101) Herman, D. A. J.; Cheong-Tilley, S.; McGrath, A. J.; McVey, B. F. P.; Lein, M.; Tilley, R. D. How to Choose a Precursor for Decomposition Solution-Phase Synthesis: The Case of Iron Nanoparticles. *Nanoscale* **2015**, *7* (14), 5951–5954. https://doi.org/10.1039/C5NR00718F.

(102) Thanh, N. T. K.; Maclean, N.; Mahiddine, S. Mechanisms of Nucleation and Growth of Nanoparticles in Solution. *Chem. Rev.* **2014**, *114* (15), 7610–7630. https://doi.org/10.1021/cr400544s.

(103) You, H.; Fang, J. Particle-Mediated Nucleation and Growth of Solution-Synthesized Metal Nanocrystals: A New Story beyond the LaMer Curve. *Nano Today* **2016**, *11* (2), 145–167. https://doi.org/10.1016/j.nantod.2016.04.003.

(104) Zhang, S.; Jiang, G.; Filsinger, G.; Wu, L.; Zhu, H.; Lee, J.; Wu, Z.; Sun, S. Halide Ion-Mediated Growth of Single Crystalline Fe Nanoparticles. *Nanoscale* **2014**, No. 310058, 4852–4856. https://doi.org/10.1039/c4nr00193a.

(105) Lin, X. M.; Sorensen, C. M.; Klabunde, K. J. Digestive Ripening, Nanophase Segregation and Superlattice Formation in Gold Nanocrystal Colloids. *J. Nanoparticle Res.* **2000**, *2* (2), 157–164. https://doi.org/10.1023/A:1010078521951.

(106) Prasad, B. L. V.; Stoeva, S. I.; Sorensen, C. M.; Klabunde, K. J. Digestive Ripening of Thiolated Gold Nanoparticles: The Effect of Alkyl Chain Length. *Langmuir* **2002**, *18* (20), 7515–7520. https://doi.org/10.1021/la020181d.

(107) Sahu, P.; Prasad, B. L. V. Time and Temperature Effects on the Digestive Ripening of Gold Nanoparticles: Is There a Crossover from Digestive Ripening to Ostwald Ripening? *Langmuir* **2014**, *30* (34), 10143–10150. https://doi.org/10.1021/la500914j.

(108) Cingarapu, S.; Yang, Z.; Sorensen, C. M.; Klabunde, K. J. Synthesis of CdSe/ZnS and CdTe/ZnS Quantum Dots: Refined Digestive Ripening. *J. Nanomater.* **2012**, *2012*. https://doi.org/10.1155/2012/312087.

(109) Yoder, T. S.; Cloud, J. E.; Leong, G. J.; Molk, D. F.; Tussing, M.; Miorelli, J.; Ngo, C.; Kodambaka, S.; Eberhart, M. E.; Richards, R. M.; et al. Iron Pyrite Nanocrystal Inks: Solvothermal Synthesis, Digestive Ripening, and Reaction Mechanism. *Chem. Mater.* **2014**, *26* (23), 6741–6751. https://doi.org/10.1021/cm5030553.

(110) Shimpi, J. R.; Sidhaye, D. S.; Prasad, B. L. V. Digestive Ripening: A Fine Chemical Machining Process on the Nanoscale. *Langmuir* **2017**, *33* (38), 9491–9507. https://doi.org/10.1021/acs.langmuir.7b00193.

(111) Kemp, S. J.; Ferguson, R. M.; Khandhar, A. P.; Krishnan, K. M. Monodisperse Magnetite Nanoparticles with Nearly Ideal Saturation Magnetization. *RSC Adv.* **2016**, *6* (81), 77452–77464. https://doi.org/10.1039/C6RA12072E.

(112) Hufschmid, R.; Arami, H.; Ferguson, R. M.; Gonzales, M.; Teeman, E.; Brush, L. N.; Browning, N. D.; Krishnan, K. M. Synthesis of Phase-Pure and Monodisperse Iron Oxide Nanoparticles by Thermal Decomposition. *Nanoscale* **2015**, *7* (25), 11142–11154. https://doi.org/10.1039/c5nr01651g.

(113) Hyeon, T.; Su Seong Lee; Park, J.; Chung, Y.; Hyon Bin Na. Synthesis of Highly Crystalline and Monodisperse Maghemite Nanocrystallites without a Size-Selection Process. *J. Am. Chem. Soc.* **2001**, *123* (51), 12798–12801. https://doi.org/10.1021/ja016812s.

(114) Wang, Z.-L.; Ma, H.; Wang, F.; Li, M.; Zhang, L.-G.; Xu, X.-H. Controllable Synthesis and Magnetic Properties of Monodisperse Fe_3O_4 Nanoparticles. *Chinese Phys. Lett.* **2016**, *33* (10), 107501. https://doi.org/10.1088/0256-307X/33/10/107501.

(115) Van Embden, J.; Mulvaney, P. Nucleation and Growth of CdSe Nanocrystals in a Binary Ligand System. *Langmuir* **2005**, *21* (22), 10226–10233. https://doi.org/10.1021/la051081l.

(116) Sugimoto, T. Preparation of Monodispersed Colloidal Particles. *Adv. Colloid Interface Sci.* **1987**, *28* (C), 65–108. https://doi.org/10.1016/0001-8686(87)80009-X.

(117) Mohapatra, S.; Pramanik, P. Synthesis and Stability of Functionalized Iron Oxide Nanoparticles Using Organophosphorus Coupling Agents. *Colloids Surfaces A Physicochem. Eng. Asp.* **2009**, *339* (1–3), 35–42. https://doi.org/10.1016/j.colsurfa.2009.01.009.

(118) Zvarec, O.; Purushotham, S.; Masic, A.; Ramanujan, R. V.; Miserez, A. Catechol-Functionalized Chitosan/Iron Oxide Nanoparticle Composite Inspired by Mussel Thread Coating and Squid Beak Interfacial Chemistry. *Langmuir* **2013**, *29* (34), 10899–10906. https://doi.org/10.1021/la401858s.

(119) Lagrow, A. P.; Ingham, B.; Toney, M. F.; Tilley, R. D. Effect of Surfactant Concentration and Aggregation on the Growth Kinetics of Nickel Nanoparticles. *J. Phys. Chem. C* **2013**, *117* (32), 16709–16718. https://doi.org/10.1021/jp405314g.

(120) Sharifi Dehsari, H.; Heidari, M.; Halda Ribeiro, A.; Tremel, W.; Jakob, G.; Donadio, D.; Potestio, R.; Asadi, K. Combined Experimental and Theoretical Investigation of Heating Rate on Growth of Iron Oxide Nanoparticles. *Chem. Mater.* **2017**, *29* (22), 9648–9656. https://doi.org/10.1021/acs.chemmater.7b02872.

(121) Stensberg, M. C.; Wei, Q.; Mclamore, E. S.; Marshall, D.; Wei, A.; Porterfield, D. M.; Sepulveda, M. S. Toxicological Studies on Silver Nanoparticles. *Nanomedicine (Lond)* **2011**, *6* (5), 879–898. https://doi.org/10.2217/nnm.11.78.Toxicological.

(122) Plan Sangnier, A.; Preveral, S.; Curcio, A.; K. A. Silva, A.; Lefèvre, C. T.; Pignol, D.; Lalatonne, Y.; Wilhelm, C. Targeted Thermal Therapy with Genetically Engineered Magnetite Magnetosomes@RGD: Photothermia Is Far More Efficient than Magnetic Hyperthermia. *J. Control. Release* **2018**, *279* (January), 271–281. https://doi.org/10.1016/j.jconrel.2018.04.036.

(123) Ziech, D.; Franco, R.; Pappa, A.; Panayiotidis, M. I. Reactive Oxygen Species (ROS)--Induced Genetic and Epigenetic Alterations in Human Carcinogenesis. *Mutat. Res. - Fundam. Mol. Mech. Mutagen.* **2011**, *711* (1–2), 167–173. https://doi.org/10.1016/j.mrfmmm.2011.02.015.

(124) Di Corato, R.; Espinosa, A.; Lartigue, L.; Tharaud, M.; Chat, S.; Pellegrino, T.; Ménager, C.; Gazeau, F.; Wilhelm, C. Magnetic Hyperthermia Efficiency in the Cellular Environment Fordifferent

Nanoparticle Designs. *Biomaterials* **2014**, *35* (24), 6400–6411. https://doi.org/10.1016/j.biomaterials.2014.04.036.

(125) Tang, H. L.; Tang, H. M.; Mak, K. H.; Hu, S.; Wang, S. S.; Wong, K. M.; Wong, C. S. T.; Wu, H. Y.; Law, H. T.; Liu, K.; et al. Cell Survival, DNA Damage, and Oncogenic Transformation after a Transient and Reversible Apoptotic Response. *Mol. Biol. Cell* **2012**, *23* (12), 2240–2252. https://doi.org/10.1091/mbc.e11-11-0926.

(126) Narula, J.; Haider, N.; Arbustini, E.; Chandrashekhar, Y. Mechanisms of Disease: Apoptosis in Heart Failure - Seeing Hope in Death. *Nat. Clin. Pract. Cardiovasc. Med.* **2006**, *3* (12), 681–688. https://doi.org/10.1038/ncpcardio0710.

(127) Chabaud, S.; Moulin, V. J. Apoptosis Modulation as a Promising Target for Treatment of Systemic Sclerosis. *Int. J. Rheumatol.* **2011**, *2011*. https://doi.org/10.1155/2011/495792.

(128) Tang, H. M.; Tang, H. L. Anastasis: Recovery from the Brink of Cell Death. *R. Soc. Open Sci.* **2018**, *5* (9). https://doi.org/10.1098/rsos.180442.

(129) G Kroemer, L Galluzzi1, P Vandenabeele, J Abrams, ES Alnemri, EH Baehrecke, MV Blagosklonny, WS El-Deiry, P Golstein, DR Green, M Hengartner, RA Knight, S Kumar, SA Lipton, W Malorni, G Nuñez, ME Peter, J Tschopp, J Yuan, M Piacentini, B Zhivotovsky, and G. M. Classification of Cell Death: Recommendations. *Cell Death Differ.* **2009**, *16* (1), 3–11. https://doi.org/10.1038/cdd.2008.150.Classification.

(130) GOODSELL, D. S. The Molecular Perspective : Caspases. *Oncologist* **2000**, *5*, 435–436.

(131) McIlwain, D. R.; Berger, T.; Mak, T. W. Caspase Functions in Cell Death and Disease. *Cold Spring Harb. Perspect. Biol.* **2013**, *5* (4), 1–28. https://doi.org/10.1101/cshperspect.a008656.

(132) Orrenius, S.; Zhivotovsky, B. Cardiolipin Oxidation Sets Cytochrome C Free. *Nat. Chem. Biol.* **2005**, *1* (4), 188–189.

https://doi.org/10.1038/nchembio0905-188.

(133) Tavaria, M.; Gabriele, T.; Kola, I.; L., A. R. A Hitchhiker's Guide to the Human HSP70 Family. *Cell Stress Chaperones* **1996**, *1* (1), 23–28.

(134) Green, D. R.; Beere, H. M.; Wolf, B. B.; Cain, K.; Mosser, D. D.; Mahboubi, A.; Kuwana, T.; Tailor, P.; Morimoto, R. I.; Cohen, G. M. Heat-Shock Protein 70 Inhibits Apoptosis by Preventing Recruitment of Procaspase-9 to the Apaf-1 Apoptosome. *Nat. Cell Biol.* **2000**, *2* (8), 469–475. https://doi.org/10.1038/35019501.

(135) Deveraux, Q. L.; Reed, J. C. IAP Family Proteins - Suppressors of Apoptosis. *Genes Dev.* **1999**, *13* (3), 239–252. https://doi.org/10.1101/gad.13.3.239.

(136) Reed, J. C.; Deveraux, Q. L.; Takahashi, R.; Salvesen, G. S. X-Linked IAP Is a Direct Inhibitor of Cell-Death Proteases. *Nature* **1997**, *388* (6639), 300–304. https://doi.org/10.1038/40901.

(137) Duckett, C. S.; Li, F.; Wang, Y.; Tomaselli, K. J.; Thompson, C. B.; Armstrong, R. C. Human IAP-Like Protein Regulates Programmed Cell Death Downstream of Bcl-x L and Cytochrome C . *Mol. Cell. Biol.* **2015**, *18* (1), 608–615. https://doi.org/10.1128/mcb.18.1.608.

(138) Tong, Q. S.; Zheng, L. D.; Wang, L.; Zeng, F. Q.; Chen, F. M.; Dong, J. H.; Lu, G. C. Downregulation of XIAP Expression Induces Apoptosis and Enhances Chemotherapeutic Sensitivity in Human Gastric Cancer Cells. *Cancer Gene Ther.* **2005**, *12* (5), 509–514. https://doi.org/10.1038/sj.cgt.7700813.

(139) Duan, X.; Li, Y. Physicochemical Characteristics of Nanoparticles Affect Circulation, Biodistribution, Cellular Internalization, and Trafficking. *Small* **2013**, *9* (9–10), 1521–1532. https://doi.org/10.1002/smll.201201390.

(140) Longmier, M.; Choyke, P. L.; Kobayashi, H. Clearance Properties of Nano-Sized Particles and Molecules as Imaging Agents: Consideration and Caveats. *Nanomedicine (Lond)* **2012**, *3* (5), 703–717.

https://doi.org/10.2217/17435889.3.5.703.Clearance.

(141) Xiao, K.; Li, Y.; Luo, J.; Lee, J. S.; Xiao, W.; Gonik, A. M.; Agarwal, R. G.; Lam, K. S. The Effect of Surface Charge on in Vivo Biodistribution of PEG-Oligocholic Acid Based Micellar Nanoparticles. *Biomaterials* **2011**, *32* (13), 3435–3446. https://doi.org/10.1016/j.biomaterials.2011.01.021.

(142) Dawidczyk, C. M.; Russell, L. M.; Searson, P. C. Nanomedicines for Cancer Therapy: State-of-the-Art and Limitations to Pre-Clinical Studies That Hinder Future Developments. *Front. Chem.* **2014**, *2* (August), 1–13. https://doi.org/10.3389/fchem.2014.00069.

(143) National Centre for the Replacement Refinement & Reduction of Animals in Research.

(144) Máté, G.; Šimeček, J.; Pniok, M.; Kertész, I.; Notni, J.; Wester, H. J.; Galuska, L.; Hermann, P. The Influence of the Combination of Carboxylate and Phosphinate Pendant Arms in 1,4,7-Triazacyclononane-Based Chelators on Their ^{68}Ga Labelling Properties. *Molecules* **2015**, *20* (7), 13112–13126. https://doi.org/10.3390/molecules200713112.

(145) Winter, M. J. *D-Block Chemistry*; Oxford University Press, 2011.

(146) Kumar, K.; Nightingale, A. M.; Krishnadasan, S. H.; Kamaly, N.; Wylenzinska-Arridge, M.; Zeissler, K.; Branford, W. R.; Ware, E.; DeMello, A. J.; DeMello, J. C. Direct Synthesis of Dextran-Coated Superparamagnetic Iron Oxide Nanoparticles in a Capillary-Based Droplet Reactor. *J. Mater. Chem.* **2012**, *22* (11), 4704. https://doi.org/10.1039/c2jm30257h.

(147) Lee, J.-H.; Jang, J.; Choi, J.; Moon, S. H.; Noh, S.; Kim, J.; Kim, J.-G.; Kim, I.-S.; Park, K. I.; Cheon, J. Exchange-Coupled Magnetic Nanoparticles for Efficient Heat Induction. *Nat. Nanotechnol.* **2011**, *6* (7), 418–422. https://doi.org/10.1038/nnano.2011.95.

(148) Lalatsa, A.; Schätzlein, A. G.; Garrett, N. L.; Moger, J.; Briggs, M.; Godfrey, L.; Iannitelli, A.; Freeman, J.; Uchegbu, I. F. Chitosan

Amphiphile Coating of Peptide Nanofibres Reduces Liver Uptake and Delivers the Peptide to the Brain on Intravenous Administration. *J. Control. Release* **2015**, *197*, 87–96. https://doi.org/10.1016/j.jconrel.2014.10.028.

(149) Tsoukalas, C.; Geninatti-Crich, S.; Gaitanis, A.; Tsotakos, T.; Paravatou-Petsotas, M.; Aime, S.; Jiménez-Juárez, R.; Anagnostopoulos, C. D.; Djanashvili, K.; Bouziotis, P. Tumor Targeting via Sialic Acid: [68Ga]DOTA-En-Pba as a New Tool for Molecular Imaging of Cancer with PET. *Mol. Imaging Biol.* **2018**, No. February, 1–10. https://doi.org/10.1007/s11307-018-1176-0.

(150) Chopra, S.; Mahdi, S.; Kaur, J.; Iqbal, Z.; Talegaonkar, S.; Ahmad, F. J. Advances and Potential Applications of Chitosan Derivatives as Mucoadhesive Biomaterials in Modern Drug Delivery. *J. Pharm. Pharmacol.* **2006**, *58* (8), 1021–1032. https://doi.org/10.1211/jpp.58.8.0002.

(151) Amidi, M.; Romeijn, S. G.; Verhoef, J. C.; Junginger, H. E.; Bungener, L.; Huckriede, A.; Crommelin, D. J. A.; Jiskoot, W. N-Trimethyl Chitosan (TMC) Nanoparticles Loaded with Influenza Subunit Antigen for Intranasal Vaccination: Biological Properties and Immunogenicity in a Mouse Model. *Vaccine* **2007**, *25* (1), 144–153. https://doi.org/10.1016/j.vaccine.2006.06.086.

(152) Araya, T.; Kasahara, K.; Nishikawa, S.; Kimura, H.; Sone, T.; Nagae, H.; Ikehata, Y.; Nagano, I.; Fujimura, M. Antitumor Effects of Inductive Hyperthermia Using Magnetic Ferucarbotran Nanoparticles on Human Lung Cancer Xenografts in Nude Mice. *Onco. Targets. Ther.* **2013**, *6*, 237–242. https://doi.org/10.2147/OTT.S42815.

(153) Salunkhe, a B.; Khot, V. M.; Pawar, S. H. Magnetic Hyperthermia with Magnetic Nanoparticles: A Status Review. *Curr. Top. Med. Chem.* **2014**, *14* (5), 572–594. https://doi.org/10.2174/1568026614666140118203550.

(154) Lu, C.; Bhatt, L. R.; Jun, H. Y.; Park, S. H.; Chai, K. Y. Carboxyl–

Polyethylene Glycol–Phosphoric Acid: A Ligand for Highly Stabilized Iron Oxide Nanoparticles. *J. Mater. Chem.* **2012**, *22* (AUGUST), 19806–19811. https://doi.org/10.1039/c2jm34327d.

(155) Thorek, D. L. J.; Tsourkas, A. Size, Charge and Concentration Dependent Uptake of Iron Oxide Particles by Non-Phagocytic Cells. *Biomaterials* **2008**, *29* (26), 3583–3590. https://doi.org/10.1016/j.biomaterials.2008.05.015.

(156) Fr??hlich, E. The Role of Surface Charge in Cellular Uptake and Cytotoxicity of Medical Nanoparticles. *Int. J. Nanomedicine* **2012**, *7*, 5577–5591. https://doi.org/10.2147/IJN.S36111.

(157) Zhao, X.; Ng, S.; Heng, B. C.; Guo, J.; Ma, L.; Tan, T. T. Y.; Ng, K. W.; Loo, S. C. J. Cytotoxicity of Hydroxyapatite Nanoparticles Is Shape and Cell Dependent. *Arch. Toxicol.* **2013**, *87* (6), 1037–1052. https://doi.org/10.1007/s00204-012-0827-1.

(158) Lee, J. H.; Ju, J. E.; Kim, B. Il; Pak, P. J.; Choi, E. K.; Lee, H. S.; Chung, N. Rod-Shaped Iron Oxide Nanoparticles Are More Toxic than Sphere-Shaped Nanoparticles to Murine Macrophage Cells. *Environ. Toxicol. Chem.* **2014**, *33* (12), 2759–2766. https://doi.org/10.1002/etc.2735.

(159) Van Den Berg, B. M.; Nieuwdorp, M.; Stroes, E. S. G.; Vink, H. Glycocalyx and Endothelial (Dys) Function: From Mice to Men. *Pharmacol. Reports* **2006**, *58*, 75–80.

(160) Yardeni, T.; Eckhaus, M.; Morris, H. D. Retro-Orbital_injections_in_mice Lab Animal 2011.Pdf. *Lab Anim* **2011**, *40* (5), 155–160. https://doi.org/10.1038/laban0511-155.Retro-orbital.

(161) Marasini, N.; Skwarczynski, M.; Toth, I. Intranasal Delivery of Nanoparticle-Based Vaccines. *Ther. Deliv.* **2017**, *8* (3), 151–167.

(162) Rassu, G.; Porcu, E. P.; Fancello, S.; Obinu, A.; Senes, N.; Galleri, G.; Migheli, R.; Gavini, E.; Giunchedi, P. Intranasal Delivery of Genistein-Loaded Nanoparticles as a Potential Preventive System against Neurodegenerative Disorders. *Pharmaceutics* **2019**, *11* (1).

https://doi.org/10.3390/pharmaceutics11010008.

(163) Aly, A. E.; Harmon, B. T.; Dines, K.; Sesenoglu-laird, O.; Padegimas, L.; Cooper, M. J.; Waszczak, B. L. Intranasal Delivery of HGDNF Nanoparticles Results in GDNF Expression throughout Rat Brain and Provides Neuroprotection in the Rat6-Hydroxydopamine Model of Parkinson's Disease. *Mol. Neurobiol.* **2019**, *56*, 688–701.

(164) Daneman, R.; Prat, A. The Blood –Brain Barrier. *Cold Spring Harb. Perspect. Biol.* **2015**, *7*, 1–23.

(165) Grant, J. C. B. *An Atlas of Anatomy*; The Williams & Wilkins Co., 1962.

(166) *Nanobiomaterials in Drug Delivery*; Grumezescu, A. M., Ed.; Elsevier, 2016.

(167) Misra, A.; Shahiwala, A. *Applications of Polymers in Drug Delivery*; Smithers Rapra Technology Ltd, 2014.

(168) Amidi, M.; Mastrobattista, E.; Jiskoot, W.; Hennink, W. E. Chitosan-Based Delivery Systems for Protein Therapeutics and Antigens. *Adv. Drug Deliv. Rev.* **2010**, *62* (1), 59–82. https://doi.org/10.1016/j.addr.2009.11.009.

(169) Jabbal-Gill, I.; Watts, P.; Smith, A. Chitosan-Based Delivery Systems for Mucosal Vaccines. *Expert Opin. Drug Deliv.* **2012**, *9* (9), 1051–1067. https://doi.org/10.1517/17425247.2012.697455.

(170) Lentijo Mozo, S.; Zuddas, E.; Casu, A.; Falqui, A. Synthesizing Iron Oxide Nanostructures: The Polyethylenenemine (PEI) Role. *Crystals* **2017**, *7* (1), 22. https://doi.org/10.3390/cryst7010022.

(171) Piao, Y.; Kim, J.; Na, H. Bin; Kim, D.; Baek, J. S.; Ko, M. K.; Lee, J. H.; Shokouhimehr, M.; Hyeon, T. Wrap-Bake-Peel Process for Nanostructural Transformation from Beta-FeOOH Nanorods to Biocompatible Iron Oxide Nanocapsules. *Nat. Mater.* **2008**, *7* (3), 242–247. https://doi.org/10.1038/nmat2118.

(172) Espinosa, A.; Curcio, A.; Cabana, S.; Radtke, G.; Bugnet, M.; Kolosnjaj-Tabi, J.; Péchoux, C.; Alvarez-Lorenzo, C.; Botton, G. A.; Silva, A. K. A.;

et al. Intracellular Biodegradation of Ag Nanoparticles, Storage in Ferritin, and Protection by a Au Shell for Enhanced Photothermal Therapy. *ACS Nano* **2018**, *12* (7), 6523–6535. https://doi.org/10.1021/acsnano.8b00482.

(173) Zimmer, J. P.; Liu, X.; Yang, Y.; Xiao, W.; Li, Z.; Xue, D.; Li, F.; Ding, J. Synthesis of Nonstoichiometric Zinc Ferrite Nanoparticles with Extraordinary Room Temperature Magnetism and Their Diverse Applications. *J. Mater. Chem. C* **2013**, *1*, 2875–2885. https://doi.org/10.1039/c3tc00790a.

(174) Byrne, J. M.; Coker, V. S.; Cespedes, E.; Wincott, P. L.; Vaughan, D. J.; Pattrick, R. A. D.; Van Der Laan, G.; Arenholz, E.; Tuna, F.; Bencsik, M.; et al. Biosynthesis of Zinc Substituted Magnetite Nanoparticles with Enhanced Magnetic Properties. *Adv. Funct. Mater.* **2014**, *24*, 2518–2529. https://doi.org/10.1002/adfm.201303230.

(175) Zhao, Z.; Chi, X.; Yang, L.; Yang, R.; Ren, B. W.; Zhu, X.; Zhang, P.; Gao, J. Cation Exchange of Anisotropic-Shaped Magnetite Nanoparticles Generates High-Relaxivity Contrast Agents for Liver Tumor Imaging. *Chem. Mater.* **2016**, *28*, 3497–3506. https://doi.org/10.1021/acs.chemmater.6b01256.